



**UNIVERSITA' DEGLI STUDI DI BARI ALDO MORO**

**DIPARTIMENTO INTERATENEO DI FISICA**

**'MICHELANGELO MERLIN'**

**SCUOLA DI DOTTORATO DI RICERCA IN FISICA**

**XXXVI CYCLE**

**Settore Scientifico Disciplinare: FIS/03**

**Nanomechanical and Surface Potential Characterization of  
Protein Films via Atomic Force and Kelvin Probe Force  
Microscopy**

Submitted to University of Bari Aldo Moro, Italy in partial fulfillment of the  
requirements for the award of the degree of

**Doctor of Philosophy in Physics**

**Dottorando:** Dott. Aniq Khaliq

**Supervisore (Tutor):** Ch.mo Prof. Gaetano Scamarcio

**Coordinatore:** Ch.mo Prof. Domenico Di Bari

**Session: 2021-2024**

**Esame Finale 2025**

## **Dedications**

To my beloved parents and family who gave me the opportunity to educate myself at the best institutions.

# Table of Contents

Table of Contents .....	ii
Acknowledgment .....	v
List of abbreviations and symbols .....	vi
List of Figures .....	ix
List of Tables.....	xiv
Research Project.....	xv
Thesis Organization .....	xvi
Abstract.....	xviii
Chapter 1 Introduction .....	1
1.1 Techniques for Studying Mechanical Properties .....	5
1.1.1 AFM based nanoindentation .....	5
1.1.2 Cantilever-based optical interfacial force microscopy (COIFM) .....	5
1.1.3 Quartz crystal microbalance with dissipation (QCM-D).....	6
1.1.4 Atomic force microscopy based force spectroscopy (AFM-FS) .....	7
1.1.5 Force-volume AFM.....	8
1.1.6 Bimodal AFM .....	9
1.1.7 Contact resonance AFM.....	10
1.1.8 Multi-harmonic AFM.....	10
1.1.9 Torsional harmonic AFM.....	10
Chapter 2 Theoretical Background .....	12
2.1 Protein films.....	12
2.2 Theories related to mechanical Properties .....	13
2.2.1 Hertzian model.....	13
2.2.2 Derjaguin–Muller–Toporov (DMT) model.....	13
2.2.3 Johnson–Kendall–Roberts (JKR) model.....	14
2.2.4 Sneddon Model .....	14

2.2.5	Oliver-Pharr Method .....	15
2.3	Principles of AFM.....	15
2.4	Theory of the dynamic mode .....	18
2.4.1	Equation of motion .....	19
2.4.2	Driven and self-driven cantilevers .....	19
2.5	Theory of the AM-MODE .....	21
2.6	Dynamic force spectroscopy using the AM-AFM.....	24
2.7	Energy dissipation in AM-AFM .....	24
2.8	Kelvin Probe Force Microscopy (KPFM).....	25
2.8.1	Principles of KPFM .....	25
Chapter 3	Experimental Methods .....	29
3.1	Materials .....	29
3.1.1	Biofunctionalization protocol .....	30
3.1.2	AFM measurements .....	31
3.1.3	AFM Setup and Calibration .....	31
3.1.4	Topography measurement:.....	35
3.1.5	Dynamic force spectroscopy.....	35
3.2	Data Analysis .....	38
3.2.1	Methods for Analyzing AM-AFM Data.....	38
3.2.2	Reconstruction of tip-sample force.....	40
3.3	Materials .....	43
3.3.1	Patterned bio-functionalized Au surfaces fabrication .....	43
3.3.2	KPFM Measurements .....	44
3.4	Single-molecule KPFM measurements protocol .....	45
3.5	Electrolyte-gated SiMoT fabrication and single-molecule sensing .....	46
Chapter 4	Results and Discussion.....	47
4.1	AFM and AM-AFM Measurements .....	47

4.2	Energy Dissipation in AM-AFM .....	50
4.3	Mechanical properties .....	53
4.4	AFM Measurements.....	57
4.5	Electrolyte-gated SiMoT sensor I-V transfer curves .....	58
4.6	Kelvin probe force microscopy (KPFM) measurements .....	59
4.7	Surface Potential shifts induced by few binding events .....	68
	Chapter 5 Conclusion and Future Perspectives .....	70
	References.....	72
	Curriculum Vitae.....	86

# Acknowledgment

I am thankful to Allah almighty who bestowed upon me the intellectual ability, courage and strength to complete this contribution towards knowledge.

First and foremost, I deem it as my utmost pleasure to express my deepest thanks and respect to my Supervisor Prof. Gaetano Scamarcio. I am strongly indebted the guidance, encouragement and support he has provided me throughout my research. I have been extremely lucky to have you as a supervisor. Every single time, I have approached him with some query or difficulty regarding my research. He provided me with his precious time, valuable suggestions, and useful directions. He is a man who I found with great patience, kindness, affection, inspiring with helping attitude toward students. I must say he is a great scientist, a great mentor, a great supervisor and a great human being.

I am deeply indebted to Dr. Cinzia di Franco, Dr. Hendrik Holscher, Prof. Luisa Torsi, and Dr. Eleonora Macchia for their scientific support. A special thanks to Cinzia di Franco for her continuous support throughout my PhD journey. I am also grateful to Mr. Piero Calabrese for his technical assistance and contributions. Additionally, I extend my thanks to Dr. Riccardo Funari, Moh Rafik, Dr. Lucia Sarcina, Dr. Nicoletta Di Taranto, and Dr. Matteo Piscitelli for their scientific input. A heartfelt thanks goes to Dr. Abouzar Sarfaraz for his steadfast support during my PhD, and to my son, Syed Muhammad Areeb Abouzar, for the joy and laughter he brought into this journey.

I am heartily grateful to my lovely parents for their prayers and endless support that keeps me standing firmly through all thick and thin. I am heartily grateful to my uncle M. Akhlaq for their moral support. To my siblings, I am greatly thankful for their sacrifices, motivation, and patience throughout my PhD journey.

# List of abbreviations and symbols

## List of Abbreviations

<b>AFM</b>	Atomic Force Microscopy
<b>AM-AFM</b>	Amplitude Modulation - Atomic Force Microscopy
<b>APD</b>	Amplitude-Phase Distance
<b>Au</b>	Gold
<b>CPD</b>	Contact Potential Difference
<b>EGOFET</b>	Electrolyte-Gated Organic Field Effect Transistor
<b>fM</b>	Femtomolar
<b>IgG</b>	Immunoglobulin G
<b>IgM</b>	Immunoglobulin M
<b>JKR</b>	Johnson-Kendall-Roberts
<b>DMT</b>	Derjaguin–Muller–Toporov
<b>KPFM</b>	Kelvin Probe Force Microscopy
<b>PBS</b>	Phosphate Buffered Saline
<b>RMS</b>	Root Mean Square
<b>SiMoT</b>	Single Molecule Transistor
<b>SP</b>	Surface Potential
<b>V<sub>D</sub></b>	Drain-Source Voltage
<b>V<sub>G</sub></b>	Gate Voltage
<b>V<sub>T</sub></b>	Threshold Voltage

**zM** Zepto molar

## List of Symbols

**A** Oscillation amplitude

**A<sub>exc</sub>** Excitation amplitude

**C<sub>i</sub>** Capacitance per unit area

**LH** Lift height of the AFM tip

**E** Young's modulus (GPa)

**EGOFET** Electrolyte-Gated Organic Field Effect Transistor

**F<sub>ad</sub>** Adhesion force (nN)

**f<sub>0</sub>** Resonance frequency

**f<sub>d</sub>** Driving frequency

**I<sub>G</sub>** Gate leakage current

**I<sub>D</sub>** Drain current

**K** Stiffness (N/m)

**k<sub>B</sub>** Boltzmann constant

**c<sub>z</sub>** Cantilever spring constant

**L** Length of the transistor channel

**μFET** Field-effect mobility

**Q<sub>0</sub>** Quality factor of cantilever

**Sep<sub>min</sub>** Minimum separation distance during tip retraction

**Sep<sub>zero</sub>** Distance where force is zero

$V_D$  Drain-source voltage

$\Phi$  Phase lag

$\nu$  Poisson's ratio

# List of Figures

**Figure 1.1** The schematic illustrates a nanoindentation experimentation, showing load-displacement data as an AFM tip with a radius of curvature ( $R$ ) applies a vertical compressive force to indent a biological material to a depth ( $\delta$ ). The load-displacement curve, which includes both loading and unloading phases, is analyzed to conclude the mechanical characteristics of the sample. Reproduced from Ref. 33. ....5

**Figure 1.2** Experimental setup of the COIFM apparatus showing the force feedback mechanism based on voltage activation. The system combines an LS AutoProbe atomic force microscope with a DMASP cantilever tip, interfaced with an RHK SPM100 control unit. The setup employs optical beam deflection for detection. Reproduced from Ref. 34. ....6

**Figure 1.3** QCM-D technology measures two key variables: the sensor's frequency and its dissipation response. (a) The relationship between sensor thickness and oscillation frequency, showing frequency reduction upon molecular layer formation. Rigid thin films exhibit minimal dissipation. (b) Energy dissipation behavior of soft, thick, or viscoelastic films during oscillation, where frequency changes do not directly correlate with mass density. The high dissipation characteristics of hydrated biomolecular layers necessitate viscoelastic modeling for accurate analysis. Reproduced from Ref. 35. ....7

**Figure 1.4** Force versus time (part b) and force versus distance (part c) curves were generated through AFM-based force spectroscopy (AFM-FS. (1–3) The AFM tip contacts the sample, resulting in cantilever deflection due to repulsive forces. (3–5) The feedback system then retracts the sample, resulting in a downward deflection of the cantilever (5). Reproduced from Ref. 36. ....8

**Figure 1.5** Force–volume. (a) Schematic representation of FV mapping. (b) Various waveforms can be employed to modulate the displacement between the tip and the sample. Reproduced from Ref. 41. ....9

**Figure 1.6** Excitation and detection scheme. The cantilever is excited at its first two eigenmodes. When it interacts with the sample, the components of the tip's response are analyzed. This process produces multiple observable parameters. In bimodal AM-FM, the topography is acquired by maintaining  $A_1 = \text{constant}$  while two feedback loops act on the parameters of the 2nd mode. Reproduced from Ref. 41. ....9

**Figure 1.7** Schematic and scanning electron microscopy image of a torsional setup. Reproduced from Ref. 45. .... 11

**Figure 2.2 Schematic representation of the experimental configuration in Kelvin probe force microscopy.** During the second pass, the tip is lifted to a specified height and applied with an a.c voltage  $V_{AC}\sin(\omega t)$  and a d.c  $V_{DC}$ . The sample is grounded.....28

**Figure 3.1 Schematic illustration of the Au/anti-IgM surface patterning process, followed by a flowchart outlining the step of the sample preparation protocol for protein clusters and protein film.**.....31

**Figure 3.2 Frequency responses of the cantilever oscillation, including the magnitude (Mag signal) and phase (Phase signal).**.....33

**Figure 3.3 Resonance curve of the AFM cantilever, showing the power spectral density (PSD) as a function of frequency. The peak corresponds to the cantilever’s fundamental resonance frequency (304.75 kHz), having a quality factor of 498, used to calibrate the spring constant.**.....34

**Figure 3.4 Schematic illustration of the experimental setup for tuned oscillation AFM. The process sequence includes: (i) Generation of a cosine wave  $a_e\cos(t)=a_d\cos(2\pi f_d t)$  with constant frequency  $f_d$  and amplitude  $a_d$ ; (ii) Mechanical cantilever excitation via piezo element using this input signal  $a_e\cos(t)$ ; (iii) Detection and transmission of cantilever movement by optical sensing; (iv) Processing of amplitude  $A$  and phase difference  $\phi$  relative to input signal using lock-in detection; (v) Maintenance of constant amplitude  $A$  through feedback-controlled sample height adjustment. The resulting z-position data reveals surface features. Key parameters shown include the base separation  $d$  and minimum tip-sample gap  $D=d-A$  during oscillation cycles, where  $d$  represents the characteristic force distance. ....**35

**Figure 3.5 A typical amplitude/phase versus piezo displacement curves of on anti-IgM proteins physisorbed on gold substrate.**.....37

**Figure 3.6 Amplitude/phase versus piezo displacement curves of Anti-IgM proteins physisorbed on gold substrate (Raw data).**.....39

**Figure 3.7 Amplitude/phase versus piezo displacement curves of Anti-IgM proteins physisorbed on gold substrate (processed data). The first area marked in green, the tip is out of contact or free air region and it is approaching the sample. The light blue area corresponds to an decrease in  $\phi < -90^\circ$ , and the tip turns to be in attractive regime. Upon approaching the sample, the tip enters in a third region, named repulsive region (yellow) dominated by an increase of  $\phi$ . The shift of higher values is due to the transition from attractive to repulsive regime. The similar regions are marked for the amplitude profile. ....**40

**Figure 3.8 (a)Reconstructed tip-sample potential versus nearest tip-sample distance  $D=d-A$ : the origin of  $D$  has been arbitrarily defined such that  $D=0$  at the minimum potential, from the**

data points of the amplitude/phase versus distance curves of Anti-IgM proteins on gold substrate is shown in Figure 3.7, (b) Reconstructed tip-sample force versus nearest tip-sample distance D for anti-IgM proteins.....42

**Figure 3.9 Patterning of Au/anti-IgM surfaces.** (a) Flowchart outlining the protocol for sample preparation. (b) Optical image of the gold substrate patterned with anti-IgM, highlighting the region of the physisorbed protein layer with a blue dashed square. (c) Cyclic voltammograms recorded from the patterned anti-IgM gold sample by sweeping the potential between the sample and a reference electrode within a water-filled well. ....44

**Figure 4.1** (a) Semi-contact mode topography of a patterned Au/anti-IgM clusters at a concentration of 100 ng/mL anti-IgM, (b) Magnified view of the highlighted region, focusing on a single protein cluster, (c) Cross-section profiles along the lines given in panel b are displayed. ....47

**Figure 4.2** (a) Semi-contact mode topography of a patterned Au/anti-IgM film at concentration of 0.5 mg/mL anti-IgM, (b) Cross-section profiles along the lines given in panel a are displayed. ....48

**Figure 4.3** The representative outcomes of amplitude/phase versus distance curves on protein film (a,b) reconstructed tip-sample potential (c), tip-sample interaction force between AFM tip and anti-IgM protein film (d). The representative outcomes of amplitude/phase versus distance curves on protein clusters (f,g) reconstructed tip-sample potential (h), tip-sample interaction force between AFM tip and anti-IgM protein clusters (i). ....49

**Figure 4.4 Typical Energy Dissipation Profiles of Anti-IgM Structures.** The representative results of Energy loss characteristics are presented for anti-IgM clusters and anti-IgM film, respectively, as a function of the minimum distance between the AFM tip and the sample surface. ....52

**Figure 4.5 Mechanical characterization of Anti-IgM proteins (clusters vs. film).** (a) Young’s modulus distribution and the statistical comparison of protein clusters and film, (b) Stiffness distribution and the statistical comparison of protein clusters and film, (c) Adhesion force distribution and the statistical comparison of protein clusters and film, respectively. ...55

**Figure 4.6 AFM analysis of the Au/anti-IgM patterned surface.** (a) Representative topography image obtained in semi-contact mode. (b) Cross-sectional profile along the line marked in (a). (c) High-resolution images showcasing the morphologies of the gold (left) and anti-IgM (right) regions. (d) Comparative cross-sectional profiles from (c), demonstrating increased roughness in the bio-functionalized area (red) compared to the gold region (green). ....57

**Figure 4.7** (a) The transfer characteristics curves  $I_D - V_G$ , at a fixed  $V_D = -0.4$  V, and  $V_G$  ranging from 0.1 V to -0.5 V. (b)  $I_G - V_G$  gate leakage current, registered with  $V_G$  ranging from 0.1 V to -0.5 V, at a fixed  $V_D$  of -0.4 V. (c) Threshold voltage measured from the SiMoT device with an anti-IgM biofunctionalized gate. The device underwent sequential incubation, first in bare PBS to establish a baseline, followed by a PBS standard solution containing 3 fM IgG as a negative control, and finally in PBS standard solutions with IgM concentrations of 100 zM and 10 aM for the sensing experiment. ....58

**Figure 4.8** (a) Illustration of dual-pass Kelvin probe microscopy measurement setup. (b) Basic structure of the antibody molecule showing two  $F_{ab}$  segments and one  $F_c$  portion, with the dipole moment direction pointing from  $F_c$  to  $F_{ab}$  regions. (c) Topography, phase contrast, and surface potential maps were recorded concurrently during measurement. (d) The mean surface potential distribution is shown in the inset. ....61

**Figure 4.9 AFM analysis of the patterned Au/anti-IgM electrode surface.** (a) Cross-sectional representation showing the boundary between unmodified and anti-IgM functionalized gold regions, including height profile measurements across the interface. (b) Topographic AFM scans of the bare gold electrode. (c) Region showing transition between unmodified gold (left side) and antibody-modified gold (right side). (d) Surface scan of the anti-IgM modified gold region. Green dotted lines in (a) and (c) indicate the interface boundary. ....62

**Figure 4.10 Surface potential changes induced by affinity binding events.** (a) Cross-sectional diagram and (b) KPFM scan ( $90 \mu\text{m} \times 90 \mu\text{m}$ ) showing the boundary between bare Au (left) and anti-IgM modified gold (right) regions, where anti-IgM acts as the recognition layer. (c) Distribution plot showing surface potential differences (SPD) relative to the bare Au peak value. Sets {d,e,f}, {g,h,i}, and {l,m,n} mirror {a,b,c}, displaying cross-sections, KPFM measurements, and SPD distributions after sequential exposure to: non-specific IgG (3 fM) as negative control, specific IgM (100 zM), and higher concentration IgM (10 aM), as illustrated in panels d, g, and l. ....64

**Figure 4.11 Comparable responses observed in KPFM and SiMoT measurements of Au/anti-IgM electrodes at matching IgM levels.** (a) Surface potential difference changes ( $\Delta\text{SPD}$ ) measured at different IgM concentrations, referenced to bare gold values. Electrodes were tested with IgM (3 fM) and IgG solutions (100 zM, 10 aM, and 100 aM) in PBS. (b) Diagram showing SiMoT device configuration, with gate area of  $5 \times 10^{-1} \text{ cm}^2$  and anti-IgM density of  $2 \times 10^{12} \text{ cm}^{-2}$ . (c) Representative current-voltage characteristics ( $I_D$  vs.  $V_G$ ) at  $V_D = -0.4$  V for samples matching panel (a). (d) Threshold voltage shifts ( $\Delta V_T$ ) extracted from

transfer curves. Data points show means with standard deviations from triplicate measurements.....66

**Figure 4.12** SP changes induced by the formation of anti-IgM/IgM biocomplex and the corresponding histograms of the SP distributions.....69

## List of Tables

<b>Table 4.1 Mechanical properties of anti-IgM clusters and anti-IgM film.</b> The mean values presented include Young's modulus (E), stiffness (K), and adhesion force (Fad) for each sample type.....	56
---	----

## **Research Project**

The primary aim of this thesis is to characterize the mechanical properties of proteins, both in films and clusters, when physisorbed onto a solid state gold substrate, which is essential for the development of the single-molecule organic field-effect transistor (SiMoT) biosensor. Additionally, a diagnostic platform based on Kelvin Probe Force Microscopy (KPFM) is developed to explore the forces and dynamics between ligands and receptors during immunocomplex formation. The findings are applied to assess similar processes at the SiMoT active element, revealing the surface phenomena behind SiMoT's amplified response.

# Thesis Organization

## **Chapter 1:**

Chapter 1 provides an introduction and state-of-the-art on the nanomechanical properties and surface potential characterization of protein films, emphasizing their significance across various fields. It explores the techniques employed for investigating nanomechanical behavior, such as AFM, KPFM, and other advanced methodologies. The chapter also outlines key advancements in the field while identifying existing research gaps.

## **Chapter 2:**

Chapter 2 provides the theoretical background of the models and techniques used to study the nanomechanical properties, including Young's modulus, stiffness and adhesion forces and surface potential characterization of proteins films. The chapter also covers the principles and modes of AFM for high-resolution imaging and force measurement, along with dynamic force spectroscopy for nanoscale interactions. Additionally, it outlines KPFM for surface potential analysis, focusing on its use in studying protein interactions.

## **Chapter 3**

Chapter 3 covers the experimental methods and sample preparation procedures for AM-AFM, KPFM, Electrolyte-gated SiMoT, and single-molecule sensing. It provides comprehensive details on these techniques and the processes involved, as well as explanations of the data analysis methods used throughout the experiments.

## **Chapter 4:**

Chapter 4 is divided into two parts. Part one presents the results and discussion on the mechanical properties of both protein films and clusters. Part two focuses on the results and discussion related to KPFM and Electrolyte-gated SiMoT, analyzing their implications for surface potential characterization and single-molecule sensing.

## **Chapter 5:**

Chapter 5 will provide a comprehensive overview, beginning with a summary of the key findings from the study, emphasizing the main results and their implications. It will then discuss the significance of the work in advancing the understanding of protein films, particularly in terms of their nanomechanical and surface potential properties, and how these insights contribute to the broader field. The chapter will also outline recommendations for future work,

suggesting improvements to the experimental techniques and potential applications of the findings.

## Abstract

Amplitude Modulation Atomic Force Microscopy (AM-AFM) is a powerful technique used for high-resolution imaging and mechanical characterization of surfaces at the nanoscale. It excels in analyzing weak intermolecular forces, such as van der Waals and electrostatic interactions, which are crucial for understanding protein films and biofunctionalized surfaces in biosensing. This study employed AM-AFM to analyze the mechanical properties of anti-IgM protein physisorbed on stiff gold films on solid substrates, a process driven by weak intermolecular forces. The research examined the mechanical properties, including Young's modulus, stiffness, and adhesion forces, of both protein clusters and films. It is revealed that the anti-IgM protein films were more compact, and exhibited higher Young's modulus, stiffness and less adhesion force compared to the protein clusters. Energy dissipation patterns observed in AM-AFM further supported these findings. Protein clusters exhibited higher energy dissipation in the attractive regime, indicating that they are softer and less ordered. In contrast, protein films demonstrated lower dissipation due to their more compact, ordered arrangement. These results suggest that protein films are more resistant to deformation, making them suitable for biosensor applications where mechanical stability is crucial.

Additionally, Kelvin Probe Force Microscopy (KPFM) was utilized to measure surface potential changes resulting from antigen-antibody interactions, demonstrating its potential as a diagnostic tool for biosensing. KPFM is a non-invasive technique that measures the contact potential difference between a conducting cantilever tip and a sample surface, allowing simultaneous high-resolution topographic and surface potential imaging. The study demonstrated the effectiveness of KPFM in detecting surface potential shifts resulting from antigen-antibody binding, such as the interaction between anti-IgM biofunctionalized surfaces and IgM molecules. The formation of the immuno-complex caused a measurable decrease in surface potential, attributed to electrostatic interactions at the binding sites. The surface potential shift was detected across the entire functionalized area, even at extremely low IgM concentrations, highlighting KPFM's sensitivity in detecting single-molecule binding events. These results suggest that KPFM can serve as a label-free, highly sensitive diagnostic tool for detecting biomolecular interactions in biosensing platforms.

# Chapter 1 Introduction

Protein films mechanics is a relatively young, yet not well-developed area, that has rapidly gained importance. The effective functioning of proteins relies on a delicate balance between molecular stability and structural flexibility, both of which are influenced by their secondary structure and intramolecular interactions. [1] Understanding the nanomechanical behavior of protein films is crucial to support diverse applications, including industrial processes such as food processing, production of photographic emulsions, [2] enzyme activity, muscle contraction, [3] ligand-receptor interactions, [4] biomedical diagnostics, [5,6] and biosensors. [7] Additionally, protein layers are integral to material science and play a crucial role in developing novel biosensors and bioactive materials. [8,9]

The mechanical properties of protein films significantly affect their biological functions and structural integrity. Understanding the flexibility and deformability of proteins is essential as their functions are closely dependent on their three-dimensional structures. As a result, alterations in protein mechanics can contribute to various pathological conditions, including protein aggregation and immune responses that can be detected by biosensors. [6] Moreover, the mechanical properties of protein layers are vital for advancing our understanding of disease mechanisms, enabling the development of innovative diagnostic methods, and driving biosensor technology advancements. [9] The mechanical properties of antibodies, including, Young's modulus, stiffness, and adhesion force are integral to the development and performance of biosensors. These properties influence how well antibodies can be immobilized, their stability during use, and their ability to interact with target analytes effectively. Understanding and optimizing these mechanical characteristics are essential for creating reliable, sensitive biosensors capable of accurate biomolecular detection in various applications. The combination of suitable mechanical properties allows biosensors to achieve high sensitivity and specificity in detecting biomarkers for diseases such as cancer or infections. For instance, biosensors utilizing stanniocalcin-1 protein antibodies have demonstrated effective prostate cancer diagnostics due to their optimized mechanical characteristics. [10]

The orientation, configuration, and structural characteristics of protein films in bioactive materials, as well as their mechanical properties, have a critical role in mediating in

vivo responses. Research has shown that the mechanical characteristics of biomaterials can control the performance of biosensors and, for nanoparticles, impact the sensitivity and efficiency of molecular detection. Recent advancements in the use of Quartz Crystal Microbalance with Dissipation (QCM-D) for designing, synthesizing, and characterizing bioactive materials highlight the increasing significance of this field. [11] Furthermore, nanomechanical characterization of biomolecules presents new resources for designing novel materials and nanocomposites, as highlighted by Willner and co-workers. [12]

The rise of advanced force microscopy techniques, particularly AFM, has greatly advanced our understanding of protein mechanics. Colton and Burham conducted a pioneering study on nanomechanical properties using AFM in 1989. [13] This innovative research paved the way for subsequent studies, including Bhushan and Koinkar's demonstration of the versatility of AFM-based nanoindentation, which offers high spatial resolution with indentation depths on the nanometer scale. [14] AFM has become a versatile tool for exploring not only the mechanical properties but also the electric and magnetic properties of various surfaces, including biological samples and soft matter.

Early work using viscometers to measure the viscous and elastic shear moduli of protein films, such as ovalbumin and bovine serum albumin (BSA), provided foundational insights into the mechanical behavior of protein films. For instance, a study via modified Bernard's double-ring surface viscometer in 1992 revealed elastic shear moduli for ovalbumin and BSA, reflecting increasing rigidity and network strength as these films aged. A significant breakthrough occurred in 2002 with the development of the Cambridge Interfacial Tensiometer (CIT), which enabled precise measurement of the mechanical characteristics of protein films adsorbed at the air-water interface. This study revealed that  $\alpha$ -lactoglobulin films exhibited a surface elasticity modulus of around 100 mN/m, with higher protein concentrations leading to increased rigidity. [15] This was the first instance where conventional stress-strain analysis was utilized to gain insight into the mechanical behavior of adsorbed protein films, offering deeper insights into their functional properties.

The advent of AFM techniques opened up new possibilities for nanoscale investigations of protein mechanics. In 2005, researchers probed the mechanical properties of BCA II molecules immobilized on a silicon substrate, revealing tensile forces during the unfolding and refolding processes. [16] That same year, single-molecule force spectroscopy (SMFS) was

employed to study the temperature-dependent mechanical flexibility of proteins, demonstrating that higher temperatures significantly reduced protein stiffness due to a shift from hydrogen bond dominance to hydrophobic interactions. [17] Further, studies in 2007 focused on lactate oxidase (LOx) monolayers immobilized on gold substrates, showing Young's moduli varying from 0.5-0.8 GPa. [18] More recent studies have highlighted the mechanical characteristics of single proteins and complex structures. For example, a 2009 review outlined how AFM-based single-molecule force spectroscopy (SMFS) could be used to investigate the mechanical properties of the giant muscle protein titin, which exhibited mechanically stable domains, depending on the pulling speed. [19] Another 2011 study employed bimodal dynamic force microscopy, allowing for topographical and flexibility mapping of single proteins, revealing elastic modulus variations from 8 to 18 MPa. [20] These findings were corroborated by studies of single membrane proteins, such as bacteriorhodopsin (bR), which exhibited stiffness in the  $\alpha$ -helices while the interhelical loops displayed flexibility. [21] A 2015 study of human IgM and IgG antibodies further expanded the understanding of protein mechanics. In this work, fast force-volume AFM techniques with sub-10-nm spatial resolution were used to quantify the elastic stiffness and deformability. [21] This was followed by a 2016 study that characterized the stress-strain behavior of IgM antibody pentamers, revealing distinct elastic regimes and highlighting their mechanical flexibility. [22]

Recent advancements by our group on the mechanical behavior of the SARS-CoV-2 spike protein variants (alpha, beta, and gamma) illustrate the importance of studying protein mechanics in detail. Using AM-AFM combined with force spectroscopy, they characterized key nanomechanical parameters, including Young's modulus, stiffness, adhesion force, and the Hamaker constant. The alpha variant exhibited the highest rigidity, followed by the beta and gamma variants, which correlated with specific mutations. These mechanical insights have provided critical understanding of viral infectivity and binding affinity, paving the way for therapeutic interventions and vaccine development. [23]

Despite these significant advancements, there remains a notable gap in the literature concerning the nanomechanical behavior of certain biomolecules, particularly globular proteins like anti-IgM antibodies, when physisorbed on stiff substrates such as gold. This area represents an underexplored field within nanomechanical characterization, highlighting the need for further research to gain insight in the nanoscale mechanical behavior of these proteins. Immunoglobulin proteins are among the most abundant proteins, accounting for a significant

portion (28%) of total protein content, [24] and are used in developing biosensors for biomarker detection. The ongoing exploration of protein film mechanics, especially in underexplored areas such as globular proteins on stiff substrates, promises to yield crucial knowledge for optimizing the performance and stability of protein-based materials in various biomedical and technological applications.

Alongside mechanical properties, the surface potential of protein layers is another critical aspect that must be explored. KPFM is a powerful technique for measuring the surface potential of protein layers at the nanoscale. Understanding how surface potential changes under different conditions or upon binding with other molecules is vital for electrolyte-gated organic field-effect transistor (EGOFET) applications, where protein layers serve as functional components.

KPFM has become a widely used technique for imaging the surface potentials and charges of a variety of biological samples, including protein arrays, biomolecular monolayers, and single proteins. [25,26] Based on Lord Kelvin “vibrating capacitance method” KPFM measures the difference in work function between the AFM tip and the sample, offering high spatial resolution and sensitivity in identifying changes in surface potential.

KPFM allows for label-free detection of protein-small molecule interactions by identifying binding-induced changes in surface potential at the single-molecule level. [27] It has found application in studying organosilane self-assembled monolayers (SAMs) to measure distinct surface potentials and differentiate between molecular domains. Additionally, KPFM has been used in protein microarray technology, enabling the detection of antibody-antigen interactions with high reproducibility and resolution. [28] Further KPFM was used to study DNA hybridization and protein/DNA nanoarrays, for detecting charge variations associated with molecular binding events, providing crucial insights into biomolecular interactions. [29] Moreover, KPFM has been instrumental in characterizing organic thin films and nanostructures, mapping electronic processes, and optimizing the design of bioelectronic devices. [24,26]

## 1.1 Techniques for Studying Mechanical Properties

Attempts to explore the biomolecular interactions and mechanical characteristics of complex biosystems have been constrained for a long time due to the absence of suitable techniques. Although optical tweezers, [30] magnetic tweezers, [31] micropipette manipulation, [32] or surface force apparatus (SFA), [33] these techniques are highly sensitive for measuring force; however, they cannot simultaneously quantify and map these interactions structurally across wide force ranges. The more commonly used methods are explained below.

### 1.1.1 AFM based nanoindentation

Nano-indentation with AFM enables the evaluation of nanoscale topography and the determination of Young's modulus at specific sites within a biomolecule. This method involves pressing an AFM tip onto a protein sample to obtain force-displacement curves, which are subsequently analyzed to derive mechanical properties. [34]

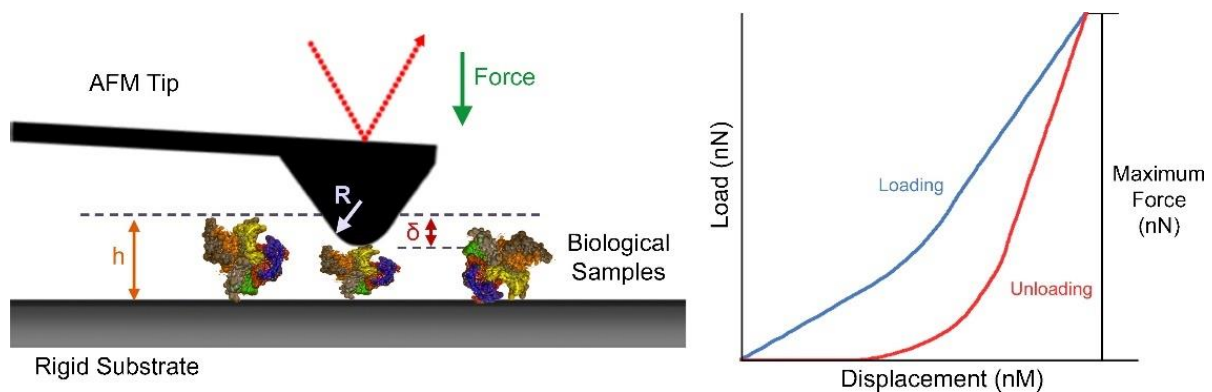


**Figure 1.1** The schematic illustrates a nanoindentation experimentation, showing load-displacement data as an AFM tip with a radius of curvature ( $R$ ) applies a vertical compressive force to indent a biological material to a depth ( $\delta$ ). The load-displacement curve, which includes both loading and unloading phases, is analyzed to conclude the mechanical characteristics of the sample. Reproduced from Ref. 33.

### 1.1.2 Cantilever-based optical interfacial force microscopy (COIFM)

COIFM is an advanced technique that combines AFM with optical detection methods to measure intermolecular forces at the nanoscale. Its sensitivity to environmental conditions can impact measurement accuracy, and it may encounter challenges with the snap-to-contact

phenomenon, making the analysis of force-distance curves more complex. [35]

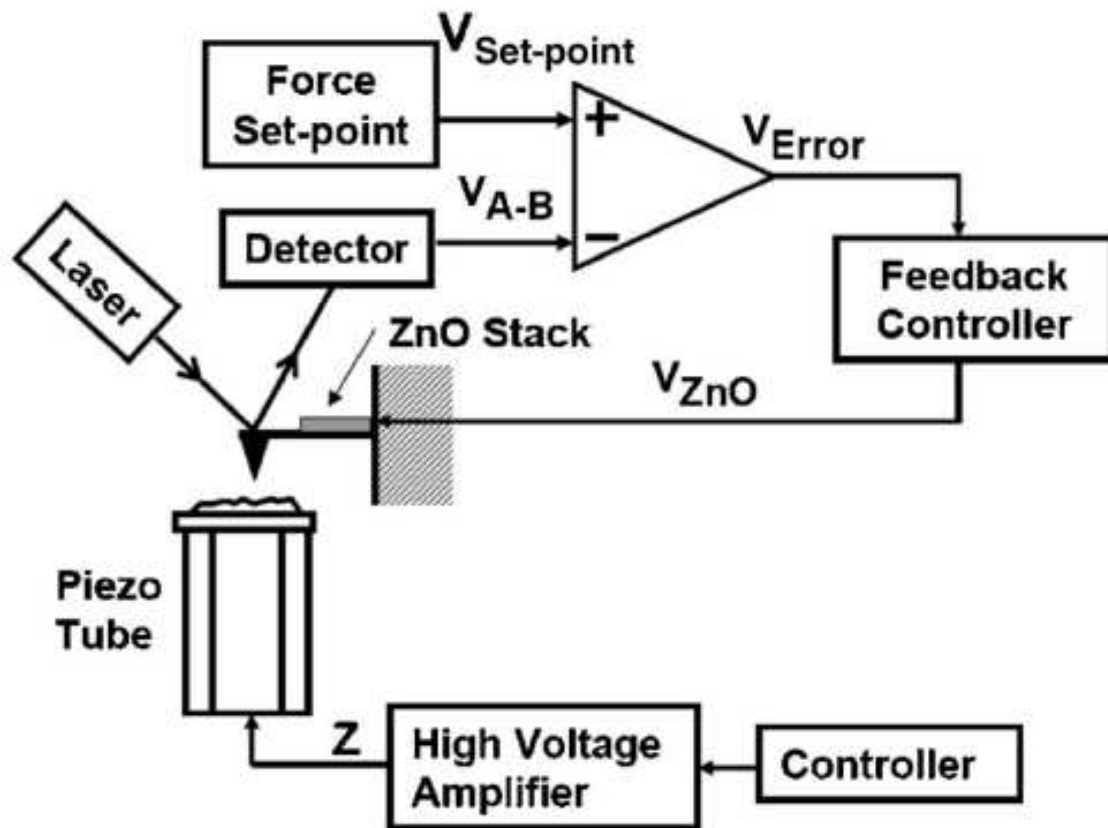


**Figure 1.2** Experimental setup of the COIFM apparatus showing the force feedback mechanism based on voltage activation. The system combines an LS AutoProbe atomic force microscope with a DMASP cantilever tip, interfaced with an RHK SPM100 control unit. The setup employs optical beam deflection for detection. Reproduced from Ref. 34.

### 1.1.3 Quartz crystal microbalance with dissipation (QCM-D)

The QCM-D offers another approach for nanoscale mechanical analysis. This technique employs acoustic resonance to measure both mass changes and viscoelastic characteristics of soft materials without requiring labels. Its key advantage lies in the ability to perform real-time measurements across different mediums, functioning effectively in both liquid and gas phases. The capabilities of QCM-D has significantly improved the study of bioactive materials, allowing for the analysis of protein structures on surfaces, investigation of cell adhesion, and development of sensing arrays for advanced biotechnological applications. [36]

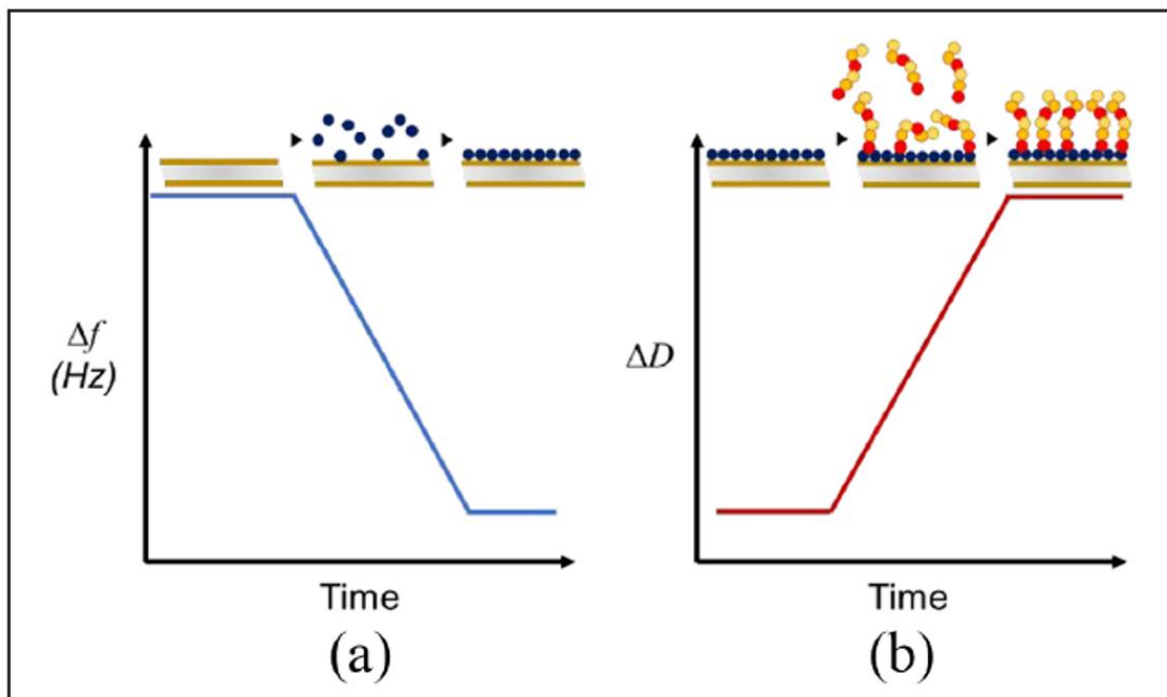


**Figure 1.3** QCM-D technology measures two key variables: the sensor's frequency and its dissipation response. (a) The relationship between sensor thickness and oscillation frequency, showing frequency reduction upon molecular layer formation. Rigid thin films exhibit minimal dissipation. (b) Energy dissipation behavior of soft, thick, or viscoelastic films during oscillation, where frequency changes do not directly correlate with mass density. The high dissipation characteristics of hydrated biomolecular layers necessitate viscoelastic modeling for accurate analysis. Reproduced from Ref. 35.

#### 1.1.4 Atomic force microscopy based force spectroscopy (AFM-FS)

Force–distance curves acquired from AFM offer insights into various sample properties. When the tip moves closer to the sample, interactions like electrostatic or van der Waals forces cause cantilever deflection, allowing for the calculation of elastic properties like deformation and stiffness. During retraction, adhesive forces result in downward deflection, which reveals information about adhesion force and work. [37–40]

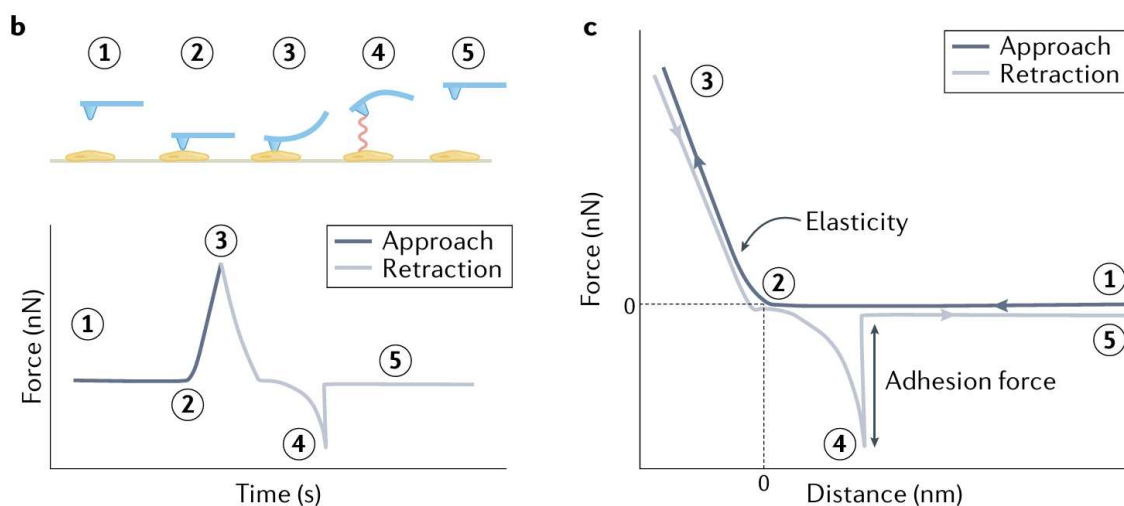


**Figure 1.4** Force versus time (part b) and force versus distance (part c) curves were generated through AFM-based force spectroscopy (AFM-FS). (1–3) The AFM tip contacts the sample, resulting in cantilever deflection due to repulsive forces. (3–5) The feedback system then retracts the sample, resulting in a downward deflection of the cantilever (5). Reproduced from Ref. 36.

### 1.1.5 Force-volume AFM

Force–volume (FV) is a commonly utilized technique for measuring mechanical characteristics at the nanoscale. This feature is integrated into the application modules of many commercial AFMs and enables the acquisition of arrays of spatially resolved force-displacement curves (FDCs) Figure 1.5a.

A variety of parameters can be derived from a FDC, with the most common height, Young's modulus, stiffness, adhesion force, and energy dissipation. Plotting these parameters as a function of spatial coordinates enables a comprehensive characterization of the interface. The adhesion force is determined by observing changes in deflection as the tip withdraws from the sample surface. Stiffness is directly measured from the slope of the force-displacement curve in the repulsive region. To determine Young's modulus, a section of the FDC dominated by repulsive forces is fitted to a contact mechanics model. Assessing viscoelastic properties requires a theoretical model to relate observables to underlying parameters.

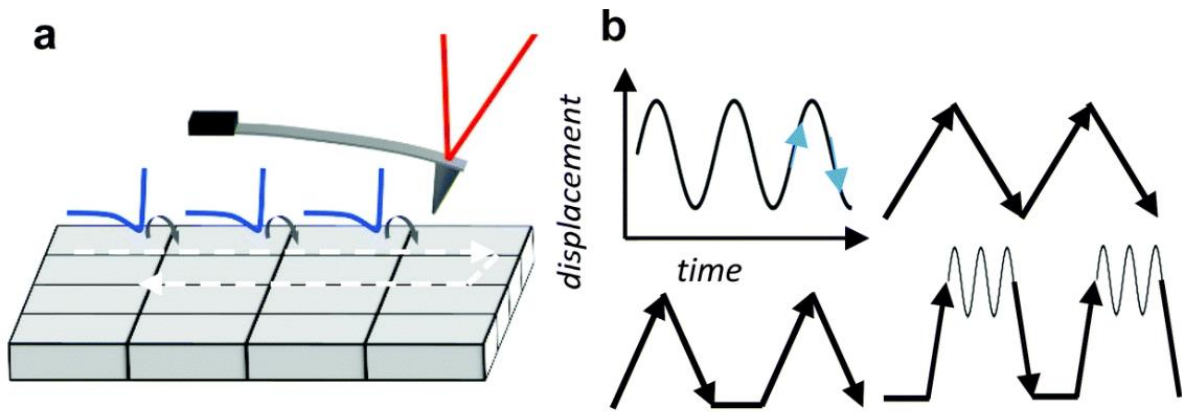


**Figure 1.5** Force–volume. (a) Schematic representation of FV mapping. (b) Various waveforms can be employed to modulate the displacement between the tip and the sample. Reproduced from Ref. 41.

### 1.1.6 Bimodal AFM

Bimodal AFM utilizes the simultaneous excitation and detection of two cantilever modes. This dual-mode approach enables the measurement of various material properties—such as topography, deformation, dissipation, elastic modulus, viscosity coefficients, and long-range interaction parameters—in a single imaging step. In bimodal AFM, the tip motion is analyzed by decomposing it into components that oscillate at the frequencies of the excited modes. [41]

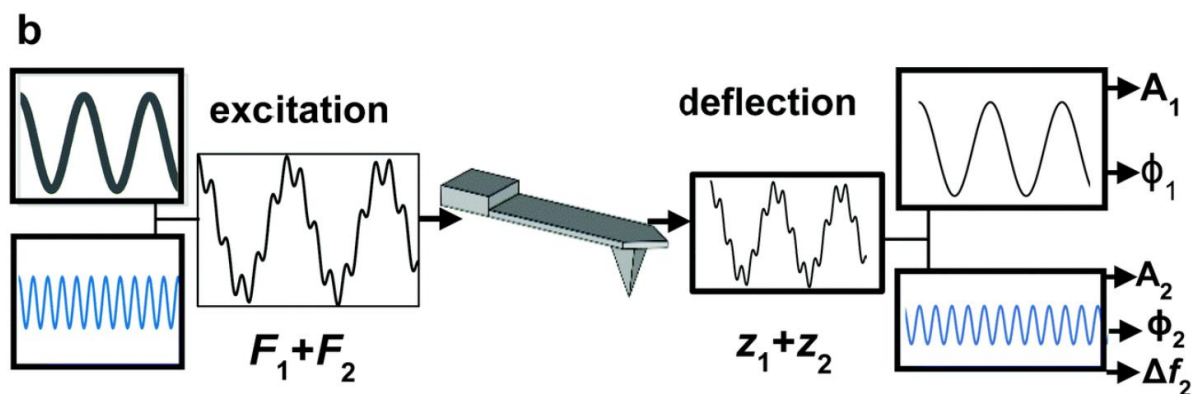


**Figure 1.6** Excitation and detection scheme. The cantilever is excited at its first two eigenmodes. When it interacts with the sample, the components of the tip's response are analyzed. This process produces multiple observable parameters. In bimodal AM-FM, the topography is acquired by maintaining  $A_1 = \text{constant}$  while two feedback loops act on the parameters of the 2nd mode. Reproduced from Ref. 41.

### **1.1.7 Contact resonance AFM**

This method tracks changes in the cantilever's resonant frequency resulting from variations in the mechanical properties of the tip-sample contact. In contact resonance atomic force microscopy (CR-AFM), the sample is subjected to ultrasonic frequencies while maintaining contact with the tip. The technique involves measuring the resonant frequency, amplitude, and phase shift of the cantilever-tip response, which are then compared to measurements taken when the tip is free-standing and not in contact with the sample. Theoretical models have been proposed to interpret these observations. For elastic contacts, the models associate the measured parameters with contact stiffness. In the case of viscoelastic contacts, the models relate the observations to both contact stiffness and damping coefficients. [42]

### **1.1.8 Multi-harmonic AFM**

Multi-harmonic AFM works by examining multiple harmonic components of the deflection signal during amplitude modulation AFM imaging, assuming periodic tip motion involving up to four harmonics of the drive frequency. This approach assumes that periodic oscillations correspond to a periodic tip-sample force, which can be represented as a Taylor series of harmonic components. Analytical expressions based on energy balance and the virial theorem connect the Fourier components to multi-harmonic observables, such as amplitudes and phase shifts. To convert these observables into material properties, a contact mechanics model is necessary. [43]

### **1.1.9 Torsional harmonic AFM**

This approach is based on collecting the higher harmonics of the torsional signal. [44] In conventional AM-AFM topographic imaging, the tip-sample force is determined by integrating the higher harmonic of the torsional signal. This method requires a specially designed cantilever, where the tip is positioned off-center from the cantilever axis, as illustrated in Figure 1.7. This design enhances torque around the cantilever axis, amplifying the generation of higher harmonics. By calculating the time-varying force, it becomes possible to measure local mechanical properties, such as Young's modulus.

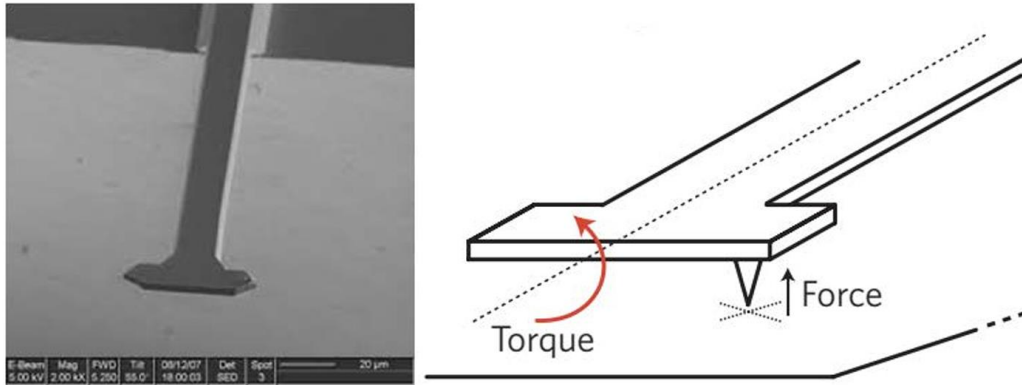


**Figure 1.7** Schematic and scanning electron microscopy image of a torsional setup. Reproduced from Ref. 45.

# Chapter 2 Theoretical Background

## 2.1 Protein films

Protein films are structured materials composed of protein molecules arranged into a thin, cohesive layer on a substrate. The structure and properties of these films can differ based on the fabrication method, the specific proteins involved, and the conditions under which they are formed. There are three primary strategies for generating protein films.

- Naturally self-assembling proteins
- Crosslinking of proteins using both physical and chemical methods
- Thermal/electrical treatment of proteins to initiate reorganization

Protein films are built upon the primary structure of proteins, which is the sequence of amino acids in a linear arrangement. This arrangement guides how proteins fold into their secondary structures, like alpha-helices and beta-sheets, which are essential for defining the film's overall structure. In protein films, these secondary structures tend to remain intact or may be slightly modified due to interactions with the substrate and surrounding environment. Proteins can also fold into tertiary structures, representing the three-dimensional arrangement of individual molecules, which influences the film's shape and behavior. When multiple protein molecules come together, they can form quaternary structures, organizing into larger complexes that contribute to the overall characteristics of the film.

The deposition method plays a critical role in revealing how protein molecules are arranged within a film. In self-assembled films, proteins tend to naturally orient and pack closely together due to intermolecular forces like hydrophobic interactions, van der Waals forces, and hydrogen bonding. On the other hand, films created through techniques like casting, spin coating, or dip coating may display more random orientations or alignments, influenced by the specific drying and curing conditions used during their formation.

Crosslinking methods, both physical and chemical, strengthen protein films by creating bonds between protein molecules, resulting in a more stable and cohesive network. Physical crosslinking allows for effective control of biophysical properties like strength, elasticity,

surface roughness, degradability, and biocompatibility. Chemical crosslinking, on the other hand, offers precise tuning of film characteristics, including mechanical strength, flexibility, and degradation rates. The final structural properties of the film—such as thickness, uniformity, and mechanical attributes like Young's modulus, stiffness, and adhesion—are shaped by the interaction between these molecular structures and the conditions during film formation. [45]

## 2.2 Theories related to mechanical Properties

Different models were considered for measuring mechanical properties involving (Young's modulus, stiffness and Adhesion force) in AFM-based experiments. The understanding of nano-mechanical interactions between an AFM tip and a sample surface relies on these models. Here are the models widely used for AFM-based mechanical property measurements.

### 2.2.1 Hertzian model

The Hertzian model accounts solely for elastic deformation, specifically focusing on contact between elastic materials [46]. Any adhesion phenomenon between the AFM tip and the sample surface is disregarded in the Hertzian model. Young's modulus within this model is given by the following expression: [47]

$$E = \frac{3(1-\nu)^2}{4r^{1/2}} \left\{ \frac{(F_{SP})^{2/3} - (F_{ATH})^{2/3}}{\text{Sep}_{SP} - \text{Sep}_{ATH}} \right\}^{3/2} \quad (2.1)$$

In this expression, E represents Young's modulus,  $\nu$  is Poisson's ratio and r is the AFM tip radius,  $F_{SP}$  and  $\text{Sep}_{SP}$  denote the force and distance at the setpoint (SP), while  $F_{ATH}$  and  $\text{Sep}_{ATH}$  refer to the force and distance at the 'approach engage threshold (ATH)', respectively.

### 2.2.2 Derjaguin–Muller–Toporov (DMT) model

The Derjaguin–Muller–Toporov (DMT) model is suitable for samples with a higher Young's modulus (greater than 1 GPa) and for adhesive materials. In contrast to the Hertzian model, the DMT model includes adhesion between the tip and the sample surface in its Young's modulus calculations, as shown in the following expression.

$$E = \frac{3(1-\nu)^2}{4r^{1/2}} \left\{ \frac{(F_{SP} - F_{RMA})^{2/3} - (F_{RTH} - F_{RMA})^{2/3}}{\text{Sep}_{SP} - \text{Sep}_{RTH}} \right\}^{3/2} \quad (2.2)$$

where  $F_{SP}$  and  $\text{Sep}_{SP}$  represent the force and the separation distance at the setpoint (SP).  $F_{RTH}$  and  $\text{Sep}_{RTH}$  denote the force and the distance at ‘retract engage threshold (RTH), while  $F_{RMA}$  indicates the force at the ‘retract minimum adhesion (RMA) position. [47]

### 2.2.3 Johnson–Kendall–Roberts (JKR) model

The Johnson-Kendall-Roberts (JKR) model is ideal for soft materials with a Young’s modulus below 1 GPa and significant adhesive properties. The primary distinction between the DMT and JKR models lies in the range of adhesion forces. The DMT model accounts for long-range adhesion forces, even before contact, whereas the JKR model only includes adhesion forces at the point of contact. [48] The Young’s modulus is expressed as follows:

$$E = \frac{3}{4}(1-\nu)^2 \left\{ \frac{1 + 16^{1/3}}{3} \right\}^{3/2} \frac{F_{min}}{(r(\text{Sep}_{zero} - \text{Sep}_{min})^3)^{1/2}} \quad (2.3)$$

where  $F_{min}$  represents the minimum force at  $z = \text{Sep}_{min}$  and  $\text{Sep}_{zero}$  is the distance where the force becomes zero during the retraction. [47]

### 2.2.4 Sneddon Model

The Sneddon model extends the Hertzian theory to non-spherical indenters and does not consider for long-range forces. For AFM tips that are conical, pyramidal, or cylindrical, the Sneddon model is utilized to relate the indentation depth to the applied force. The formula is given below.

$$F = \frac{E \tan \alpha}{1 - \nu^2} \frac{\delta^2}{\sqrt{2}} \quad (2.4)$$

where  $\theta$  is the half-angle of the indenter (for a conical tip),  $E$  represents the Young’s modulus,  $\delta$  denotes the indentation depth, and  $\nu$  is the Poisson ratio respectively. This model is commonly applied when AFM tips are not spherical, such as with sharper or more complex tip geometries, allowing for accurate mechanical property measurements with non-ideal tip shapes. [49,50]

### 2.2.5 Oliver-Pharr Method

It is widely used in nanoindentation experiments to evaluate the hardness and elastic modulus of materials. The unloading portion of the force-displacement curve is analyzed during AFM nanoindentation. [51,52] This method is mostly useful to quantify materials' mechanical properties when large, permanent deformations occur. This model calculates the reduced modulus from the slope of the unloading curve and uses that to determine the material's hardness and elastic modulus. The following formula describes the Young's modulus.

$$E = \frac{\sqrt{\pi}}{2} (1 - \nu^2) \frac{S}{\sqrt{A_c}} \quad (2.5)$$

where  $\nu$  represents the Poisson's ratio,  $S$  denotes the stiffness, and  $A_c$  is the projected area at the contact depth. The Oliver-Pharr method is valuable in extracting properties like hardness and Young's modulus from AFM indentation measurements, particularly in metallic and ceramic materials. [53]

## 2.3 Principles of AFM

The AFM serves as a versatile tool, enabling the imaging of biological system topography at nanometer resolution under physiological conditions, as well as the quantification of biophysical properties and molecular interactions. The AFM functions by detecting the forces between a sharp tip positioned at the end of a flexible cantilever and the sample surface. The fundamental principle of AFM is based on the relationship between force and cantilever deflection, as described by Hooke's law:

$$F = k \cdot \Delta z \quad (2.6)$$

where  $F$  represents the force exerted between the tip and the sample,  $k$  denotes the spring constant (or stiffness) of the cantilever, and the deflection of the cantilever is denoted by  $\Delta z$ . In AFM, cantilevers typically have spring constants in the range of 0.01-10 N/m, making them highly sensitive to the small forces, often in nano newton (nN) range, that occur at the atomic scale. [54]

When the cantilever engages with the sample surface, the forces between the tip and the surface induce deflection of the cantilever. This deflection is precisely measured by directing a laser beam off the cantilever onto a position-sensitive photodiode. The deflection amount is directly proportional to the force between the tip and the sample. Either the cantilever

or the sample is moved by a piezoelectric scanner, enabling the tip to scan across the surface in the x and y directions. The position of the cantilever in the z-direction is adjusted by a feedback loop, enabling precise control over the force applied by the tip.

By monitoring these forces and controlling the tip's position, AFM generates high-resolution images of a sample's surface and provides detailed insights into its topography and mechanical properties., with spatial resolutions down to the nanometer scale. AFM is capable of measuring a broad range of forces, typically spanning from as low as 5 piconewtons (pN) to over 100 nanonewtons (nN), and can evaluate stiffness values ranging from approximately 100 pascals (Pa) to the lower gigapascal (GPa) range. [55]

The effective tip-sample interaction force comprises a combination of various force contributions.

#### **Van der Waals forces:**

The interaction between temporarily induced electric dipoles in atoms and molecules creates these attractive forces. When measuring the interaction between two separate molecules, the strength of these forces typically decreases with the seventh power ( $-1/z^7$ ) of the distance between them. [56] When analyzing van der Waals forces in macroscopic objects, scientists often use a simplified approach that treats solid objects as groups of separate molecules that don't affect each other. The total force can then be calculated by adding up the individual molecular contributions. This method is particularly useful when calculating the van der Waals force between a spherical object and a flat plane expressed as

$$F_{vdw}(z) = -\frac{A_H R}{6z^2} \quad (2.7)$$

In this equation, the sphere's radius is denoted by R, and  $A_H$  represents the Hamaker constant, which typically has a value of approximately 0.1 aJ. This geometric configuration is commonly used to model the van der Waals interactions between a microscope tip and a sample surface. Since these forces decrease with the square of the distance ( $1/z^2$ ), they are considered to act over longer distances compared to other forces that affect atomic force microscopy measurements. [57]

### Capillary forces:

When experiments are conducted in normal atmospheric conditions, moisture from the air accumulates on both the sample and the microscope tip, creating a thin layer of water molecules. As the tip moves closer to the sample's surface, it must move through this moisture layer. At the point where the tip meets the sample, the water molecules form a bridge-like structure (meniscus) between the two surfaces, resulting in a powerful attractive pull. This strong attraction can be problematic when examining delicate materials, as it may inadvertently alter or damage the sample's surface structure. [58]

### Elastic forces:

Physical contact between the microscope tip and the sample can result in elastic changes to both surfaces. These changes affect how much of the tip interacts with the sample, making it essential to understand both the elastic forces involved and how the materials deform during contact. This aspect of surface interaction was first mathematically explored in the late 19th century (1881), when Heinrich Hertz developed a theoretical framework for calculating the repulsive forces that develop when a sphere elastically deforms a flat surface upon contact. [58]

$$F_{\text{Hertz}}(z) = \frac{4}{3} E^* \sqrt{R} (z_0 - z)^{3/2} \text{ for } z \leq z_0 \quad (2.8)$$

where the effective elastic modulus  $E^*$

$$E^* = 1 / ((1 - \mu_t^2) / E_t + (1 - \mu_s^2) / E_s) \quad (2.9)$$

The mathematical model depends on several key material properties: Young's moduli ( $E_{t,s}$ ) and Poisson ratios ( $\mu_{t,s}$ ) of both the microscope tip and the sample surface. Additional important parameters include the radius of the tip ( $R$ ) and the initial position where the tip first makes contact with the surface ( $z_0$ ).

### Chemical binding forces:

When molecules from the microscope tip come very close to the surface molecules, their electron orbitals can interact and create distinct chemical bonds. These interactions occur only at extremely small distances and are particularly useful for achieving atomic-level

resolution when imaging surfaces, especially in vacuum conditions. Since these interactions vary depending on the specific molecules involved, researchers can use AFM measurements to investigate and identify the chemical composition of different atoms on a surface. [59]

### **Magnetic and electrostatic forces:**

Magnetic and electrostatic interactions can push surfaces apart or pull them together, and these forces can act over relatively large distances. Scientists typically study these forces by keeping the microscope tip separated from the sample surface, using what's known as non-contact mode. To detect magnetic forces, researchers must use tips made from or coated with magnetic materials. For studying electrostatic forces, it's necessary to carefully control the electrical potential difference between the tip and the sample.

### **AFM modes**

The main AFM modes include contact mode, non-contact mode, and dynamic modes, each with its unique strengths and limitations. Tapping mode AFM is a commonly employed technique that excels in high-resolution imaging of delicate and soft samples. By intermittently contacting the surface, it minimizes damage and adhesion issues while reducing lateral forces. This approach effectively overcomes challenges posed by friction, electrostatic forces, and other interfering factors, enabling accurate measurements of samples that are difficult to study with other AFM modes.

## **2.4 Theory of the dynamic mode**

In dynamic operation, two detection modes are frequently utilized: amplitude modulation (AM) and frequency modulation (FM) AFM. Dynamic AFM, particularly in amplitude modulation (AM-AFM) mode, is widely used for imaging applications. However, dynamic force measurements are less common due to the complexities involved in signal analysis caused by the non-linearity of the tip-sample force, which leads to instabilities and hysteresis. Employing dynamic techniques for force measurement, rather than static methods, offers numerous advantages. E.g., it allows for the measurement of dissipative forces at higher frequencies, enhances stability by minimizing susceptibility to snap-to-contact issues, and increases sensitivity when utilizing stiffer cantilevers. [60] Different methodologies in the

literature are introduced to reconstruct the force-distance curves in AM-AFM. A small amplitude solution to the force inversion problem in AM-AFM was developed by O'Shea et al. [61] Holscher and co-workers [62,63] developed a large amplitude solution by simplifying the integral equation assuming that the amplitudes in AM mode exceed the interaction range of the tip-sample force. Lee and Jhe [64] derived a method to measure the forces from amplitude and phase measurements for arbitrary amplitudes. Hu and Raman [65] adopted a different method, approximating the force using a series expansion in Chebyshev polynomials. Katan et.al method is based on an ad hoc equivalence between frequency modulation and AM-AFM observables [66] Garcia and co-workers also derived a different methodology for reconstructing the force by assuming that the amplitude and phase shift of the oscillation are slowly varying functions of the probe-surface separation. [67] Dynamic modes, particularly AM-AFM, are fundamental for studying the mechanical characteristics of materials at the nanoscale, and a detailed exploration of their theoretical underpinnings will provide deeper insights into their capabilities and applications.

#### 2.4.1 Equation of motion

The fundamental equation of motion relating the cantilever's behavior in dynamic mode. [63,68]

$$m\ddot{z}(t) + \frac{2\pi f_0 m}{Q_0} \dot{z}(t) + c_z(z(t) - d) = a_{exc} c_z \cos(2\pi f_d t) + F_{ts} [z(t), \dot{z}(t)] \quad (2.10)$$

Here,  $z(t)$  represents how the tip's position changes over time  $t$ , while  $c_z$  indicates the cantilever's spring constant. The effective mass is shown as  $m$ ,  $Q_0$  represents the quality factor, and  $f_0 = \sqrt{(c_z/m)/(2\pi)}$  denotes the cantilever's natural frequency. Looking at the right side of the equation, we find two main components. The first component describes the external force that drives the cantilever's oscillation, characterized by a constant amplitude ( $a_d$ ) and frequency  $f_d$ . The second component accounts for the nonlinear force  $F_{ts}$  that occurs between the tip and sample. The parameter  $d$  represents the equilibrium position of the tip.

#### 2.4.2 Driven and self-driven cantilevers

To study the specific characteristics of AM-mode, it is helpful to first study the distinction between the two driving terms. For simplicity, we consider that the cantilever is

vibrating far from the sample surface, allowing us to neglect the tip-sample forces ( $F_t \equiv 0$ ). This assumption simplifies the equation of motion (eq. 2.10) considerably. We will abandon this constraint later. Initially, we focused on the case where DFM operates in AM-mode. In these conditions, the equation of motion simplifies to the well-known form of a driven and damped harmonic oscillator:

$$m\ddot{z}(t) + \frac{2\pi f_0 m}{Q_0} \dot{z}(t) + c_z(z(t) - d) = a_{\text{exc}} c_z \cos(2\pi f_d t) \quad (2.11)$$

The cantilever oscillates at the driving frequency  $f_d$  as a result of the external driving force. Thus, the steady-state solution can be represented using the subsequent ansatz.

$$z(t \gg 0) = D + A + A \cos(2\pi f_d t + \phi) \quad (2.12)$$

where  $\phi$  denotes the phase difference between the excitation and the cantilever's oscillation. By employing this ansatz, we derive two functions that describe the amplitude and phase curves:

$$A = \frac{a_{\text{exc}}}{\sqrt{\left(1 - \frac{f_d^2}{f_0^2}\right)^2 + \left(\frac{1}{Q_0} \frac{f_d}{f_0}\right)^2}} \quad (2.13)$$

$$\tan \phi = \frac{1}{Q_0} \frac{f_d/f_0}{1 - f_d^2/f_0^2} \quad (2.14)$$

In contrast, the scenario when the cantilever is completely self-driven has received significantly less attention in the literature. In this case, the resulting equation of motion can be simplified to:

$$m\ddot{z}(t) + \left(\frac{2\pi f_0 m}{Q_0}\right) \dot{z}(t) + c_z(z(t) - d) = -\frac{a_{\text{exc}}}{A} c_z z(t - t_0) \quad (2.15)$$

Since the cantilever is not driven by an externally fixed frequency, it acts as the frequency-defining element. So, we propose the following ansatz: [69]

$$z(t \gg 0) = d + A \cos(2\pi f t) \quad (2.16)$$

By introducing this ansatz into Equation 2.16 and substituting it into Equation 2.15, we derive two coupled trigonometric equations:

$$a_{\text{exc}} \cos(2\pi f t_0) = \frac{f_0^2 - f^2}{f_0^2} \quad (2.17a)$$

$$\frac{a_{\text{exc}}}{A} \sin(2\pi f t_0) = \frac{1}{Q_0} \frac{f}{f_0} \quad (2.17b)$$

With the assumption that the time shift  $t_0 = 1/(4f_0) = 90^\circ$ , is set to a specific value, the two equations can be decoupled, which simultaneously corresponds to the most common choice for  $t_0$ . For this value, the solution of Equation 2.18 is expressed as follows:

$$f = f_0 \quad (2.18a)$$

$$A = a_{\text{exc}} Q_0 \quad (2.18b)$$

This simple calculation highlights the unique behavior of a self-driven oscillator when the phase (or time) shift is set to  $90^\circ$ . In this scenario, the cantilever oscillates precisely at its natural frequency  $f_0$ . As indicated by Equation 2.18a, this specific feature leads to the definition of resonance when this condition is met. Furthermore, Equation 2.18b illustrates the linear relationship between the oscillation and excitation amplitude. [62,69]

## 2.5 Theory of the AM-MODE

The analysis begins by examining the cantilever's behavior when it's far from the sample. At this distance, we can ignore the tip-sample interactions in the relevant equation 2.11, which simplifies the system to a basic driven-damped harmonic oscillator. However, the situation becomes more complex as the cantilever approaches the sample surface. At closer distances, the force between the tip and sample  $F_{\text{ts}}$  becomes significant and affects how the cantilever oscillates. The main difficulty lies in the complex nature of real tip-sample interactions, which introduce strong nonlinear elements into the motion equation 2.10. This nonlinearity makes it challenging to find direct mathematical solutions. To make practical sense of DFM data, researchers focus on analyzing the steady-state behavior, where the cantilever moves in a sinusoidal pattern. This approach allows the tip-sample force to be broken down using Fourier series analysis, making the mathematics more manageable.

$$\begin{aligned}
F_{ts} [z(t), \dot{z}(t)] &\approx f_d \int_0^{\frac{1}{f_d}} F_{ts} [z(t), \dot{z}(t)] dt \\
&+ 2f_d \int_0^{\frac{1}{f_d}} F_{ts} [z(t), \dot{z}(t)] \cos(2\pi f_d t + \phi) dt \\
&\times \cos(2\pi f_d t + \phi) \\
&+ 2f_d \int_0^{\frac{1}{f_d}} F_{ts} [z(t), \dot{z}(t)] \sin(2\pi f_d t + \phi) dt \\
&\times \sin(2\pi f_d t + \phi)
\end{aligned} \tag{2.19}$$

where  $z(t)$  is represented by Equation 2.12.

The average tip-sample force over one complete oscillation cycle is represented by the first term in the Fourier series, that causes a slight shift in the equilibrium position of the oscillation by a small offset  $\Delta d$  from  $d$  to  $d_0$ . However, the original values of  $\Delta d$  are typically very small. For the amplitudes commonly used in AM-AFM (ranging from a few nanometers to tens of nanometers), the average tip-sample force falls within the range of a few piconewtons. [62] The resulting offset  $\Delta d$  is smaller than 1 pm for standard sets of parameters. Since this is significantly beyond the resolution limit of an AM-AFM experiment performed in air, we disregard this effect in the following and assume  $d \approx d_0$  and  $D = d - A$ . For further analysis, the first harmonics of the Fourier series from Equation 2.19 are inserted into the equation of motion in Equation 2.10, leading to the formation of two coupled equations.

$$\frac{f_0^2 - f_d^2}{f_0^2} = I_+(d, A) + \frac{a_d}{A} \cos \phi \tag{2.20a}$$

$$-\frac{1}{Q_0} \frac{f_d}{f_0} = I_-(d, A) + \frac{a_d}{A} \sin \phi \tag{2.20b}$$

where the following integrals have been defined:

$$I_+(d, A) = \frac{2f_d}{c_z A} \int_0^{\frac{1}{f_d}} F_{ts} [z(t), \dot{z}(t)] \cos(2\pi f_d t + \phi) dt \tag{2.21a}$$

$$\begin{aligned}
&= \frac{1}{\pi c_z A^2} \int_{d-A}^{d+A} (F_{\downarrow} + F_{\uparrow}) \frac{z-d}{\sqrt{A^2 - (z-d)^2}} dz \\
I_-(d, A) &= \frac{2f_d}{c_z A} \int_0^{\frac{1}{f_d}} F_{ts} [z(t), \dot{z}(t)] \sin(2\pi f_d t + \phi) dt \\
&= \frac{1}{\pi c_z A^2} \int_{d-A}^{d+A} (F_{\downarrow} - F_{\uparrow}) dz \tag{2.21b} \\
&= \frac{1}{\pi c_z A^2} \Delta E(d, A)
\end{aligned}$$

Both integrals depend on the oscillation amplitude  $A$  and the distance  $d$  between the cantilever and the sample. They also rely on both the sum and difference of the tip-sample forces during approach ( $F_{\downarrow}$ ) and retraction ( $F_{\uparrow}$ ), which are marked with the labels "+" and "-" for clarity. The integral  $I_+$  represents a weighted average of the tip sample forces ( $F_{\downarrow} + F_{\uparrow}$ ). In contrast, the integral  $I_-$  is directly associated with  $\Delta E$ , which represents the energy dissipated during each oscillation cycle. As a result,  $I_-$  becomes zero for purely conservative tip-sample forces, where  $F_{\downarrow}$  and  $F_{\uparrow}$  are identical. Equation 2.20 can be utilized to compute the resonance curves of a dynamic force microscope, incorporating tip-sample forces. The findings are

$$A = \frac{a_d}{\sqrt{\left(1 - \frac{f_d^2}{f_0^2} - I_+(d, A)\right)^2 + \left(\frac{1}{Q_0} \frac{f_d}{f_0} + I_-(d, A)\right)^2}} \tag{2.22a}$$

$$\tan \phi = \frac{\frac{1}{Q_0} \frac{f_d}{f_0} + I_-(d, A)}{1 - \frac{f_d^2}{f_0^2} - I_+(d, A)} \tag{2.22b}$$

Equation 2.22a characterizes the shape of the resonance curve, however, as it is an implicit function of the oscillation amplitude  $A$ , it cannot be plotted directly. [70]

## 2.6 Dynamic force spectroscopy using the AM-AFM

Tip-sample potential in the AM-AFM mode can be determined using the integral equation. [62,63]

$$U_{ts}(D) = 2c_z \int_D^{\infty} K(z) \left[ (z-D) + \sqrt{\frac{A}{16\pi}} \sqrt{z-D} + \frac{A^{3/2}}{\sqrt{2(z-D)}} \right] dz, \quad (2.23)$$

Where

$$K(D, A) = \frac{1}{2} \left[ \frac{a_{exc}}{A} \cos \varphi + \frac{f_0^2 - f_d^2}{f_0^2} \right] \quad (2.24)$$

The final term in this integral equation diverges as  $z=D$ . To prevent numerical problems associated with this pole, apply the transformation  $z = D + t^2$  and used the transformed equation.

$$U_{ts}(D) = 4c_z \int_0^{\infty} K(D + t^2) \left[ t^3 + \sqrt{\frac{A}{16\pi}} t^2 + \frac{A^{3/2}}{\sqrt{2}} \right] dt \quad (2.25)$$

For the measurement of the tip-sample force, fitting a 4th-order polynomial to the potential and the negative gradient is calculated as follows.

$$F_{ts} = -\frac{\partial U_{ts}}{\partial D} \quad (2.26)$$

where  $D=d-A$  is the nearest tip-sample distance

## 2.7 Energy dissipation in AM-AFM

Additional insight in to the tip-sample interaction can be gained by observing that the integral  $I_-$  is directly related with the energy dissipation  $\Delta E$ . Combining Equations 2.14 and 2.21b, we get.

$$\Delta E = \left( \frac{1}{Q_0} \frac{f_d}{f_0} + \frac{a_{exc}}{A} \sin \phi \right) \pi c_z A^2 \quad (2.27)$$

The same result was previously reported by Cleveland [71] using the conservation of energy principle. However, building on Cleveland's work, the energy dissipation is plotted as a function of the nearest tip-sample distance  $D=d-A$  to match the same scaling as that of the tip-sample force.

## 2.8 Kelvin Probe Force Microscopy (KPFM)

### 2.8.1 Principles of KPFM

The Kelvin probe method, which takes its name from Lord Kelvin (William Thomson), emerged in 1898 as a way to understand how metals develop natural electrical potential differences at their contact points. [72] The work function (WF,  $\phi$ ) represents the smallest amount of energy required to remove an electron from a material's lowest energy state. In metallic materials,  $\phi$  equals the energy gap between the Fermi level and the vacuum state of an electron (Figure 2.1a). When considering semiconductors or insulating materials, the work function measures the energy required to move electrons from their weakest bonds within the material to the vacuum level. [73]

As shown in Figure 2.1b, connecting two capacitor plates made of distinct materials causes electron flow from the plate with a lower work function (material 2, where electrons are less tightly bound) towards the plate with a higher work function (material 1, where electrons are more strongly bound). The transfer of electrons generates opposing charges, establishing a contact potential difference (CPD) between the materials. This creates a measurable electric field in the capacitor. By applying an external voltage  $V_c$ , the field can be neutralized. At equilibrium, when the field reaches zero, this applied voltage equals the CPD, which reflects the work function difference between the two materials, as illustrated in Figure 2.1c.

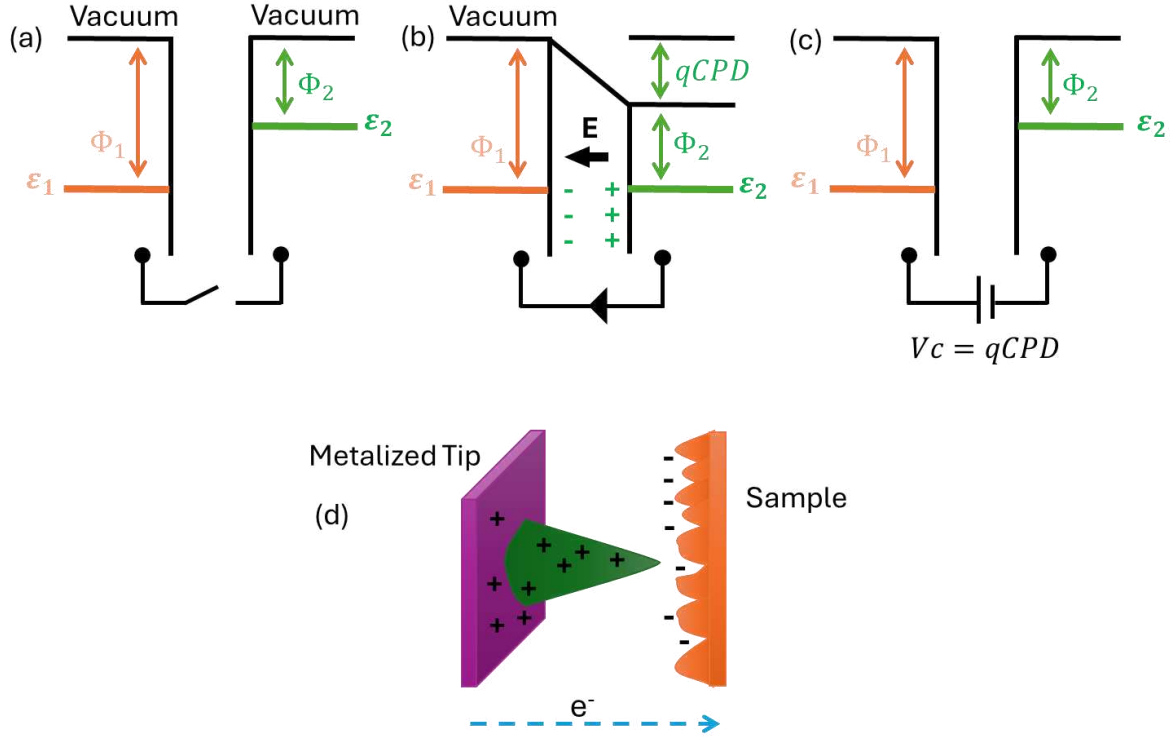


**Figure 2. Schematic diagram of Kelvin Probe physics.** (a) Materials 1 and 2 possess different work function, denoted as  $\phi_1$  and  $\phi_2$  (b) When contacted, electrons flow from Material 2 to Material 1 until their Fermi levels are aligned, resulting in a contact potential  $V_b$  and an electric field  $E$ . (c) Applying an external potential  $V_c=V_b$  cancels this electric field. (d) The Contact Potential Difference (CPD) arises between the AFM tip and the sample.

KPFM employs a probe-sample configuration that functions like a capacitor, where interactions arise from their distinct work functions. These forces can be modified by introducing voltage to either component. The technique uses a combined voltage signal: a direct current (d.c.) component plus an alternating current (a.c.) component. When the a.c. frequency matches the probe's natural resonance, the probe's mechanical response becomes significantly stronger than what would be observed using only d.c. voltage.

Mathematical derivations demonstrate that the magnitude of force experienced by the oscillating capacitor varies in direct proportion to the potential difference between the sample surface and the scanning probe.

$$f_{CAP} \approx f_{CAP}(\omega_{KP}) = \frac{dC}{dZ} \Delta V_{DC} \Delta V_{AC} \sin(\omega_{KP}t) \quad (2.28)$$

where  $C$  represents capacitance,  $Z$  denotes separation,  $\Delta V_{DC}$  and  $\Delta V_{AC}$  are the direct current and alternating current voltage differences between the probe and substrate respectively, while  $\omega_{KP}$  indicates the resonant frequency of the Kelvin probe. [74,75]

The applied d.c. voltage is fine-tuned until the oscillating deflection of the probe is minimized. At this point, the force between the capacitor plates is at its minimum, and the voltage reflects the difference in work functions between the two plates. Mapping this d.c. voltage reveals the distribution of surface potential across the sample, referred as the Contact Potential Difference (CPD) distribution.

KPFM generates images that depict the local CPD distribution, with the magnitude depending on the tip material and its properties. However, when the same probe is used to investigate different surface regions, the tip potential serves as a CPD reference, allowing for a relative comparison of CPD values across various functionalized regions of the sample.

This research employs dual-scan Kelvin probe microscopy to map potential variations across surfaces resulting from precise antibody-antigen binding interactions. The initial scan captures surface features using tapping mode AFM with mechanical cantilever oscillation. In the subsequent scan, the probe follows the previously recorded topography at a defined height above the surface to determine the electric surface potential (SP). During this pass, the cantilever is electrically excited rather than mechanically through the application of voltage ( $V_{tip}$ ) with both ac + dc components to the tip. [76]

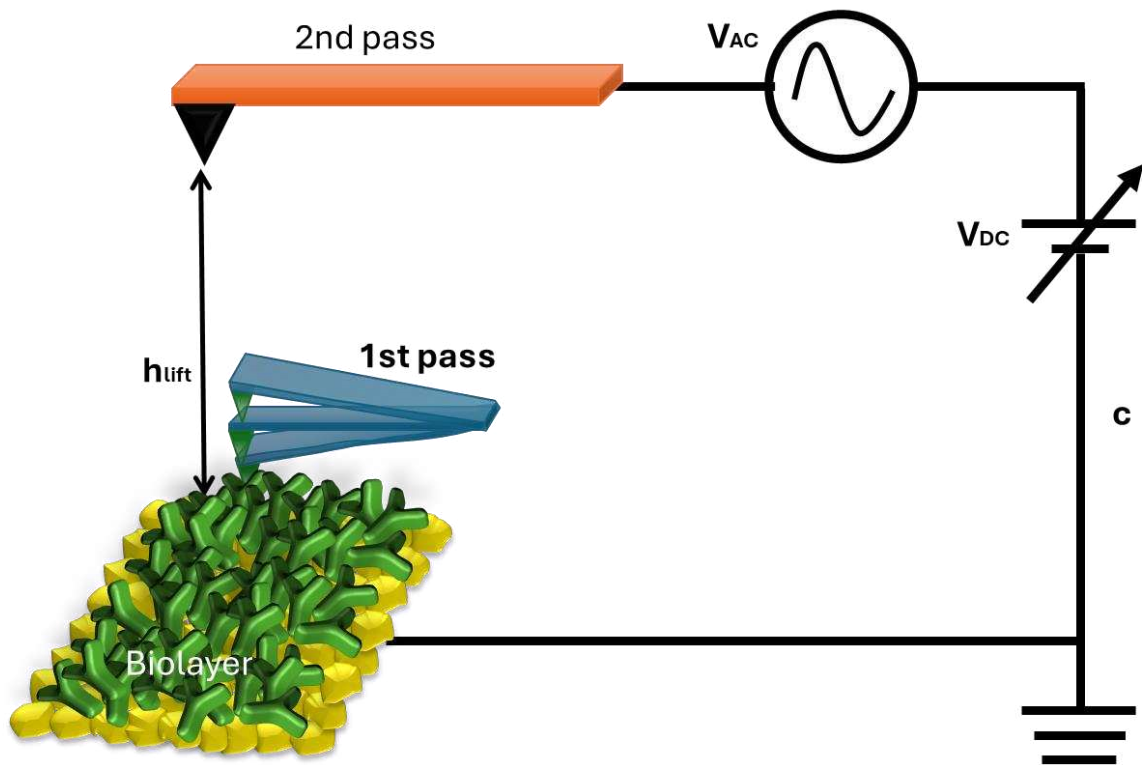


*Figure 2.1 Schematic representation of the experimental configuration in Kelvin probe force microscopy. During the second pass, the tip is lifted to a specified height and applied with an a.c voltage  $V_{AC}\sin(\omega t)$  and a d.c  $V_{DC}$ . The sample is grounded.*

## Chapter 3 Experimental Methods

Several methods are used for the formation of protein films, such as casting, printing methods, electrospinning, spin coating, and dip coating. [45,77] We employed dip coating to facilitate the physisorption of protein molecules onto the stiff substrate, leading to the formation of a thin, adherent protein film driven by weak intermolecular forces, including Van der Waals forces, and other forces like hydrogen bonding, electrostatic interactions, hydrophobic interactions. The physisorption of antibodies, or proteins in general, onto solid surfaces, is captivating and one of the most simplest and sustainable methods for the biofunctionalization phenomenon that is crucial in various fields of material science, particularly in the development of biomaterials and biosensors. This approach is cost-effective, quick, and suitable with printing technologies. [78] As it does not involve chemical coupling reactions or modifications, it is also considered environmentally friendly. Additionally, it offers valuable insights into fundamental protein-protein interactions that govern protein adhesion and aggregation. Despite these benefits, physisorption is not commonly used in biosensing platforms due to a prevalent belief that a stable, high-performance biosensor requires a conjugated layer of biological recognition elements. Additionally, concerns about poor homogeneity and long-term stability have contributed to its limited use. [79] However, bioelectronic sensors with physisorbed capture layers have successfully demonstrated reliable and stable detection of clinically significant biomarkers (such as proteins, pathogens, DNA/RNA, and peptides) directly in biofluids at the single-molecule level. Physisorption is commonly utilized to graft proteins and DNA onto organic semiconductor layers, such as P3HT, pentacene, and PEDOT, within FET instrument. This method has been adopted in the following articles. [80–83]

### Part 1 (AM-AFM)

#### 3.1 Materials

The research utilized commercially available reagents and materials throughout the study. Avantor supplied the HPLC-grade water, VLSI-grade 30% hydrogen peroxide, and VLSI Selectipur-grade 96% sulfuric acid. The team sourced polyclonal antibodies, including anti-human immunoglobulin M (anti-IgM), from Sigma-Aldrich, applying them without further

purification. For our buffer solution, we used phosphate-buffered saline (PBS) from Sigma-Aldrich, which maintained a pH of 7.4 at room temperature and had an ionic strength of 162 mM.

### **3.1.1 Biofunctionalization protocol**

Substrate preparation and biofunctionalization were performed as follows: The experimental substrates were obtained by cutting rectangular pieces (10 mm × 5 mm) from silicon wafers that had been doped with arsenic and coated with a 300 nm layer of SiO<sub>2</sub>. Initial cleaning involved 10-minute ultrasonic baths in two steps: first using acetone, then 2-propanol, followed by nitrogen drying. A 5nm layer of Ti and a 50 nm thick layer of Au were subsequently applied via electron-beam evaporation. The substrates underwent cleaning in a 3:1 mixture of sulfuric acid and hydrogen peroxide (piranha solution) followed by HPLC water rinsing and nitrogen drying. Before the biofunctionalization, the gold-plated samples undergo a 10-minute treatment in a UV-ozone cleaner. The biofunctionalization protocol is illustrated in Figure 3.1. Gold-plated substrates were dip-coated in a PBS solution of anti-IgM (0.5 mg mL<sup>-1</sup>) at 21°C for 150 minutes. The functionalized surfaces received extensive sequential washing treatments: first in PBS, then in water, followed by spin-drying at 3000 rpm for 60 s to remove the non-tightly physisorbed proteins. A stable layer remains on the sample. This immobilization approach has some advantages due to its simplicity and cost-effectiveness.

The formation of anti-IgM clusters followed an analogous protocol. Gold-plated substrates were immersed in PBS solution with anti-IgM ( $100 \text{ ng mL}^{-1}$ ) for 150 minutes, maintaining a temperature of  $21^\circ\text{C}$ .

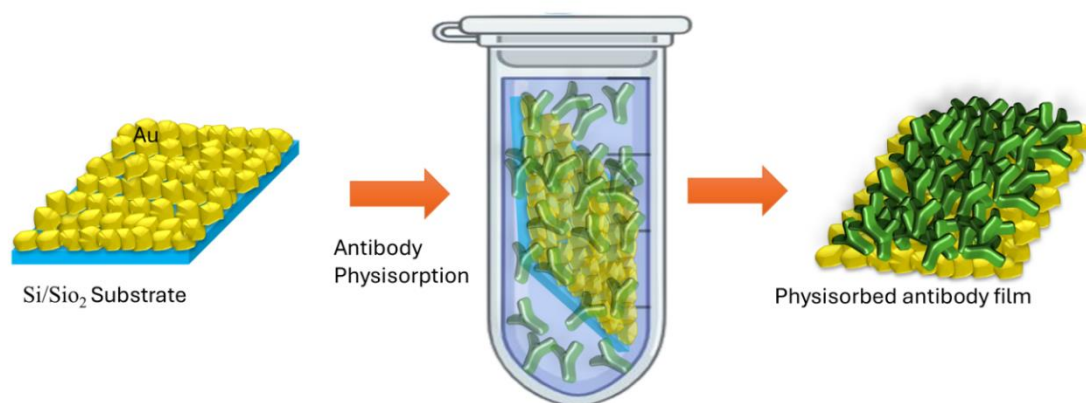


**Figure 3.1** Schematic illustration of the Au/anti-IgM surface patterning process, followed by a flowchart outlining the step of the sample preparation protocol for protein clusters and protein film.

### 3.1.2 AFM measurements

AFM measurements were carried out using an NT-MDT system NTEGRA Spectra (Moscow, Russia) in semi-contact mode, with an antimony-doped Si cantilever from Bruker (Model RTESPA-300) with a nominal tip radius of 10nm, resonance frequency 304.71kHz, spring constant of  $36.77 \text{ Nm}^{-1}$  and quality factor of 498. The Sader method was applied to measure the spring constant. A metallic clamp was used to ground the sample. Scanner calibration was performed at the start of each experiment to achieve accurate probe placement over the protein specimens. The process involved monitoring capacitance changes along all three axes (X, Y, and Z) while applying triangular voltage signals ( $\pm 300 \text{ V}$ ) to the corresponding piezo scanner segments. This is carried out prior to each experimental session, and corrections are applied as needed to maintain the linearity of the piezo response. The detailed calibrations are given below.

### 3.1.3 AFM Setup and Calibration

## **System Initialization**

Turn on the AFM system, including the main controller, AFM head, and computer interface. The system is allowed to stabilize to reach optimal operational conditions, ensuring that all the system components, such as electronics and the AFM head, have reached thermal equilibrium.

## **Mounting the sample**

The samples having dimensions 10 mm × 5 mm were securely mounted on the AFM stage with the use of double-sided adhesive tape. Ensure the sample is flat and properly aligned to prevent any tilt, which could influence the precision of the measurements.

## **Cantilever Installation and Tip Positioning**

The AFM cantilever install into the holder, ensuring it is properly seated without any tilt. Using an optical microscope, the cantilever tip was accurately positioned.

## **Piezo Scanner Calibration**

Calibrate the piezo scanners by applying a saw-tooth voltage ( $\pm 300$  mV) to the X, Y, and Z axis. Measure the capacitance displacement in each direction to ensure linear response and introduce corrections if necessary. This calibration ensures precise positioning and movement of the AFM probe above the sample surface.

## **Laser and Photodetector Alignment**

**Laser Alignment:** The laser alignment knobs are adjusted to position the laser spot onto the back of the cantilever, ideally close to its free end. This maximizes the sensitivity of the deflection measurement. The laser signal intensity is verified using the AFM (Nova Px) software.

**Photodetector Alignment:** The position of the photodetector is calibrated to align the laser signal on the detector quadrant. The vertical deflection (DFL) and lateral force (LF) values are

monitored. Proper alignment is achieved when DFL is near zero, indicating no pre-existing cantilever deflection.

### Resonance Curve Acquisition

A frequency sweep is performed near/at the expected resonance frequency of the cantilever. The lock-in amplifier measures the oscillation phase and amplitude as a function of frequency, generating the resonance curve shown in Figure 3.2.

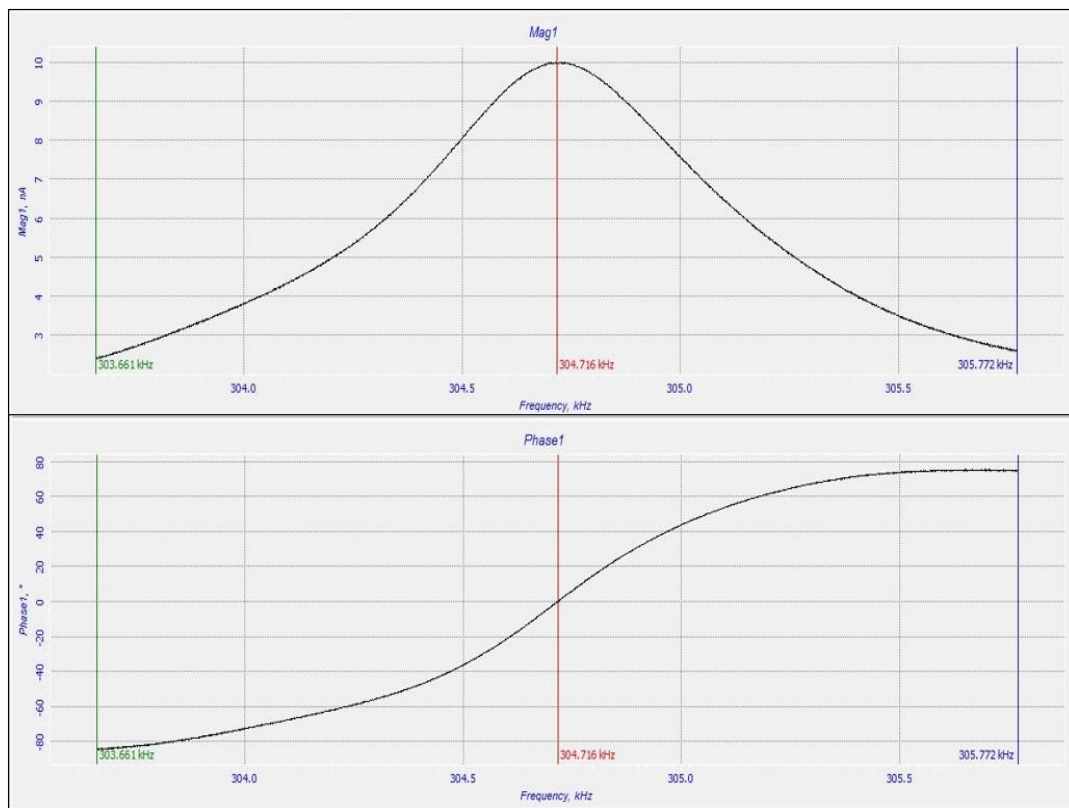


**Figure 3.2** Frequency responses of the cantilever oscillation, including the magnitude (Mag signal) and phase (Phase signal)..

### Cantilever Calibration

Reliable measurements of mechanical properties at the nanoscale depend on understanding the exact specifications of the employed cantilever. Among these parameters, determining the spring constant with accuracy presents a particularly significant technical challenge.. This calibration is essential for accurate force measurements and interpretation of AFM data. Probe calibration was performed using Sader method. [84]

## Sader method

The method requires the plan view dimensions of the rectangular cantilever, which includes a length of 123  $\mu\text{m}$ , a width of 40  $\mu\text{m}$  and a thickness of 3.3  $\mu\text{m}$ . Furthermore, the peaks' resonant frequency and quality factor are also required. These values are usually acquired by analyzing the thermal noise spectra of the unloaded AFM cantilever and fitting the response of a Simple Harmonic Oscillator (SHO) to the resonant peak of the fundamental power spectrum.

$$k = 0.1906\rho_f b^2 L Q_f \Gamma_i(\omega_f)\omega_f^2 \quad (3.1)$$

Equation 3.1, establishes a direct relationship between the spring constant  $k$ , the plan view dimensions of the cantilever,  $w_f$  which is the fundamental mode resonant frequency, and the quality factor denoted as  $Q_f$ . This expression is applicable as long as the quality factor  $Q_f > 1$ , This condition is generally met when the cantilevers are placed in air. The spring constant, determined using the Sader method, was  $36.77 \text{ Nm}^{-1}$ .

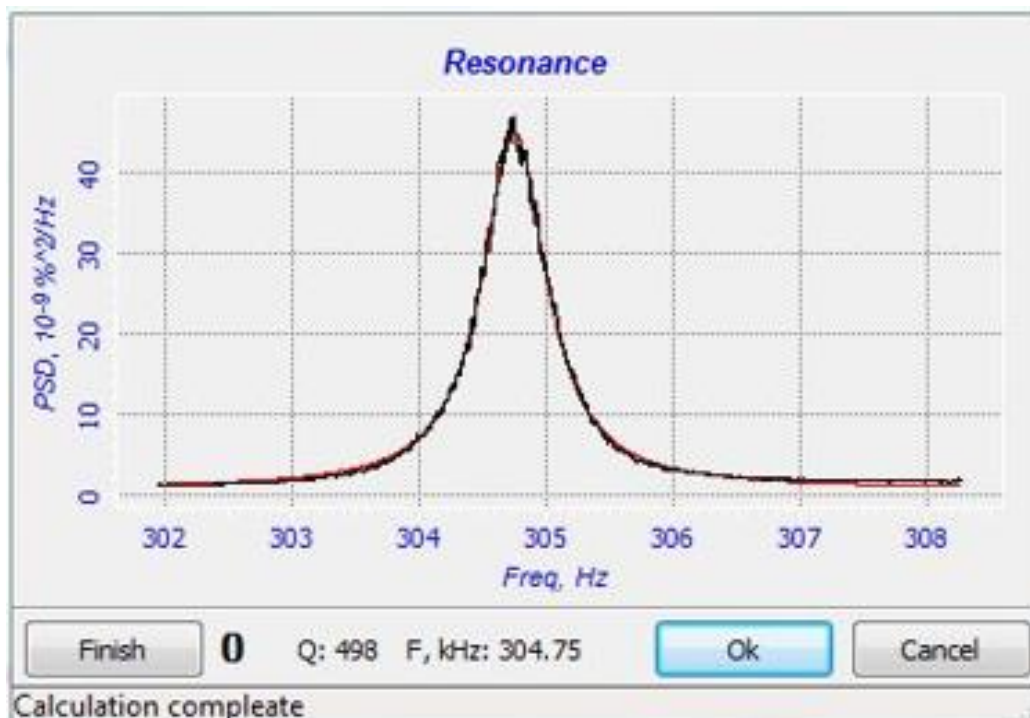


**Figure 3.3** Resonance curve of the AFM cantilever, showing the power spectral density (PSD) as a function of frequency. The peak corresponds to the cantilever's fundamental resonance frequency (304.75 kHz), having a quality factor of 498, used to calibrate the spring constant.

### 3.1.4 Topography measurement:

Set the free amplitude ( $A_0$ ) between 10-15 nm. Engage the feedback loop and adjust the set point amplitude ( $A_{sp}$ ). The areas of  $2 \times 2 \mu\text{m}^2$  were scanned at a scanning speed of 0.5Hz, with a resolution of 500 pixels per line for the anti-IgM clusters. For anti-IgM film, the areas of  $1 \times 1 \mu\text{m}^2$  were scanned at a scanning speed of 0.5Hz, with a resolution of 1000 pixels line per line. During scanning in the defined area with the optimized parameters, Monitor the real-time data to ensure that the feedback loop remains stable and the oscillation amplitude is consistent. The Topography for the anti-IgM clusters and Anti-IgM film are shown below. All measurements were conducted in air at room temperature (21 °C) and the images were processed using Image Analysis software.

### 3.1.5 Dynamic force spectroscopy

After acquiring the topography, switch to the AM-AFM mode to collect the amplitude and phase curves at amplitude setpoint ratio ( $A_{sp}/A_{free} \sim 1$ ). Detection of the oscillation amplitude and phase difference between cantilever driving and oscillation was accomplished using a lock-in amplifier. It is assumed that the tip oscillates between  $D=d-A$  and  $D+2A=d+A$ .

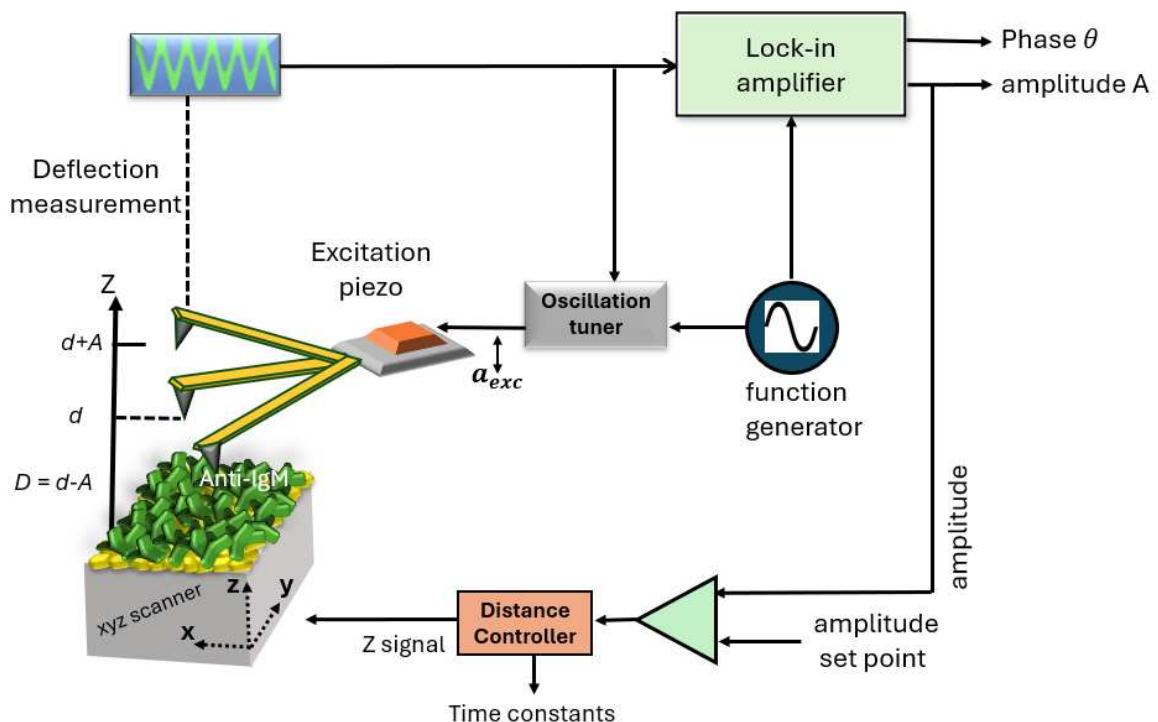


**Figure 3.4** Schematic illustration of the experimental setup for tuned oscillation AFM. The process sequence includes: (i) Generation of a cosine wave  $a_{exc}(t)=ad\cos(2\pi fdt)$  with constant

*frequency  $f_d$  and amplitude  $a_d$ ; (ii) Mechanical cantilever excitation via piezo element using this input signal  $a_{exc}(t)$ ; (iii) Detection and transmission of cantilever movement by optical sensing; (iv) Processing of amplitude  $A$  and phase difference  $\phi$  relative to input signal using lock-in detection; (v) Maintenance of constant amplitude  $A$  through feedback-controlled sample height adjustment. The resulting  $z$ -position data reveals surface features. Key parameters shown include the base separation  $d$  and minimum tip-sample gap  $D=d-A$  during oscillation cycles, where  $d$  represents the characteristic force distance.*

Figure 4.1 presents the semi-contact mode AFM topography of Au/anti-IgM clusters formed at an anti-IgM concentration of 0.1 mg/mL. Panel (b) provides a magnified view of the highlighted region, focusing on an individual protein cluster. Upon identification of clusters in the topography image, amplitude-distance and phase-distance curves were obtained at positions indicated by 'x' symbols. The height of each cluster was measured individually, ranging from 7 to 14 nm. These force spectroscopy measurements were conducted using identical parameters: a ramp rate of 0.5 Hz, a ramp distance of 15-20 nm, and a resolution of 1,000 points per line. Figure 4.2 depicts the semi-contact mode AFM topography of a patterned Au/anti-IgM film, revealing a uniform layer with a height of 6nm. Force spectroscopy measurements, including amplitude/phase-distance curves, were acquired in  $4 \times 4$  arrays across multiple regions of the biofunctionalized sample. These measurements were carried out in quintuplicate under the following parameters: ramp rate of 0.5 Hz, ramp distance of 15-20 nm, and a resolution of 1,000 points per line.

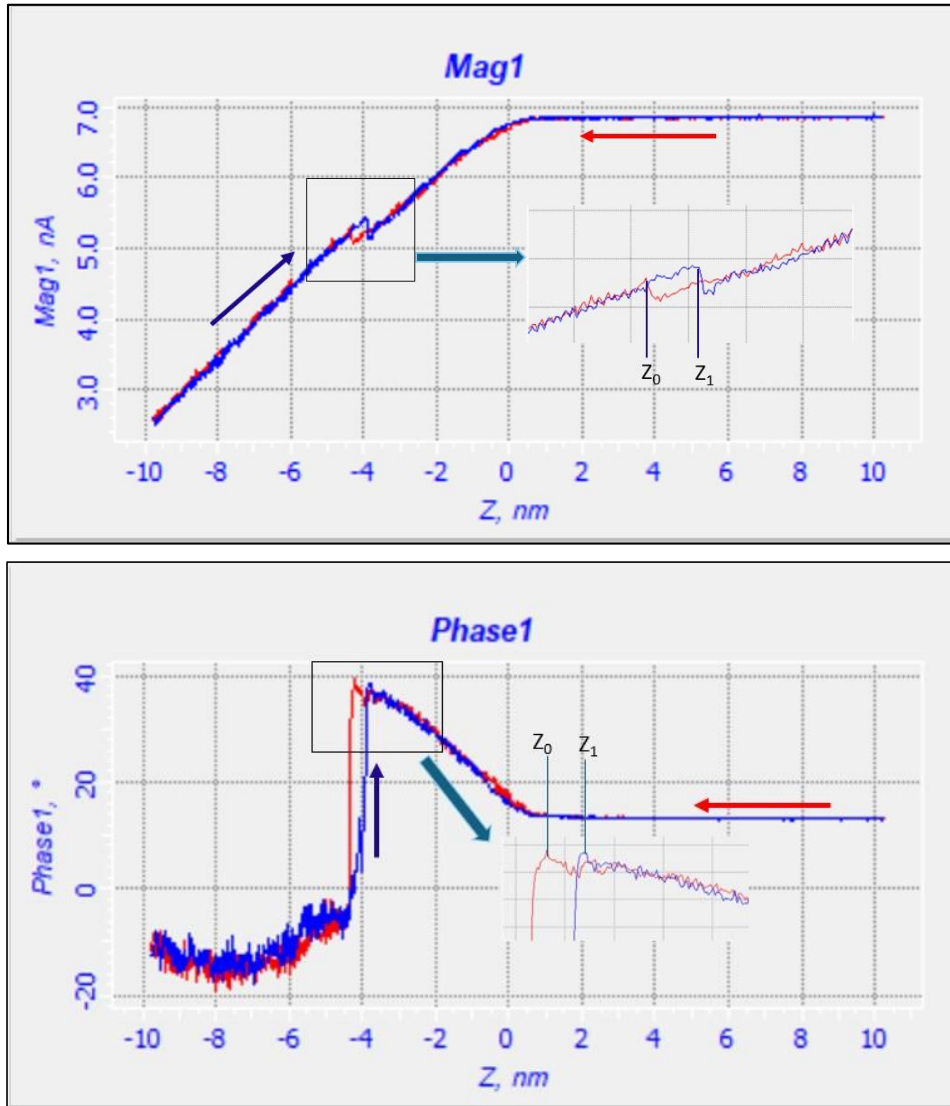


**Figure 3.5** A typical amplitude/phase versus piezo displacement curves of on anti-IgM proteins physisorbed on gold substrate.

As shown in Figure 3.5, when the resonating probe approaches the protein specimen, its vibration magnitude gradually diminishes. The amplitude exhibits a linear reduction with proximity to the surface over a limited range. Upon reaching a critical separation  $z_0$ , a jump occurs where the oscillation suddenly increases, producing an upward displacement of the damping profile. Upon retracting the tip, another discontinuity appears at a greater distance  $z_1 > z_0$ , where the amplitude returns to its original value. Consequently, a hysteresis is observed in the amplitude versus distance curve. The phase signal measured simultaneously also exhibits variations at the same distinct distances ( $z_0$  and  $z_1$ ) as the amplitude signal. The step observed in both amplitude/phase curves at a specific distance is associated with the onset of the repulsive region of the surface potential. This point, therefore, signifies the shift from non-

contact oscillation (purely attractive interaction) to tapping mode (involving both attractive and repulsive interactions). In tapping mode, typical cantilever oscillation amplitudes range from  $10\pm 100$  nm. [85]

When the probe is positioned far from the protein specimen, changes in separation have no effect on oscillation magnitude. As the gap narrows, the amplitude begins to diminish due to emerging tip-surface interactions. These forces can encompass multiple phenomena, including electrostatic attraction, hydrophobic effects, molecular adhesion, van der Waals forces, and both short/long-range interactions. The amplitude curves feature a local maximum, resulting from the interplay between attractive and repulsive interaction regions.

## **3.2 Data Analysis**

### **3.2.1 Methods for Analyzing AM-AFM Data**

Two variables, corresponding to the observables, amplitude ( $A$ ) and phase ( $\phi$ ) are recorded as a function of piezo displacement and later converted to force-distance curves. The topographic information is obtained from the feedback loop, while the phase difference between excitation and the detected cantilever signals reveals details about the specimen's compositional features and dissipative characteristics. [62]

Different methodologies were introduced to reconstruct the force-distance curves in AM-AFM already discussed in chapter 2. We adopt the Algorithm proposed by Hendrik Holscher [63] to transform the Amplitude/phase curves to the tip-sample force. The detailed theoretical background for the algorithm is provided in chapter 2.

The detailed method is described below for one set of Amplitude and phase curve.

The raw data acquired from AM-AFM measurements comprises two primary curves: amplitude versus piezo displacement and phase versus piezo displacement. The amplitude signal, initially measured in nano amperes (nA), represents the current signal as a function of the z-piezo displacement, which corresponds to the cantilever-sample separation as measured by the microscope. Concurrently, the phase signal is recorded in degrees as a function of the z-piezo displacement.

To convert the amplitude signal from nA to nm, the following procedure is implemented:

1. The slope within the linear region of the Mag(nA) versus z-piezo displacement curve is calculated.
2. The slope, expressed in nA/nm, serves as a conversion factor.
3. The amplitude in nanometers is then derived by multiplying the original amplitude values (in nA) by this conversion factor:  $\text{Amplitude (nm)} = \text{Slope} * \text{Amplitude (nA)}$

For the phase signal, a normalization process is applied to standardize the transition point between the free air region and the attractive region. In the raw data, this transition occurs at arbitrary angles. To facilitate consistent analysis and to match the algorithm across different measurements, the transition point is fixed at  $-90^\circ$ . [62,63,86] These data processing steps are automated through a custom Python script. The complete Python script implementing this methodology is available on the following link.

<https://github.com/ANIQAKHALIQ/AM-AFM-data-analysis>

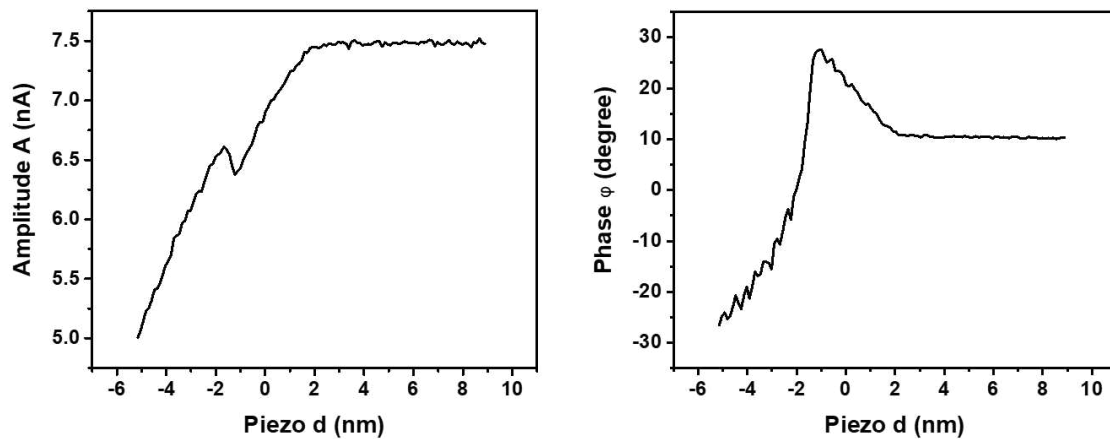


**Figure 3.6** Amplitude/phase versus piezo displacement curves of Anti-IgM proteins physisorbed on gold substrate (Raw data).

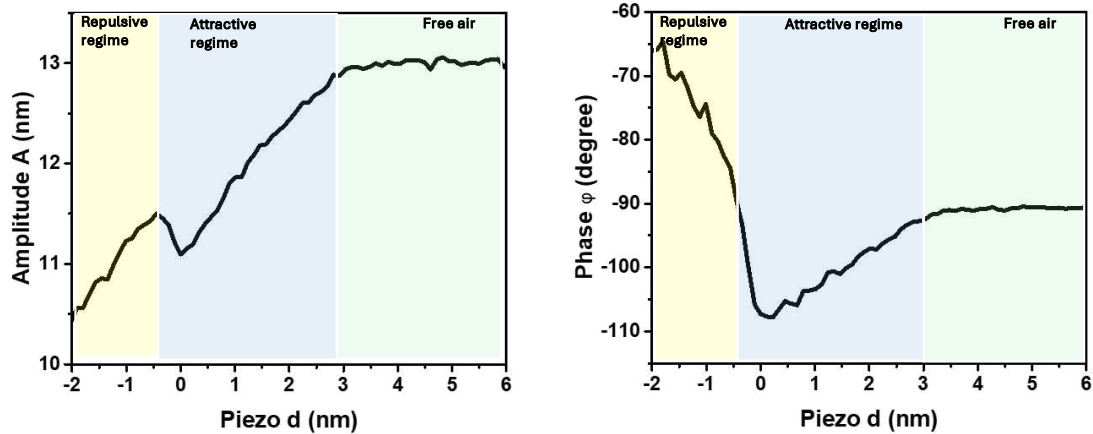


**Figure 3.7** Amplitude/phase versus piezo displacement curves of Anti-IgM proteins physisorbed on gold substrate (processed data). The first area marked in green, the tip is out of contact or free air region and it is approaching the sample. The light blue area corresponds to an decrease in  $\phi < -90^\circ$ , and the tip turns to be in attractive regime. Upon approaching the sample, the tip enters in a third region, named repulsive region (yellow) dominated by an increase of  $\phi$ . The shift of higher values is due to the transition from attractive to repulsive regime. The similar regions are marked for the amplitude profile.

In Figure 3.7, the first area highlighted in green represents the region where the tip remains detached from the sample, positioned in free air, and is moving closer to the surface. As the tip moves closer during its approach, it enters the light blue area, which is associated with a phase shift ( $\phi$ ) of less than  $-90^\circ$ , indicating the tip is now in the attractive regime. As it moves even closer to the sample, the tip transitions into the yellow region, known as the repulsive regime, characterized by an increase in  $\phi$ . This upward shift in phase values signifies the shift from the attractive to the repulsive region.

### 3.2.2 Reconstruction of tip-sample force

The foundation of the force reconstruction lies in the processed Amplitude (A) and Phase ( $\phi$ ) versus piezo displacement (z) curves depicted in Figure 3.7.

The tip-sample potential  $U_{ts}(D)$  is obtained from the amplitude/phase data using the integral equation 3.2. Romberg integration method was used for integration.

$$U_{ts}(D) = 2c_z \int_D^{\infty} K(z) \left[ (z-D) + \sqrt{\frac{A}{16\pi}} \sqrt{z-D} + \frac{A^{3/2}}{\sqrt{2(z-D)}} \right] dz \quad (3.2)$$

Where

$$K(D, A) = \frac{1}{2} \left[ \frac{a_{exc}}{A} \cos \varphi + \frac{f_0^2 - f_d^2}{f_0^2} \right] \quad (3.3)$$

The final term in this integral equation diverges when  $z=D$ . To prevent numerical problems, apply the conversion  $z = D + t^2$  and used the transformed equation.

$$U_{ts}(D) = 4c_z \int_0^{\infty} K(D + t^2) \left[ t^3 + \sqrt{\frac{A}{16\pi}} t^2 + \frac{A^{3/2}}{\sqrt{2}} \right] dt \quad (3.4)$$

To reduce numerical artifacts in subsequent analysis, the calculated potential data undergoes interpolation. This step ensures uniform spacing between data points and facilitates more accurate differentiation. The interpolated tip-sample potential is shown in Figure 3.8a.

The tip-sample force is derived by differentiating the interpolated potential.

$$F_{ts} = -\frac{\partial U_{ts}}{\partial D} \quad (3.5)$$

The resulting force-distance curve typically exhibits a distinct attractive and repulsive regime.

Apply the 4th-order polynomial on the marked regime of the force-distance curve to provide a continuous and analytically differentiable force-distance curve. The algorithm was performed by the c- code.

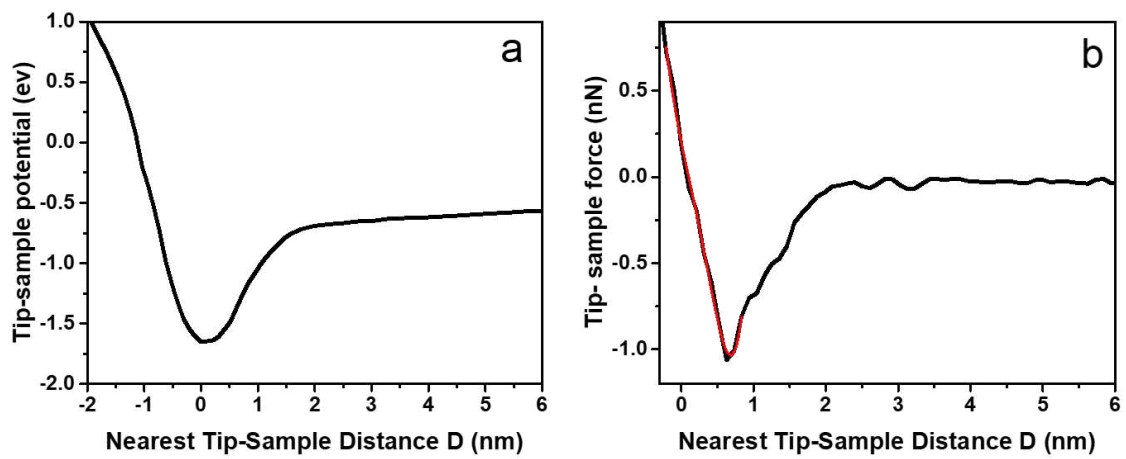


**Figure 3.8** (a) Reconstructed tip-sample potential versus nearest tip-sample distance  $D=d-A$ : the origin of  $D$  has been arbitrarily defined such that  $D=0$  at the minimum potential, from the data points of the amplitude/phase versus distance curves of Anti-IgM proteins on gold substrate is shown in Figure 3.7, (b) Reconstructed tip-sample force versus nearest tip-sample distance  $D$  for anti-IgM proteins.

The same procedure was followed to reconstruct the tip-sample force for all the input curves.

## Part 2 (KPFM)

### 3.3 Materials

All chemicals and reagents were obtained from Sigma-Aldrich and used without any further purification. These included HPLC-grade water, 96% sulfuric acid, 30% (w/w) hydrogen peroxide, anti-human immunoglobulin M (anti-IgM), and human IgM (molecular weight ~950 kDa) and IgG (molecular weight ~150 kDa). Phosphate buffered saline (PBS) solution with pH 7.4 and ionic strength of 162 mM was prepared according to standard protocols. [87] All the immunoglobulins applied consist of polyclonal antibodies.

#### 3.3.1 Patterned bio-functionalized Au surfaces fabrication

The experimental Substrates were cut from As-doped silicon wafers featuring a 300 nm SiO<sub>2</sub> layer formed by thermal growth. The wafer underwent a sequential cleaning process before metal deposition. Initial cleaning involved 10-minute ultrasonic baths in acetone and 2-propanol, followed by nitrogen drying. A 5 nm titanium adhesion layer was deposited, followed by a 50 nm gold layer via electron-beam evaporation at a rate of 0.1 Å/s under a pressure < 10<sup>-6</sup> mTorr. To remove organic residues, the gold electrodes were treated with a freshly prepared piranha solution (a combination of sulfuric acid, water, and hydrogen peroxide), followed by HPLC water rinsing and nitrogen drying. The gold gate bio-functionalization procedure is illustrated in Figure 3.9. In this process, a mask is applied over part of the gold electrode (Step 1), and the exposed area is then submerged in a 0.1 mg/mL anti-IgM PBS solution at 25 °C for 150 minutes (Step 2). This forms a stable, physisorbed layer of anti-IgM on the unmasked region of the gold surface. After mask removal, a distinct Au/anti-IgM interface is left on the substrate (Step 3). The electrode received extensive sequential washing treatments: first in PBS, then in water, followed by air drying. Prior to KPFM measurements, the patterned electrode is prepared by immersing it in HPLC water alongside a gold counter electrode and performing cyclic voltammetry by sweeping the potential in the 0.1 ÷ -0.5 V at a scan rate of 100 mV/s for 20 cycles (Step 4).

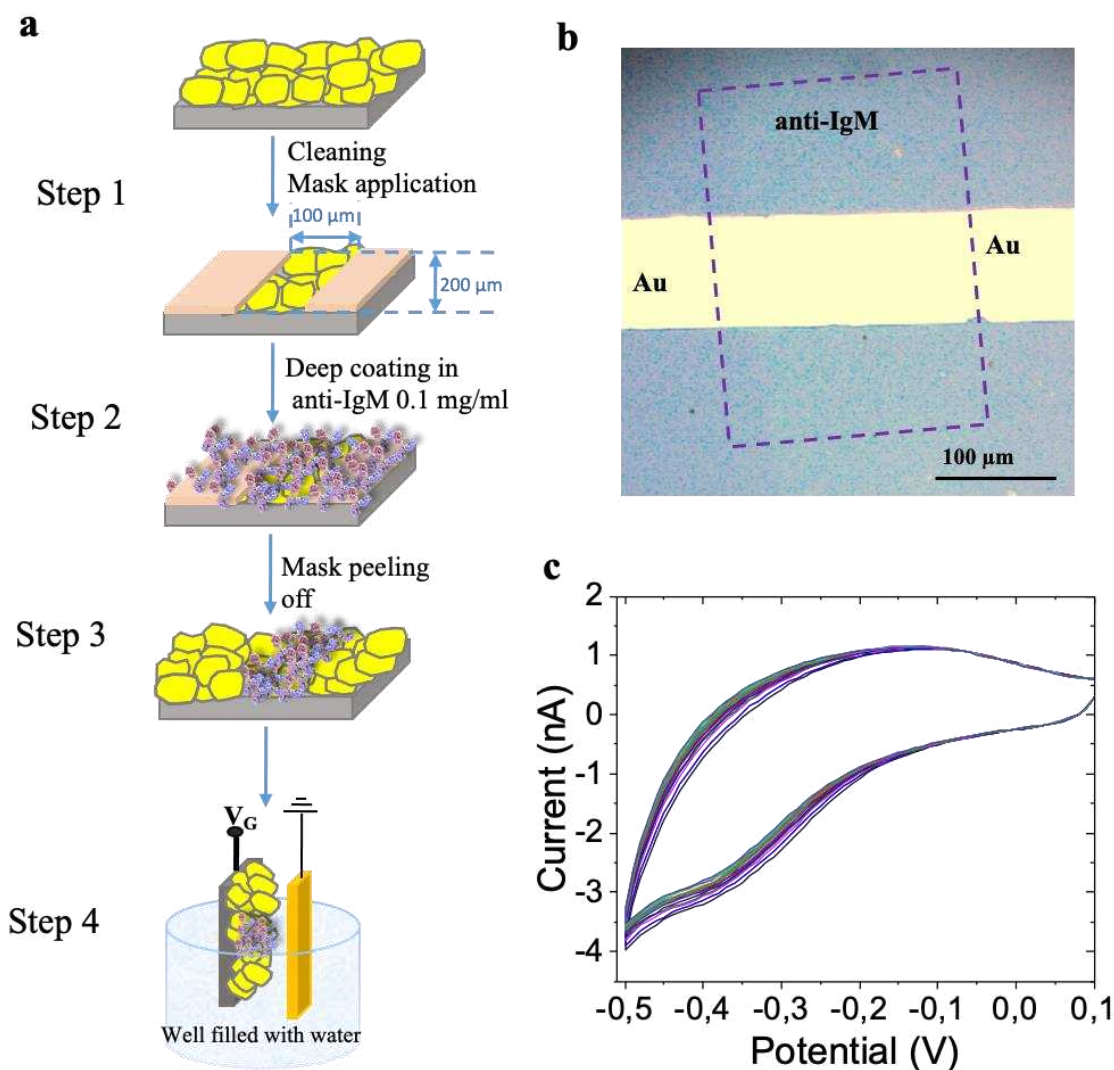


**Figure 3.9 Patterning of Au/anti-IgM surfaces.** (a) Flowchart outlining the protocol for sample preparation. (b) Optical image of the gold substrate patterned with anti-IgM, highlighting the region of the physisorbed protein layer with a blue dashed square. (c) Cyclic voltammograms were recorded from the patterned anti-IgM gold sample by sweeping the potential between the sample and a reference electrode within a water-filled well.

### 3.3.2 KPFM Measurements

#### KPFM Setup and Calibration

KPFM measurements were conducted utilizing an NT-MDT NTEGRA Spectra system (Moscow, Russia) operating in conventional dual-pass semi-contact mode. Pt/Ir-coated cantilevers (Nanosensors, PPP-EFM) with the nominal mechanical resonant frequency of 69

kHz, apex size of 25nm, and spring constant of 2.8 N/m were used. The measurement procedure involved performing two successive passes for each scan line. During the first pass, semi-contact mode was used for morphology and phase image acquisition. The second pass involved surface potential measurement with the tip elevated  $LH=250$  nm above the sample surface to isolate long-range electrostatic forces and minimize topographical artifacts. [88]

KPFM measurements were performed by applying both ac + dc voltages to the probe tip. The AC voltage ( $V_{AC}$ ) induced oscillating electrical forces between the tip and the sample surface, while the DC voltage ( $V_{DC}$ ) counteracted these forces arising from the contact potential difference. A lock-in amplifier was employed to measure the contact potential difference, recording the output signal at each point on the sample surface. This allowed for the mapping of the surface potential across the investigated area.

The technique allowed for the measurement of surface potential changes on a gold substrate before and after the physisorption of a patterned anti-IgM layer. The surface potential difference ( $\Delta V$ ) served as the primary analytical parameter, with the gold portion of the sample acting as an internal reference. Scans of  $90 \times 90 \mu\text{m}^2$  areas across the Au/anti-IgM interface were performed before and after cycling treatment, maintaining consistent scanning locations across ten replicate samples. Sample preparation involved thorough rinsing with deionized water followed by air-drying via spinning at 3000 rpm for 30 seconds. All measurements were performed at room temperature ( $21^\circ\text{C}$ ) in an ambient air environment, with subsequent image processing performed using Image Analysis software.

### **3.4 Single-molecule KPFM measurements protocol**

To perform the assay, the anti-IgM bio-functionalized Au gate was submerged in  $100 \mu\text{L}$  of phosphate-buffered saline (PBS) standard solution for 10 minutes at room temperature ( $20\text{--}22^\circ\text{C}$ ). The initial experiment worked as a negative control and utilized a  $3 \text{ fM}$  solution of non-binding IgG. After the assay, the electrode was rinsed with deionized water. It was then biased against a Au counter electrode in HPLC water and underwent potential cycling between  $0.1 \div -0.5 \text{ V}$  range for 20 cycles. Once air-dried, the sample was analyzed using KPFM. Subsequently, the same gold/anti-IgG electrode was immersed in  $100 \mu\text{L}$  of PBS standard solutions containing IgM at concentrations of  $100 \text{ zM}$ ,  $10 \text{ aM}$ , and  $100 \text{ aM}$ , each for a

duration of 10 minutes. Following each incubation, the electrode was washed thoroughly, subjected to the same potential cycling protocol, air-dried, and then assessed using KPFM.

### 3.5 Electrolyte-gated SiMoT fabrication and single-molecule sensing

The SiMoT device was configured on a silicon substrate doped with a thermally developed SiO<sub>2</sub> layer. Interdigitated source (S) and drain (D) electrodes were defined on the substrate through photolithography, followed by electron-beam evaporation of gold films with a thickness of 50 nm onto a 5 nm titanium adhesion layer. The device has a channel length of 5 μm and a total channel width of 10<sup>4</sup> μm. A filtered P3HT solution (2.6 mg/mL in chlorobenzene) was spin-coated over the S and D electrodes at 2000 rpm for 20 seconds, followed by a 15-second annealing at 90°C. A polydimethylsiloxane well was then affixed around the interdigitated channel area and filled with 300 μL of HPLC-grade deionized water to serve as the gating medium, referred to as the SiMoT measurement well. Current-voltage transfer curves (source-drain current  $I_D$  vs.  $V_G$  at  $V_D = -0.4$  V) were obtained using a semiconductor parameter analyzer paired with a probe station at room temperature. Before sensing measurements, the device stabilized by remaining in deionized water for 12–24 hours post-deposition, in accordance with established protocols. [89] The stabilization of  $I_D$  was further refined by repeatedly measuring the transfer curve using a clean, bare gold gate within the  $V_G$  range of 0.1 ÷ -0.5 until the last three current traces aligned. Typically, 10 to 20 cycles were required. Subsequently, a functionalized gate was incubated in 100 μL of PBS at room temperature and in darkness for 10 minutes. After removal from the PBS solution, the functionalized gate was rinsed thoroughly with HPLC-grade water, placed in the SiMoT measurement well (replacing the previous bare gold gate), and new transfer characteristics were recorded. Following the 10–20 cycles, a stable  $I_0$  baseline was established. The same gate was then incubated in 100 μL of PBS standard solutions containing IgG at a concentration of 1 fM as a negative control, followed by incubations in IgM standard solutions with nominal concentrations of 100 zM and 10 aM. After each incubation in the PBS standard solutions of IgG or IgM, the gate electrode was thoroughly rinsed with HPLC-grade water to remove any unreacted ligands, and additional I-V transfer curves were recorded. All data points represent an average of three replicates, with reproducibility error calculated as one relative standard deviation.

# Chapter 4 Results and Discussion

## Part 1 (AM-AFM)

### 4.1 AFM and AM-AFM Measurements

The AFM measurements of anti-IgM clusters immobilized on a patterned Au substrate at a concentration of 100 ng/ml anti-IgM. The topography was obtained in semi-contact mode. Panel **a** present a large-scale image  $2 \times 2 \text{ } \mu\text{m}^2$  where multiple clusters can be identified are presented in Figure 4.1. The cross symbol indicates the clusters in the regions where force spectroscopy was performed. Panel **b** provides a magnified view of a single protein cluster from the area highlighted in panel **a**. The cluster shows a localized height of 11 nm. The morphology suggests that the anti-IgM molecules may aggregate into larger structures, potentially due to the interaction between individual molecules. The clusters are formed in irregular shapes some clusters are more extended, while others are more compact.

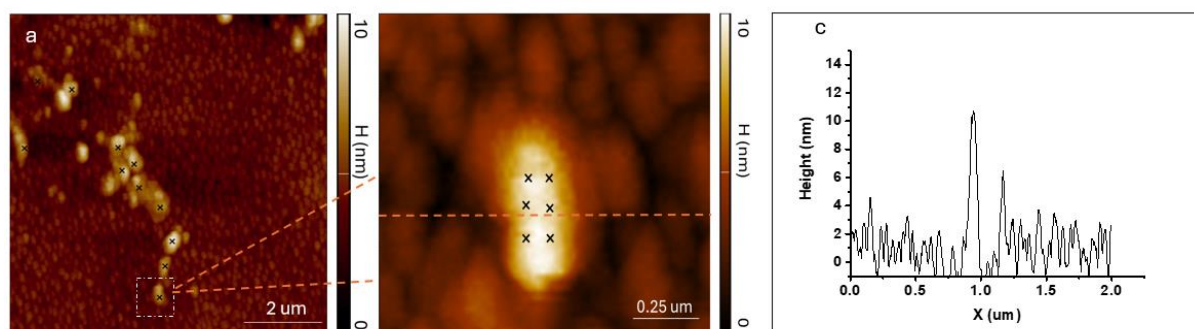


**Figure 4.1** (a) Semi-contact mode topography of a patterned Au/anti-IgM clusters at a concentration of 100 ng/mL anti-IgM, (b) Magnified view of the highlighted region, focusing on a single protein cluster, (c) Cross-section profiles along the lines given in panel b are displayed.

Figure 4.2. shows a topographical AFM image of Anti-IgM film on Au substrate at a concentration of 0.5 mg/ml anti-IgM. The average height of the film was 6nm. Amplitude/phase v/s piezo displacement curves were collected in 4 x 4 arrays as shown in Figure 4.2 (a) on different areas of Au/anti-IgM sample in quintuplicate to characterize the protein film.

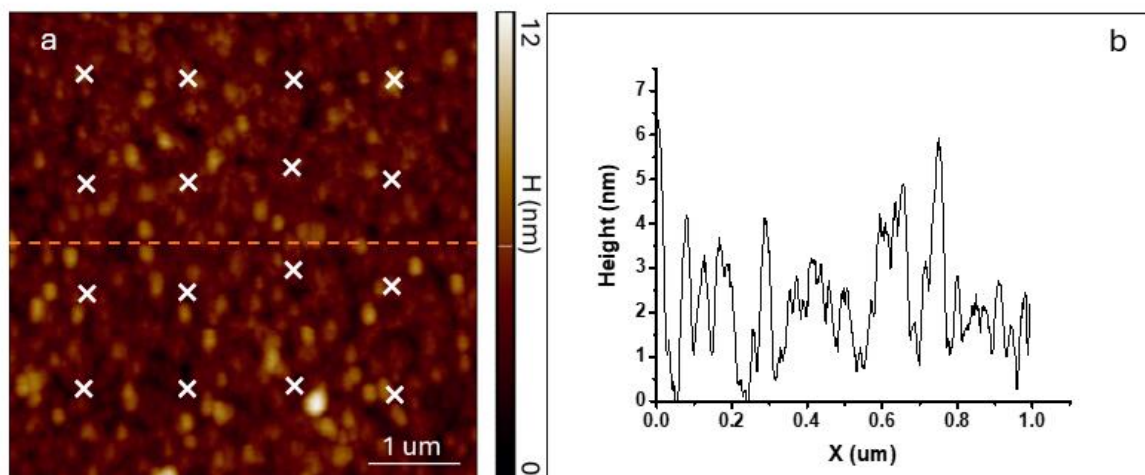


**Figure 4.2** (a) Semi-contact mode topography of a patterned Au/anti-IgM film at concentration of 0.5 mg/mL anti-IgM, (b) Cross-section profiles along the lines given in panel a are displayed.

Dynamic amplitude/phase curves were produced by tracking the "approach and retract" motion of the cantilever from the sample surface during the operation of the AFM in amplitude modulation mode. Two parameters—amplitude ( $A$ ) and phase ( $\phi$ )—were measured as functions of piezo displacement, which were then converted into the distance between the tip and sample. Using the force reconstruction algorithm, the amplitude/phase versus distance (APD) curves were transformed into force versus distance profiles. [63] From these force profiles, mechanical parameters such as Young's modulus, stiffness, and adhesion force were subsequently obtained.

In AM-AFM, the excitation frequency is maintained at a constant value, allowing the amplitude/phase lag of the oscillation to serve as dual channels for investigating both conservative (elastic) and dissipative (inelastic) tip-surface interactions. The amplitude-distance curves exhibit distinct regions that reflect the nature of these interactions. At substantial tip-surface separations, the oscillation amplitude remains largely unaffected by distance variations. However, as the average tip-surface separation decreases, a regime emerges where the amplitude starts to reduce. This reduction can be ascribed to the onset of interactions between the tip and the surface, which may encompass a range of forces including electrostatic, hydrophobic, van der Waals, and chemical adhesion, as well as both short/long-range interactions.

A key feature in the amplitude curves is the occurrence of a local maximum, which may be ascribed to the interplay between attractive and repulsive interaction regions. This maximum marks the transition point between these opposing forces, providing valuable insights into the intricate nanoscale interactions at the protein-tip interface.

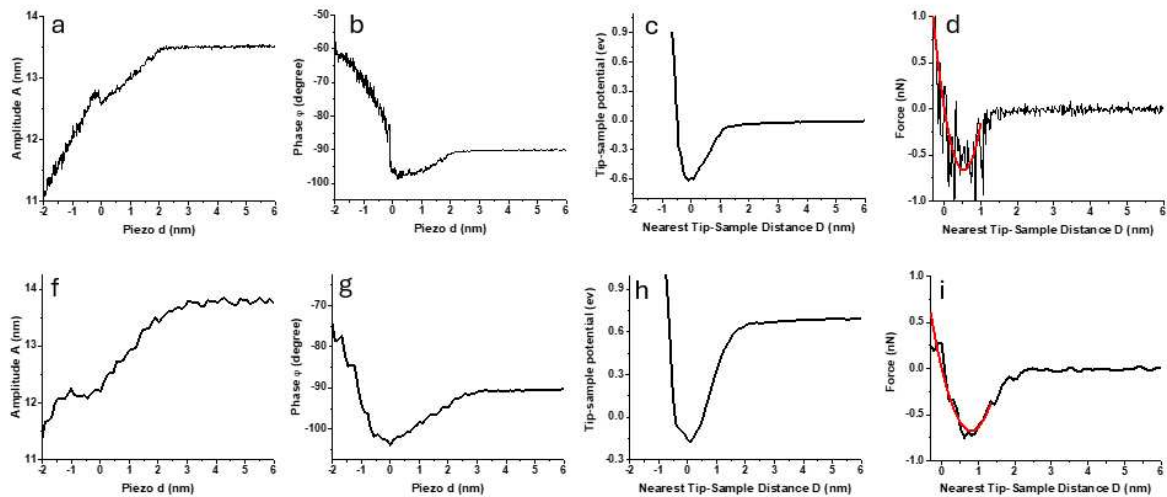


**Figure 4.3** The representative outcomes of amplitude/phase versus distance curves on protein film (a,b) reconstructed tip-sample potential (c), tip-sample interaction force between AFM tip and anti-IgM protein film (d). The representative outcomes of amplitude/phase versus distance curves on protein clusters (f,g) reconstructed tip-sample potential (h), tip-sample interaction force between AFM tip and anti-IgM protein clusters (i).

The transition for the amplitude curve in the Anti-IgM cluster is smoother than Anti-IgM film. Which can be linked to the lower values of repulsive forces relative to the film. The phase curve depicts a similar trend like the Amplitude profile. As the tip-sample separation decreased, attractive interactions arise, causing the phase to shift from -90 to -100, this shift indicates the presence of the attractive regime. The transition of the phase curve is smoother for the protein cluster than the protein film, which is a confirmation of the hypothesis that protein clusters have lower interactive forces than the protein film. Furthermore, within this regime, the AFM probe makes contact with the surface, and as a result of the Pauli exclusion principle, a repulsive force arises between the atoms of the AFM tip and the molecules or atoms of the proteins. The relationship between phase profiles and amplitude curves indicates a shift between two distinct regimes, the transition occurs from an initial regime, where the amplitude is decreased by the action of long-range attractive forces (the contact time is equal to zero) to

a subsequent regime, where the amplitude reduction is primarily governed by short-range repulsive forces (accompanied by a very short contact time).

The reconstructed forces of representative amplitude/phase profiles Figure 4.3 (d,i), from the reconstructed forces, It is observed that the contact between tip and protein molecules initiates at a greater distance value for protein film than the protein clusters. This is due to the large electrostatics force for the protein cluster with respect to protein film. In Figure 4.3 (d,i) The maximum attractive force value for protein cluster and protein film is nearly equal. The difference in the mean interaction forces for the anti-IgM clusters and film can be due to the difference in contact areas between the tip and the protein layer and clusters when measured at different times and different positions, the distribution density of protein molecules on the substrate, along with the thermal fluctuation of AFM. The increased adhesion can be attributed to the large surface area of clusters interacting with the substrate, enhancing molecular interaction such as hydrogen bonding or van der Waals forces. Clusters expose more binding sites due to their aggregated structure, leading to stronger adhesion, For the film due to uniform and flat contact of the film with the substrate, fewer active binding sites are available for interaction. Due to compact conformation, film reduces the effective surface area and strength of adhesion. [32-34]

Additionally, the force profiles can be distinctly linked to the amplitude and phase behavior, where, in the initial region of interaction between tip and surface, both the average force and its slope are negative ( indicating a noncontact regime). Furthermore, in the transition between non-contacts to intermittent contact regions, the average force is negative whereas its slope reflects a positive value. Consequently, upon indenting the surface, which is indicative of a fully repulsive region, both the average force and its slope would be positive.

## 4.2 Energy Dissipation in AM-AFM

The amount of dissipated energy is determined using the subsequent mathematical expression.

$$\Delta E = \left( \frac{1}{Q_0} \frac{f_d}{f_0} + \frac{a_{exc}}{A} \sin \phi \right) \pi c_z A^2 \quad (4.1)$$

where  $f_d$ ,  $f_o$ ,  $A$  and  $\phi$  are driving frequency, resonance frequency, oscillation amplitude and phase respectively. [31]

During AFM assessments, energy loss manifests at both atomic and molecular scales, primarily stemming from multiple fundamental atomic interactions that unfold as the probe tip with the specimen. One such process is surface energy hysteresis, where energy is lost due to the change in surface energy during the approach and retraction of the tip. Viscoelasticity also contributes, as the material deforms and resists returning to its original shape, causing energy loss. Additionally, intramolecular charge transfer occurs when charges move within the molecules as the tip interacts with the sample, resulting in electrical dissipation. Long-range dissipative interfacial interactions between the tip and sample at larger distances also play a role, as do mirror charges generated at large separations between the tip and sample, which further contribute to the overall energy dissipation. [90] Figure 4.4 (a,b) illustrates the dissipated energy trends for both protein clusters and films, plotted against the decreasing distance as the probe tip progresses towards the surface.

The measured energy dissipation between the AFM probe and globular proteins falls within a range of approximately 0.2 to 5 eV. Notably, the energy loss profile for protein clusters exhibits an earlier onset of increase compared to protein films, a phenomenon that can be attributed to the influence of long-range interfacial dissipation mechanisms and the dynamic response of image charges driven by electrostatic interactions. These long-range forces can cause the AFM tip to experience energy loss at greater distances from the sample surface which is consistent, energy dissipation begins earlier in protein clusters than in stiffer protein films.

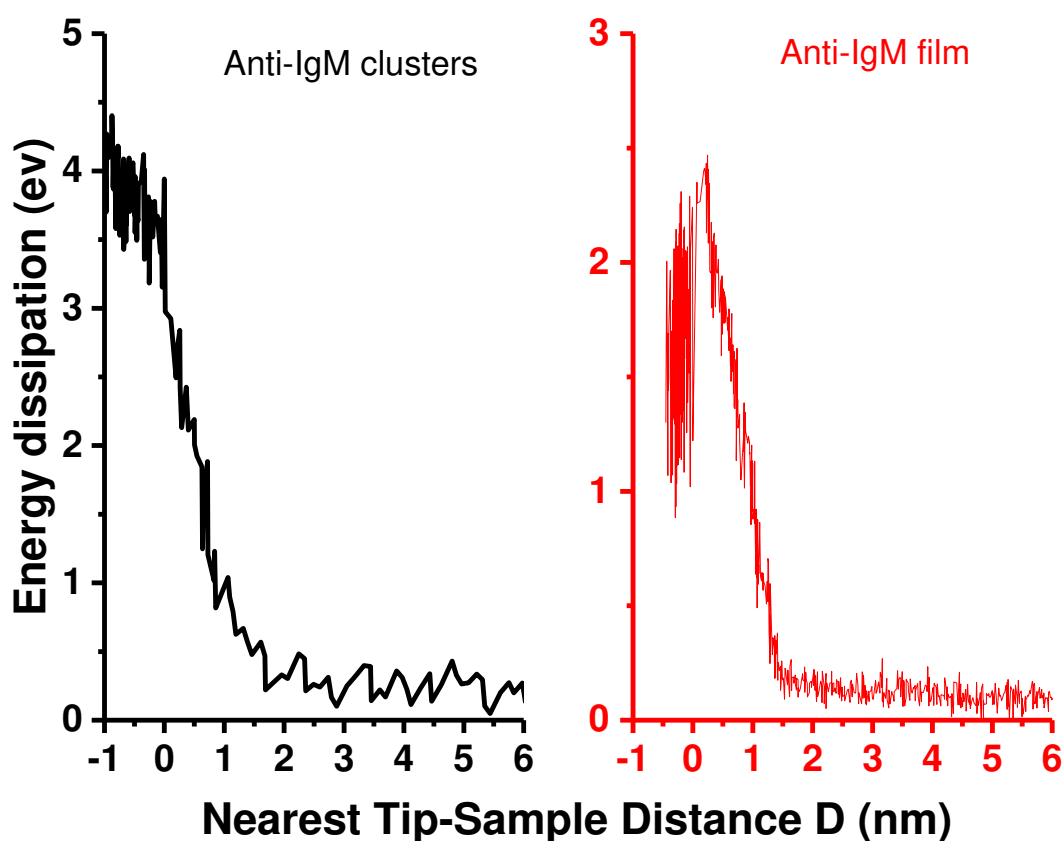


**Figure 4.4** Typical Energy Dissipation Profiles of Anti-IgM Structures. The representative results of Energy loss characteristics are presented for anti-IgM clusters and anti-IgM film, respectively, as a function of the minimum distance between the AFM tip and the sample surface.

A notable increase in energy dissipation is observed for protein clusters as the interaction regime shifts from attractive to repulsive. This indicates that the cluster structure deforms more in the repulsive regime, causing an increase in energy dissipation due to friction and deformation. In the case of protein films, energy dissipation culminates at a maximum value within the attractive regime, subsequently plummeting as the AFM probe transitions into the repulsive regime, characterized by enhanced stability in tip-sample interaction and negligible dissipation. The relatively soft protein clusters correspond to a high level of energy dissipation, whereas the stiffer protein film dissipates less energy by tip-sample interaction. Upon probing a sample with relatively lower stiffness, the protein cluster exhibits elastic strain, leading to an expansion of the effective contact zone. Consequently, this increased interface results in elevated energy dissipation due to enhanced frictional interactions between the probing tip and the sample surface. [90]

### 4.3 Mechanical properties

The mechanical properties of protein clusters and films was assessed, yielding key parameters: Young's modulus ( $E$ , MPa), stiffness ( $k$ , N/m), and adhesive force ( $F_{ad}$ , nN), all deduced from reconstructed force data and AM-AFM measurements. Figure 4.5 displays the computed mechanical characteristics of the protein specimens. Notably, the Young's modulus was determined by utilizing the Johnson-Kendall-Roberts (JKR) theoretical framework, based on the subsequent mathematical formulation.

$$E = \frac{3}{4} (1 - \nu)^2 \left\{ \frac{1 + 16^{1/3}}{3} \right\}^{3/2} \frac{F_{min}}{(r(\text{Sep}_{zero} - \text{Sep}_{min})^3)^{1/2}} \quad (4.2)$$

Here,  $\nu$  represents the material's Poisson's ratio;  $F_{min}$  denotes the minimum detected force, occurring at  $z = \text{Sep}_{min}$ ; and  $\text{Sep}_{zero}$  signifies the retraction distance where the force effectively drops to zero. [47]

The Young's modulus ( $E$ , MPa) for all 11 protein clusters falls in the range of 0.03 GPa to 0.41 GPa with an average value of  $0.19 \pm 0.10$  GPa. Additionally, it is noteworthy that, from an experimental point, there is a lack of reference data specifically about protein clusters deposited on solid state gold substrate in an ambient (air) environment. The Young's modulus for protein film is in the range of 0.35 GPa to 0.96 GPa with an average value of  $0.68 \pm 0.11$  GPa. It is in good agreement with the findings for globular protein films. [18] The minimum values of Young's modulus for the protein clusters indicate that they are less dense and have a more disordered arrangement compared to protein films. This lower packing density results in weaker intermolecular interactions, making the clusters more compliant and less rigid. The higher Young's modulus of the protein films suggests a more compact, uniformly structured material with denser packing and greater resistance to deformation. [91–93]

Stiffness, a pivotal mechanical property, is quantitatively determined by analyzing the slope within the linear or elastic segment of the force versus distance plot. It reflects the resistance of the protein film or clusters under the applied force. The stiffness of antibodies affects their ability to bind to antigens effectively. The stiffness  $k$  ( $\text{Nm}^{-1}$ ) for all 11 protein clusters falls in the range of 1.2 to 4.5  $\text{Nm}^{-1}$  with a mean value of  $2.47 \pm 0.47 \text{ Nm}^{-1}$ . For the protein film, it is 1.34 to 6.1  $\text{Nm}^{-1}$  yielding a mean of  $3.60 \pm 0.85 \text{ Nm}^{-1}$ . The larger mean

stiffness of the protein film is indeed likely due to stronger non-covalent interactions, leading to higher repulsive forces when the tip is in contact with the protein surface, non-covalent interactions are relatively weak and reversible, which is important for the dynamic nature of antigen-antibody interactions. Higher stiffness values in protein films indicate greater resistance to deformation under applied forces. This suggests that protein films are more structurally robust and can maintain their integrity when subjected to external stresses.

The adhesive force is characterized by the pull-off force value, readily extractable from the force versus distance plot. Notably, the measured adhesive force  $F_{ad}$  (nN) exhibited pronounced variations when comparing protein clusters to protein films. For protein clusters, it is ranging from 0.70 to 2.3 nN with an average of  $1.49 \pm 0.41$  nN. The protein film exhibited lower values of 0.56 to 1.84 nN with a mean value of  $1.07 \pm 0.29$  nN. The mean interaction forces between anti-IgM clusters and film differ due to variations in contact area, protein density distribution, and thermal fluctuations. The larger surface area of protein clusters facilitates more molecular interactions with the substrate, also the distribution of proteins within clusters creates a more heterogeneous environment, allowing for multiple binding sites and enhanced molecular interaction with surfaces. Additionally, in clusters thermal fluctuations may enhance the mobility of proteins, allowing them to engage more effectively with the gold substrate. The uniform and compact structure of protein film restricts the number of available binding sites, thereby reducing overall adhesion strength. [94]

These results collectively demonstrate the significant influence of protein organization (clusters vs. films) on their nanomechanical properties. The differences observed in Young's modulus, stiffness, and adhesion force between clusters and films highlight the complex interplay between molecular structure and mechanical behavior in biomolecular systems. Further investigation into the relationship between these nanomechanical properties and the functional characteristics of anti-IgM proteins could provide valuable insights into their role in immune responses and potential applications in biomedical engineering. Additionally, these findings underscore the importance of considering protein organization when designing or analyzing protein-based materials for various applications.

The large distribution range of mechanical properties including Young's modulus, stiffness, and adhesion force) observed in both the protein clusters and protein films physisorbed on a gold substrate can be attributed to several factors, particularly the interaction

between the proteins and the substrate surface characteristics. The irregularities in the gold surface led to non-uniform adsorption of the protein molecules, resulting in variations in their packing density, orientation, and contact area with the substrate. The inherent non-uniformity of the substrate gives rise to a broad spectrum of mechanical properties since varying areas of the gold surface exert distinct influences on the conformation of deposited proteins. The gold substrate's roughness introduces heterogeneity in protein adsorption. Proteins adsorbed onto areas with high surface roughness may experience more localized deformation and increased interaction forces. This variability results in a wide range of values for stiffness and Young's modulus. [39-41]

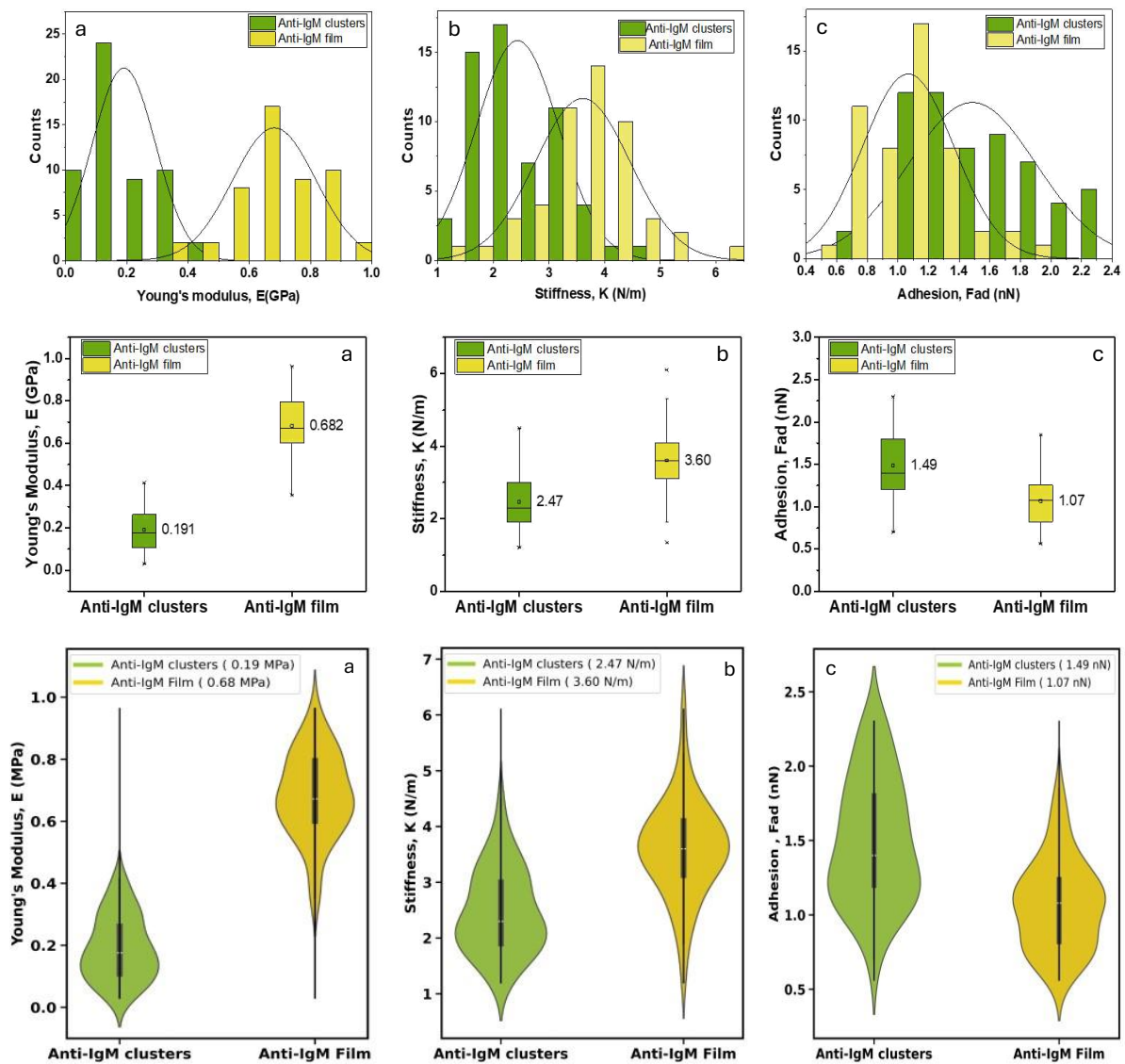


**Figure 4.5** Mechanical characterization of Anti-IgM proteins (clusters vs. film). (a) Young's modulus distribution and the statistical comparison of protein clusters and film, (b) Stiffness

distribution and the statistical comparison of protein clusters and film, (c) Adhesion force distribution and the statistical comparison of protein clusters and film, respectively.

**Table 4.1 Mechanical properties of anti-IgM clusters and anti-IgM film.** The mean values presented include Young's modulus ( $E$ ), stiffness ( $K$ ), and adhesion force ( $F_{ad}$ ) for each sample type.

<b>Sample</b>	<b>Young's modulus, E (GPa)</b>	<b>Stiffness, K (N/m)</b>	<b>Adhesion, <math>F_{ad}</math> (nN)</b>
Anti-IgM clusters	$0.19 \pm 0.10$	$2.47 \pm 0.47$	$1.49 \pm 0.41$
Anti-IgM film	$0.68 \pm 0.11$	$3.60 \pm 0.08$	$1.07 \pm 0.29$

## Part 2 (KPFM)

### 4.4 AFM Measurements

The topography of the Au/anti-IgM surface was analyzed using atomic force microscopy (AFM) with an NTEGRA Spectra instrument (NT-MDT, Moscow, Russia) worked in semi-contact mode. Measurements were conducted in ambient air environment. AFM analysis of a representative  $95 \times 60 \mu\text{m}^2$  area (cross-section profile in panel a) revealed a distinct step between the leftmost gold side substrate and the anti-IgM functionalized region rightmost one. The height profile showed a tightly packed layer of capturing antibodies with an approximate thickness of 3 nm. Higher resolution scans of  $5 \times 5 \mu\text{m}^2$  regions were performed to examine the surface morphology in greater detail Figure 4.6 (c,d). The gold substrate showed a typical grain structure, with an average grain size of  $\sim 20$  nm, characteristic of Au thin films deposited through electron beam evaporation. In contrast, the anti-IgM functionalized area displayed a notably different texture. Quantitative roughness analysis was conducted on multiple  $1 \times 1 \mu\text{m}^2$  on five different areas. The results demonstrated a significant increase in surface roughness following bio-functionalization. The average roughness values were  $0.83 \pm 0.04$  nm for the bare gold surface and  $1.18 \pm 0.03$  nm for the anti-IgM modified region.

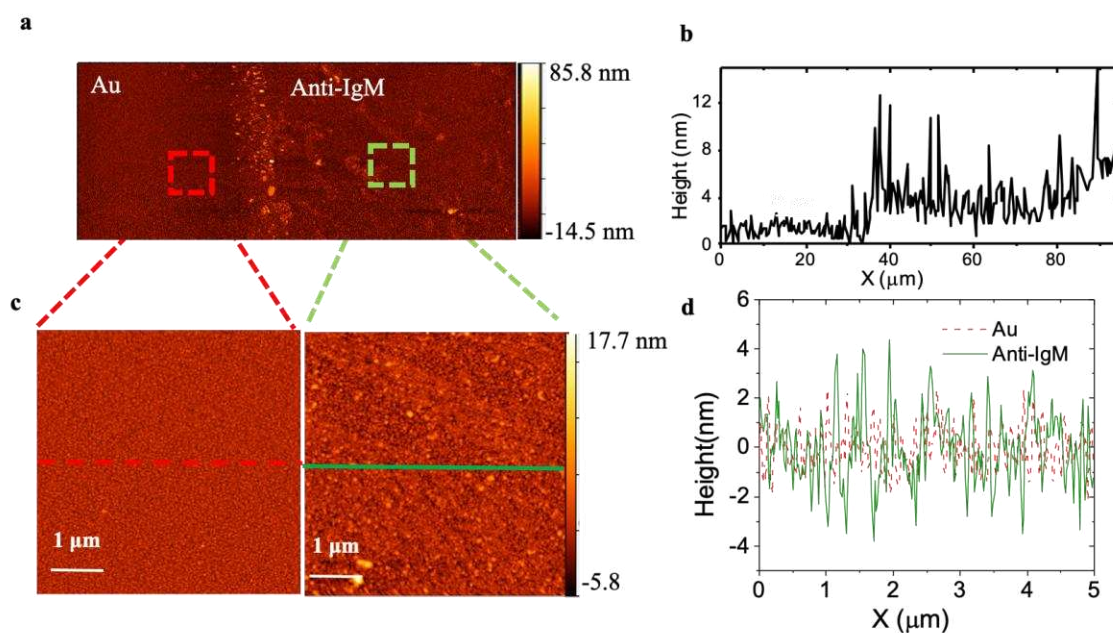


**Figure 4.6** AFM analysis of the Au/anti-IgM patterned surface. (a) Representative topography image obtained in semi-contact mode. (b) Cross-sectional profile along the line

marked in (a). (c) High-resolution images showcasing the morphologies of the gold (left) and anti-IgM (right) regions. (d) Comparative cross-sectional profiles from (c), demonstrating increased roughness in the bio-functionalized area (red) compared to the gold region (green).

#### 4.5 Electrolyte-gated SiMoT sensor I-V transfer curves

The transfer characteristics curves  $I_D - V_G$  at a constant  $V_{DS} = -0.4$  V are presented in Figure 4.7a. The transfer curves are relevant to the stabilized current recorded for each step following the transistor stabilization, achieved by cycling the device within the  $V_G$  range [0.1 V, -0.5 V] in an aqueous medium, for consecutive 20 measurements. The baseline current, represented by the black curve, was obtained from a gold gate functionalized with physisorbed anti-IgM and incubated in PBS for 10 minutes. The red curve shows the current recorded on the same SiMoT device with a matching anti-IgM gate after it was incubated in a PBS standard solution containing 3 fM IgG, used as a negative control. The blue and green curves depict the current measurements following sequential incubation of the anti-IgM gate in PBS standard solutions of IgM at concentrations of 100 zM and 10 aM, respectively. Remarkably, the inset of Figure 4.7b demonstrates that the gate leakage current ( $I_G$ ) consistently remains approximately three orders of magnitude below  $I_D$ . A small faradaic activity is evident in the  $I_G$  curve of the anti-IgM gate, attributable to subtle oxidative processes (minimized within the examined range) that exhibit no correlation with the sensing mechanism.

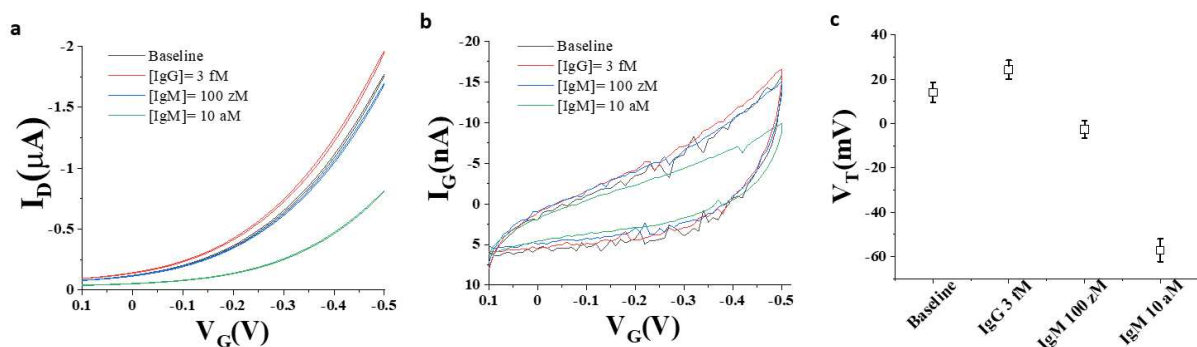


**Figure 4.7** (a) The transfer characteristics curves  $I_D - V_G$ , at a fixed  $V_D = -0.4$  V, and  $V_G$  ranging from 0.1V to -0.5 V. (b)  $I_G - V_G$  gate leakage current, registered with  $V_G$  ranging from 0.1 V to -0.5V, at a fixed  $V_D$  of -0.4 V. (c) Threshold voltage measured from the SiMoT device with an anti-IgM biofunctionalized gate. The device underwent sequential incubation, first in bare PBS to establish a baseline, followed by a PBS standard solution containing 3 fM IgG as a negative control, and finally in PBS standard solutions with IgM concentrations of 100 zM and 10 aM for the sensing experiment.

According to Macchia et al., the  $I_D$  current passing through the transistor channel in the saturation regime is expressed as follows: [95]

$$I_{DS} = \frac{W\mu_{FET}C_i}{2L}(V_G - V_T)^2 \quad \text{for } |V_{DS}| > |V_{DS}^{sat}| \quad (4.3)$$

where  $W$  is the channel width,  $L$  is the channel length,  $C_i$  is the capacitance per unit area of the gating system,  $V_T$  signifies the EGOFET threshold voltage and  $\mu_{FET}$  is the field-effect mobility. From the equation,  $\sqrt{I_{DS}}$  exhibits a linear relationship with  $(V_G - V_T)$ , with  $V_T$  corresponding to the x-intercept to the  $V_G$  axis, and the linear segment slope of the curve is proportional to  $(C_i \cdot \mu_{FET})$ . A change in the threshold voltage ( $V_T$ ) upon exposure to the target analyte indicates a shift in the gate electrochemical potential or the work function related to the biorecognition events. The shift is observable at an IgM concentration as low as 100 zM, which corresponds to  $6 \pm 2$  IgM molecules in the  $100 \mu\text{L}$  sampled volume, as illustrated in Figure 4.7c. The anti-IgM functionalized gate exhibits a threshold voltage of  $(14 \pm 4)$  mV. Notably, the incubation of the biofunctionalized gate in an IgG solution results in a negligible shift of the threshold voltage towards more positive values, ( $V_T = 24 \pm 5$  mV). In contrast, when the biofunctionalized gate is exposed to IgM, a threshold voltage shift toward negative potentials is induced. Specifically,  $V_T$  is measured as  $(-3 \pm 3)$  mV following exposure to 100 zM IgM, while a  $V_T$  of  $(-57 \pm 5)$  mV is recorded after exposure to 10 aM IgM.

#### 4.6 Kelvin probe force microscopy (KPFM) measurements

KPFM employs a two-pass atomic force microscopy (AFM) technique. During each line scan, the initial pass captures the morphology in semi-contact mode, with the tip oscillating at the cantilever's resonance frequency  $\omega_0 \approx 2\pi \times 70$  kHz. In the second pass, mechanical oscillation is suspended, and the tip is elevated at a set lift height  $D$  above the surface while an  $ac + dc$  voltage  $U_{dc} + U_{ac} \sin(\omega_0 t)$  is applied to the probe. The probe oscillation amplitude is continuously nullified via a feedback loop by modulating the  $dc$  component of the bias voltage  $U_{dc}(x, y)$ . This  $dc$  component corresponds to the local contact potential difference (CPD) between the sample surface and the tip. [96] The CPD images are equivalent to the sample work function ( $W$ ) or surface potential ( $\Phi_S$ ) images, differing only by a constant offset equal to the tip's work function. Figure 4.8a illustrates the KPFM measurement schematic. During the characterization process morphology, phase, and surface potential images are captured. All images are processed using NT-MDT Image Analysis software.

Figure 4.8, presents the morphology, phase, and corresponding surface potential image of a representative  $95 \times 95 \mu\text{m}^2$  electrode region spanning the Au/anti-IgM interfacial area. KPFM analysis reveals that the anti-IgM capturing layer exhibits a higher surface potential compared to bare Au.

Many biological molecules, by their nature, exist in a charged state under physiological conditions. As illustrated in Figure. 4.8b, the anti-IgM molecule exhibits a "Y"-shaped structure comprising of two identical fragment antigen-binding ( $F_{ab}$ ) arms and a single fragment crystallizable ( $F_c$ ) region, composed of two heavy chains. [97] The  $F_{ab}$  fragments comprise different regions capable of specific antigen binding, while the  $F_c$  fragment is the tail region that interacts with cell surface receptors. The antibody molecule can be represented as an electric dipole, where the dipole moment vector extends from the negatively charged  $F_c$  region toward the positively charged  $F_{ab}$  regions. [98] After physisorption, a layer of randomly oriented dipoles forms on the vacuum side, giving rise to the surface electrostatic potential.

KPFM measurements revealed the formation of a tightly packed bioreceptor layer through physisorption, displaying a higher surface potential compared to the gold substrate, as shown by the brighter regions in the potential profile. This observation is attributed to the linear low resolution employed in KPFM imaging of hundreds of micro-square areas.

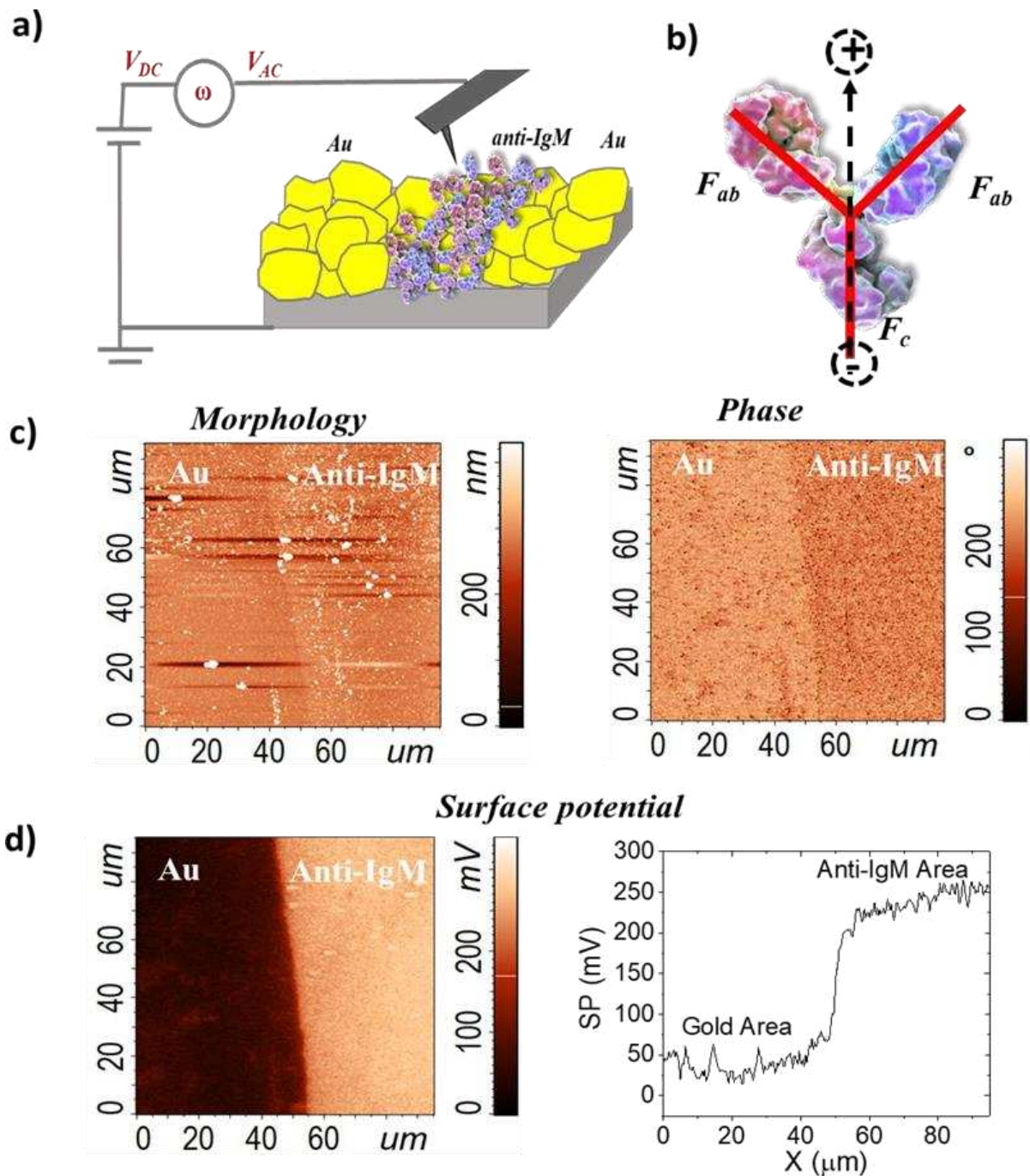


**Figure 4.8** (a) Illustration of dual-pass Kelvin probe microscopy measurement setup. (b) Basic structure of the antibody molecule showing two  $F_{ab}$  segments and one  $F_c$  portion, with the dipole moment direction pointing from  $F_c$  to  $F_{ab}$  regions. (c) Topography, phase contrast, and surface potential maps were recorded concurrently during measurement. (d) The mean surface potential distribution is shown in the inset.

The accurate interpretation of KPFM measurements requires a reliable reference point for calibration during scanning. Either a designated area of the sample or the scanning tip can

function as this reference standard, which is crucial for obtaining meaningful surface potential data across the analyzed surface.

KPFM enables high-resolution mapping of surface potential variations, offering insights into local electronic properties. However, data interpretation must consider the relative nature of potential values and the importance of proper calibration for meaningful quantitative analysis. [99] KPFM data quality depends on proper reference selection, as measurements are affected by multiple factors including tip-sample separation, applied voltages, humidity levels, and surface contamination. Even inert metal gold surfaces, despite their chemical stability, can show significant non-monotonic work function variations up to 0.5 V when exposed to air, representing roughly 10% change in measured values. [100]

To improve the accuracy and reliability of KPFM surface potential measurements while reducing external influences, we developed a three-part experimental strategy: i) Creating patterned substrates with antibody-modified regions ( $100\text{-}200\ \mu\text{m}^2$ ) adjacent to unmodified gold surfaces with clear boundaries, ii) Optimizing measurement conditions and parameters, iii) Capturing surface potential data from both unmodified gold and anti-IgM functionalized gold (Au/anti-IgM) areas simultaneously within each KPFM scan.

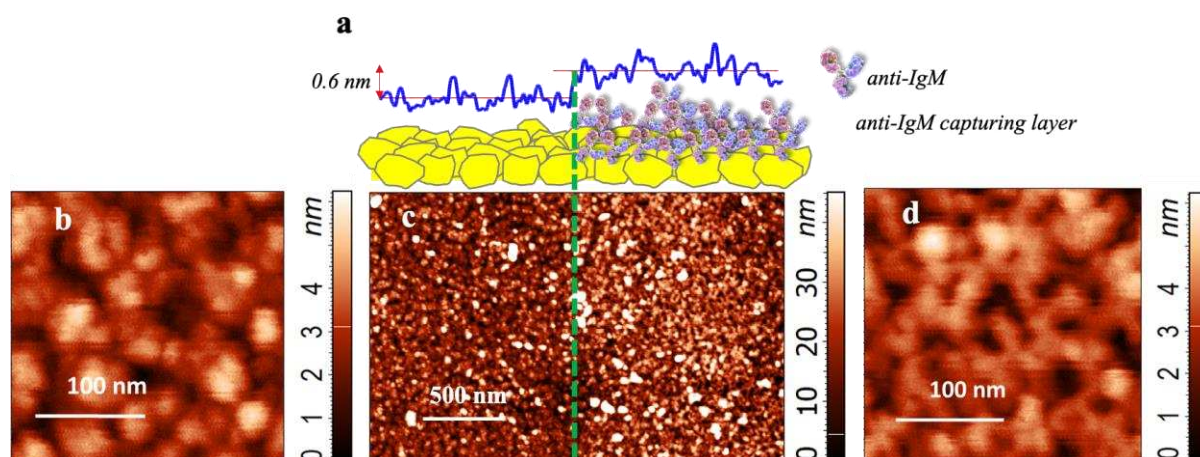


**Figure 4.9** AFM analysis of the patterned Au/anti-IgM electrode surface. (a) Cross-sectional representation showing the boundary between unmodified and anti-IgM functionalized gold regions, including height profile measurements across the interface. (b) Topographic AFM scans of the bare gold electrode. (c) Region showing transition between unmodified gold (left side) and antibody-modified gold (right side). (d) Surface scan of the anti-IgM modified gold region. Green dotted lines in (a) and (c) indicate the interface boundary.

Figure 4.9 represents the AFM topographic scans showing the boundary region between bare gold (left side) and anti-IgM functionalized gold (right side) of the electrode surface, as illustrated earlier in Figure 4.6. The illustration of the Au/anti-IgM interface (Figure 4.9a) shows the AFM profile measured across the clearly defined boundary, indicating an average height increase of 0.6 nm at the edge of the anti-IgM capturing layer. This height difference is consistent with a layer of antibodies predominantly lying flat on the electrode surface. [101] Figure 4.9c shows an AFM scan of the interface area, emphasizing the morphological differences between the bare and functionalized regions. The anti-IgM layer surface (Figure 4.9d) exhibits a network of chains or interconnected segments, with a rms roughness around 1.3 nm. This surface morphology aligns with a dense, physisorbed monolayer of anti-IgM molecules. The observed surface features suggest a coverage density of approximately  $10^{12}$  anti-IgM/cm<sup>2</sup>, which is equivalent to about  $10^9$  anti-IgM molecules on a  $10^5$  μm<sup>2</sup> area. [87,102]

KPFM images (middle panels) and corresponding histograms (right panels) of an Au/anti-IgM patterned electrode, examined before and after several individual binding events are shown in Figure 4.10. The left panels of Figure 4.10 (a,d,g,l) provide schematic representations of each experimental setup. The top row displays results from the untreated Au/anti-IgM sample. Subsequent rows illustrate the Au/anti-IgM sample response to non-binding (IgGs) and binding (IgMs). The experiments utilize phosphate buffer saline (PBS, pH = 7.4, ionic strength = 162 mM) solutions of the target ligands to simulate physiological conditions. Figures 4.10b and 4.10c depict the KPFM image and average values across the pristine Au/anti-IgM interface, measuring  $176 \pm 20$  mV. This measurement serves as the baseline differential between bare gold and unexposed anti-IgM. Figures 4.10e and 4.10f illustrate the KPFM image and values ( $167 \pm 20$  mV) obtained after incubating the Au/anti-IgM sample for 10 minutes in 100 ml of a 3 femtomolar (fM) IgG solution. These results, comparable to the baseline within error bars, act as a negative control due to IgGs non-binding nature with anti-IgM. Subsequently, the same Au/anti-IgM electrode undergoes incubation in binding IgM solutions. Notably, following exposure to 100 zM and 10 aM IgM PBS solutions, the KPFM scans (Figures 4.10h and 4.10m) exhibit significant alterations. The  $\Delta\phi$  values decrease to  $128 \pm 20$  mV for the 100 zM concentration and  $116 \pm 20$  mV for the 10 aM concentration, representing reductions of  $\Delta\phi$  (100 zM, Figure 4.10i) and  $\Delta\phi$  (10 aM, Figure 4.10n) relative to the baseline, respectively.

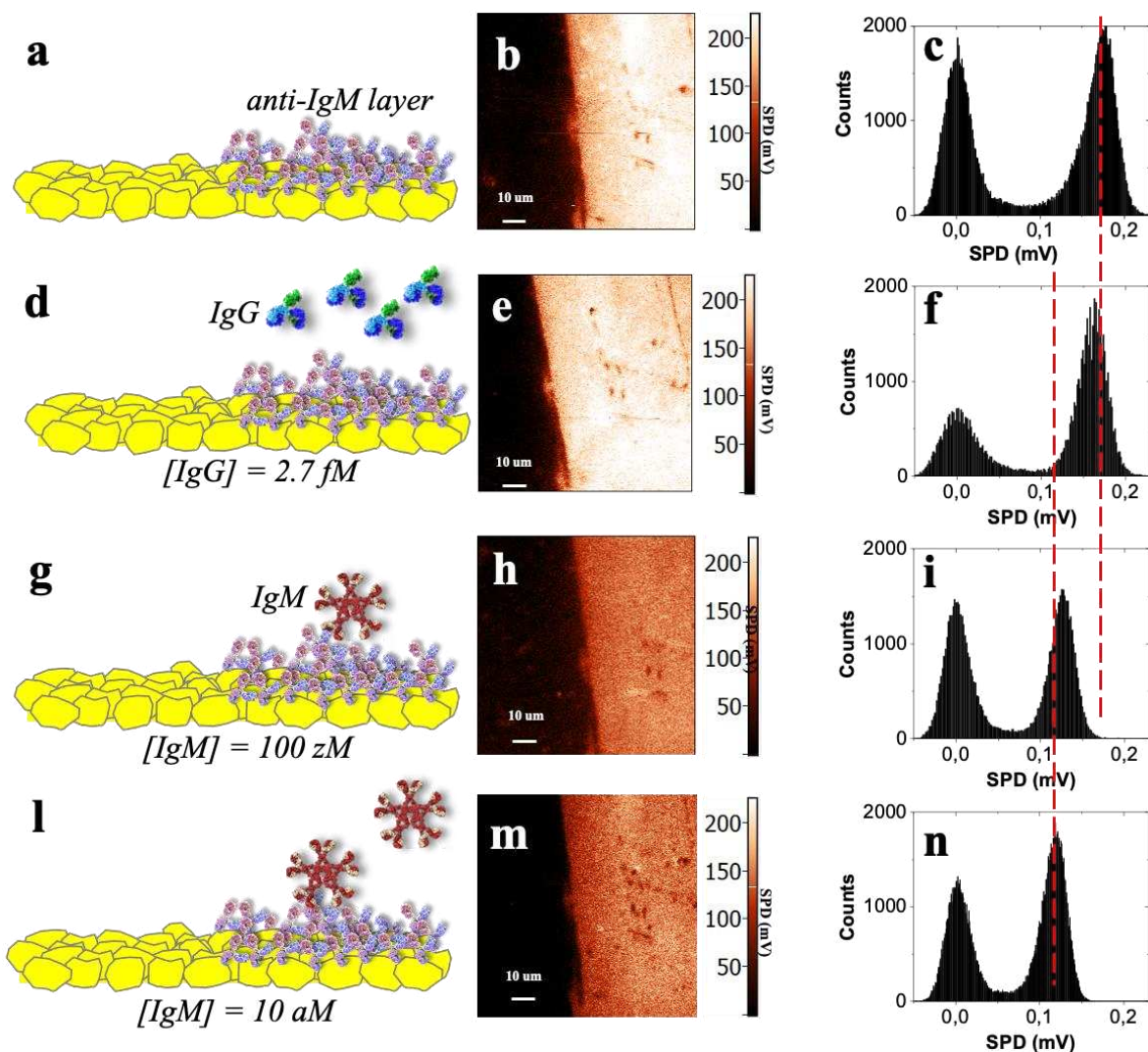


**Figure 4.10** Surface potential changes induced by affinity binding events. (a) Cross-sectional diagram and (b) KPFM scan ( $90\ \mu\text{m} \times 90\ \mu\text{m}$ ) showing the boundary between bare Au (left) and anti-IgM modified gold (right) regions, where anti-IgM acts as the recognition layer. (c) Distribution plot showing surface potential differences (SPD) relative to the bare Au peak value. Sets {d,e,f}, {g,h,i}, and {l,m,n} mirror {a,b,c}, displaying cross-sections, KPFM measurements, and SPD distributions after sequential exposure to: non-specific IgG ( $3\ \text{fM}$ ) as negative control, specific IgM ( $100\ \text{zM}$ ), and higher concentration IgM ( $10\ \text{aM}$ ), as illustrated in panels d, g, and l.

The KPFM scans reveal a substantial shift impacting the entire  $90 \times 90\ \mu\text{m}^2$  area, which is covered by approximately  $6 \times 10^7$  anti-IgM capturing proteins. This widespread effect occurs despite the minimal number of IgM ligands (ranging from  $\sim 10$  to  $10^3$ ) exhibited in the 100 mL incubation volume capable of interacting with the broad anti-IgM-covered surface via diffusion. [103] These observations offer strong experimental evidence that even a limited

number of antigen-antibody binding events can lead to significant changes in work function. Such alterations are observed across large-scale biofunctionalized Au surfaces.

Figure 4.11 presents a comprehensive analysis of the  $\Delta\phi$  data examined in Figure 4.10, measured across up to three distinct Au/anti-IgM samples, plotted against IgM concentration. The error bars represent a single standard deviation of the SPD distribution within the examined area. Notably, a significant  $\Delta\phi$  shift is observed at concentrations as low as 100 zM (corresponding to less than 10 IgM proteins in 100 mL), while no feedback is detected when the electrode is shown to a significantly higher concentrated IgG solution (3 fM, approximately  $10^5$  IgG in 100 mL).

A comparative assessment is facilitated by exposing Au/anti-IgM gate electrodes to PBS solutions containing differing analytes: IgM at a concentration of 3 fM, and IgG across a broad range (from 100 zM to 100 aM, with an intermediate 10 aM). The resultant electrode interactions are characterized utilizing advanced SiMoT transistor technology, incorporating an electrolyte-gated design. [104,105] Figure 4.11b shows a schematic representation of the SiMoT device structure, accompanied by typical transfer features presented in Figure 4.11c. From these characteristics explained in Figure 4.7, the threshold voltage change,  $\Delta V_T$ , is derived.

Extracting parameters from the current-voltage characteristics of organic field-effect transistors. An analytical model for organic-based transistors) Figure 4.11d displays the  $\Delta V_T$  data for three measurements.

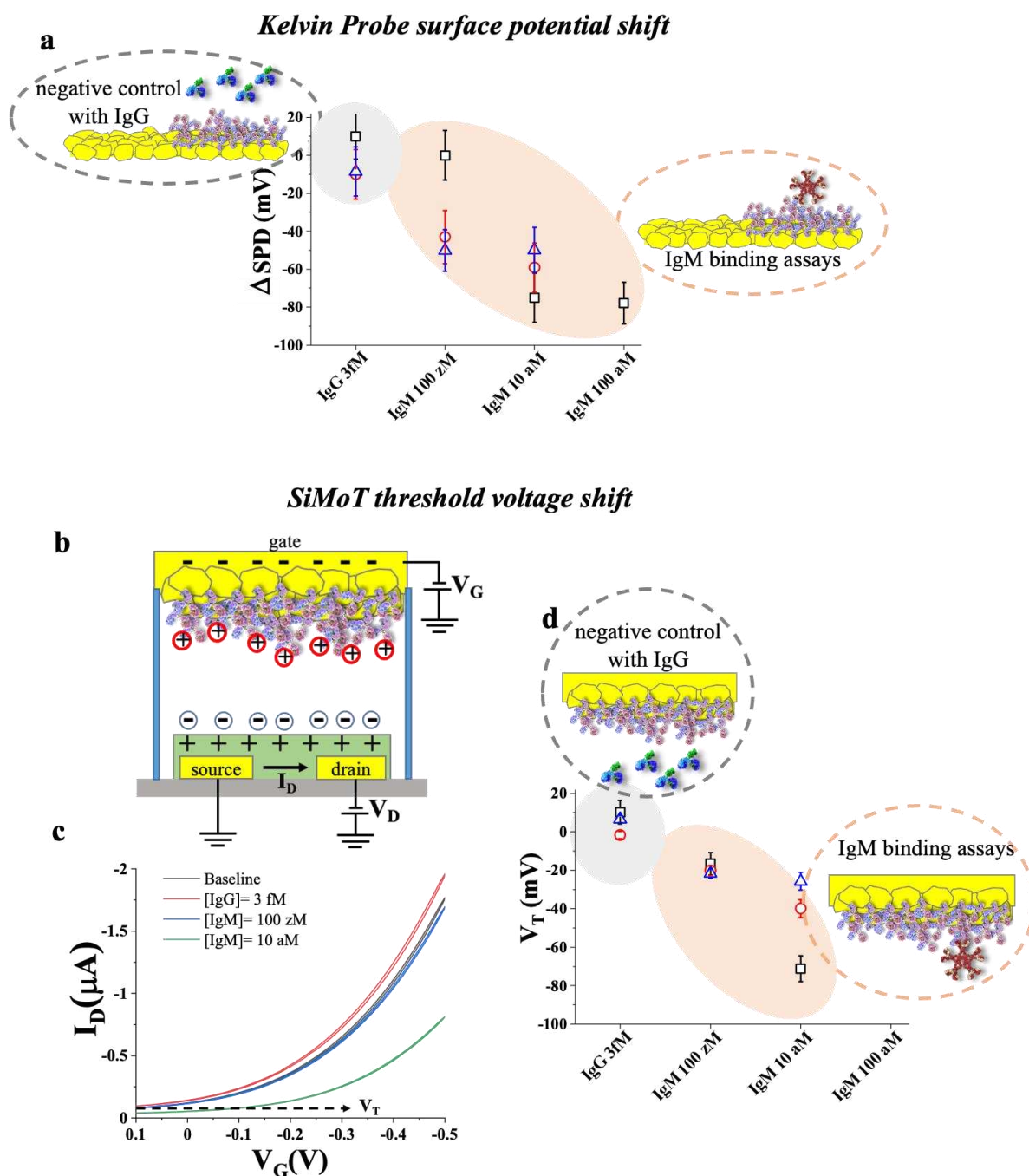


**Figure 4.11** Comparable responses observed in KPFM and SiMoT measurements of Au/anti-IgM electrodes at matching IgM levels. (a) Surface potential difference changes ( $\Delta\text{SPD}$ ) measured at different IgM concentrations, referenced to bare gold values. Electrodes were tested with IgM (3 fM) and IgG solutions (100 zM, 10 aM, and 100 aM) in PBS. (b) Diagram showing SiMoT device configuration, with gate area of  $5 \times 10^{-1} \text{ cm}^2$  and anti-IgM density of  $2 \times 10^{12} \text{ cm}^{-2}$ . (c) Representative current-voltage characteristics ( $I_D$  vs.  $V_G$ ) at  $V_D = -0.4 \text{ V}$  for samples matching panel (a). (d) Threshold voltage shifts ( $\Delta V_T$ ) extracted from transfer curves. Data points show means with standard deviations from triplicate measurements.

The comparison between the KPFM and SiMoT responses reveals a remarkable correlation between the threshold voltage shift and the surface potential change. Specifically, the threshold voltage shift ( $\Delta V_T$ ) of approximately  $-60 \pm 30$  mV closely aligns with the surface potential change ( $\Delta SPD$ ) of about  $-60 \pm 20$  mV.

The detection of individual proteins in 100 mL volumes by SiMoT was first time reported in 2018 [104] and since has been demonstrated across various sensing platforms. [106–110] Research has shown that a single antigen among ten in 100 mL can reach a millimeter-wide surface via Brownian diffusion within 10 minutes. [111] Notably, cutting-edge research has successfully showcased the feasibility of detecting individual molecules electronically, with the help of a novel capture layer design that incorporates a vast array of antibodies, estimated in the trillions, which are gently anchored via physisorption. [112] The SiMoT effect is remarkable because the footprint of a single protein ( $\sim 10^{-4}$   $\mu\text{m}^2$ ) is approximately  $10^9$  times smaller than the large-area gate transducer ( $\sim 10^5$   $\mu\text{m}^2$ ). This allows for the detection of a single IgM molecule on a surface covered with trillions of capturing antibodies, highlighting the sensitivity of the method. Both scenarios would typically stem in single-binding event signals being indistinguishable from background noise. However, this is not observed in practice. The KPFM AFM data presented here provide direct and unequivocal evidence that the binding of fewer than 10 IgMs to an equal number of anti-IgMs alters the surface potential of at least  $10^8$  anti-IgMs densely packed on a  $90 \times 90$   $\mu\text{m}^2$  gate area. The findings suggest a cascade-like amplification process, wherein the attachment of alone molecule to its corresponding capture antibody triggers a subtle yet profound alteration in the local electrostatic field or dipole moment, which in turn, sets off a self-sustaining chain reaction, akin to a row of toppled dominoes, enhancing the overall signal. This small initial change triggers a response that extends to numerous neighboring antibodies, effectively amplifying the signal across the entire surface. This mechanism enhances sensitivity, allowing even minute molecular interactions to produce detectable electronic signals.

Initially, the proposed mechanism was thought to depend on a collaborative effect among dipoles within a hydrogen-bonded lattice, linked to the antibody-stabilized self-assembled monolayer. [104] However, the effectiveness of even a barely physisorbed layer [104] suggests that electrostatic coupling on densely populated gate surfaces enables the spread of a localized electrostatic perturbation triggered by a single capturing antibody.

Recent research has demonstrated long-range charge reorganization concurrent with conformational changes during affinity binding. [113] Additionally, studies on liquid crystals have shown that dipolar mesogens can propagate structural reorientation over micrometers when an affinity binding occurs with a protein attached to the liquid crystal surface. [114] The process entails the coordinated realignment of millions of mesogenic units for each protein bound. Notably, our observations render it credible that a single protein's affinity binding can trigger a cascading electrostatic dipole reorientation, engaging hundreds of millions of antibody-associated dipoles.

#### **4.7 Surface Potential shifts induced by few binding events**

To explain the affinity-binding properties of immunoglobulin IgM, we analyzed the distribution of surface potential changes following incubation with Au/anti-IgM in standardized PBS solutions across a concentration gradient (100 nM, 10 nM, and 100 nM). A negative control experiment utilized IgG at 3 nM in PBS to validate specificity. For a detailed description of the experimental protocol, please refer to the Method section. The Au/anti-IgM interface was examined using KPFM, with a notable adjustment in the second scan: maintaining the probe tip at a consistent 250 nm distance from the surface. Figure 4.12 presents a comprehensive visual representation of the KPFM imaging at each critical step of the recognition assay, compiled from two independent data sets, thereby ensuring reliability and reproducibility.

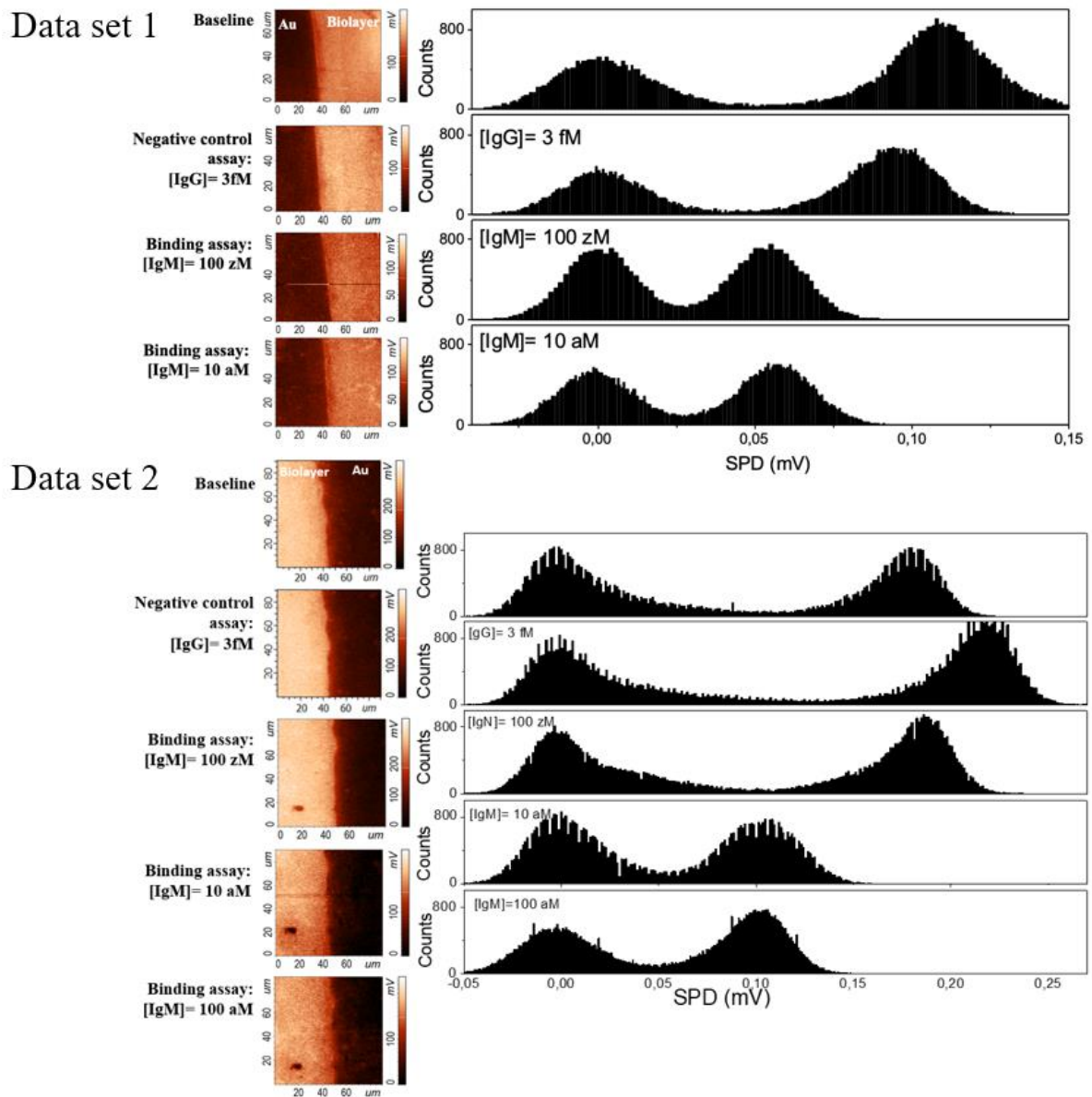


*Figure 4.12 SP changes induced by the formation of anti-IgM/IgM biocomplex and the corresponding histograms of the SP distributions.*

# Chapter 5 Conclusion and Future Perspectives

## Conclusion

The comparative study of anti-IgM clusters and films on gold substrates using AFM and AM-AFM techniques provides valuable insights into their nanomechanical properties and behaviors. The results indicate significant differences in mechanical properties between anti-IgM clusters and films, highlighting the critical role of protein organization in influencing their performance and interactions with surfaces. The topography analysis reveals that anti-IgM clusters exhibit irregular shapes with varying heights, while the film presents a more uniform and compact structure. These morphological differences directly influence their mechanical properties. The Young's modulus for protein clusters, averaging 0.19 GPa, is significantly lower than that of the protein film, which averages 0.68 GPa. This suggests that the clusters have a less dense and more disordered arrangement, resulting in weaker intermolecular interactions and increased flexibility, while the films are more compact and resistant to deformation. Stiffness measurements further support this finding, with the protein film exhibiting higher stiffness 3.60 N/m compared to the clusters 2.47 N/m. This difference in stiffness likely results from stronger non-covalent interactions in the film, which enhance its structural integrity. Adhesion force analysis shows that protein clusters have higher adhesion 1.49 nN than the film 1.07 nN, indicating that the larger surface area and higher protein density in clusters promote more significant molecular interactions with the substrate. Energy dissipation in AM-AFM experiments further supported these findings. The dissipation patterns in the protein clusters and films provided insights into the nature of long-range electrostatic and van der Waals forces. Protein clusters exhibited higher energy dissipation in the attractive regime, indicating softer, less ordered structures, while the stiffer protein films showed lower dissipation due to their more compact arrangement. The observed differences in Young's modulus, stiffness, and adhesion force between clusters and films underscore the complex interplay between protein structure, substrate interaction, and mechanical properties. These findings have implications for the design of protein-based materials and biosensors, where optimizing protein organization could enhance performance and stability.

Additionally, The results from KPFM and SiMoT measurements on Au/anti-IgM surfaces highlight key insights into the structural and electrostatic properties of the bio-

functionalized interfaces. AFM revealed an increase in surface roughness after anti-IgM functionalization, indicating a dense layer of antibodies. KPFM showed higher surface potential for anti-IgM regions due to antibody dipoles, which alter the local electrostatic environment, essential for biosensing.

Both KPFM and SiMoT demonstrated high sensitivity to IgM detection, with measurable surface potential and threshold voltage shifts at concentrations as low as 100 zM. This suggests that even minimal IgM binding events trigger significant electrostatic changes, amplified across the densely packed anti-IgM layer. The electrostatic amplification mechanism enhances the platform's sensitivity, making it highly effective for detecting small molecular interactions, critical for advanced biosensing applications like medical diagnostics.

## **Future perspective**

Building on the findings of this thesis, future work can explore several key areas to further advance the understanding and application of protein films in biosensors and bioactive materials. First, more detailed studies on the long-term stability and functionality of physisorbed protein layers under varying environmental conditions (e.g., temperature, pH, and humidity) are essential to ensure their reliability in real-world applications. Investigating different protein types, beyond anti-IgM antibodies, and substrates can provide broader insights into how the mechanical properties of various proteins influence their performance in biosensing platforms.

## References

1. D. B. Jones and A. P. J. Middelberg, "Direct determination of the mechanical properties of an interfacially adsorbed protein film," *Chem Eng Sci* **57**, 1711–1722 (2002).
2. "Serum IgM to *Chlamydia trachomatis* in pregnancy: its usefulness for screening," (n.d.).
3. R. Afrin, M. T. Alam, and A. Ikai, "Pretransition and progressive softening of bovine carbonic anhydrase II as probed by single molecule atomic force microscopy," *Protein Science* **14**, 1447–1457 (2005).
4. R. Afrin, M. T. Alam, and A. Ikai, "Pretransition and progressive softening of bovine carbonic anhydrase II as probed by single molecule atomic force microscopy," *Protein Science* **14**, 1447–1457 (2005).
5. H. Wang, S. Lin, X. Wu, K. Jiang, H. Lu, and C. Zhan, "Interplay between Liposomes and IgM: Principles, Challenges, and Opportunities," *Advanced Science* **10**, 2301777 (2023).
6. H. Wang, S. Lin, X. Wu, K. Jiang, H. Lu, and C. Zhan, "Interplay between Liposomes and IgM: Principles, Challenges, and Opportunities," *Advanced Science* **10**, 2301777 (2023).
7. J. E. Kohn and K. W. Plaxco, "Engineering a signal transduction mechanism for protein-based biosensors," *Proceedings of the National Academy of Sciences* **102**, 10841–10845 (2005).
8. E. M. Puchner and H. E. Gaub, "Force and function: probing proteins with AFM-based force spectroscopy," *Curr Opin Struct Biol* **19**, 605–614 (2009).
9. P. Hinterdorfer and Y. F. Dufrêne, "Detection and localization of single molecular recognition events using atomic force microscopy," *Nature Methods* 2006 3:5 **3**, 347–355 (2006).
10. R. Ferreira, P. A. Ribeiro, A. V. M. Canário, and M. Raposo, "Biosensors Based on Stanniocalcin-1 Protein Antibodies Thin Films for Prostate Cancer Diagnosis," *Biosensors* 2023, Vol. 13, Page 981 **13**, 981 (2023).

11. R. J. Mosley, M. V. Talarico, and M. E. Byrne, "Recent applications of QCM-D for the design, synthesis, and characterization of bioactive materials," *J Bioact Compat Polym* **36**, 261–275 (2021).
12. I. Willner and B. Willner, "Biomolecule-based nanomaterials and nanostructures," *Nano Lett* **10**, 3805–3815 (2010).
13. N. A. Burnham and R. J. Colton, "Measuring the nanomechanical properties and surface forces of materials using an atomic force microscope," *Journal of Vacuum Science & Technology A* **7**, 2906–2913 (1989).
14. D. Su and X. Li, "Investigation of Near-Surface Mechanical Properties of Materials Using Atomic Force Microscopy," *Exp Mech* **54**, 11–24 (2014).
15. D. B. Jones and A. P. J. Middelberg, "Direct determination of the mechanical properties of an interfacially adsorbed protein film," *Chem Eng Sci* **57**, 1711–1722 (2002).
16. R. Afrin, M. T. Alam, and A. Ikai, "Pretransition and progressive softening of bovine carbonic anhydrase II as probed by single molecule atomic force microscopy," *Protein Science* **14**, 1447–1457 (2005).
17. M. Schlierf and M. Rief, "Temperature Softening of a Protein in Single-molecule Experiments," *J Mol Biol* **354**, 497–503 (2005).
18. A. Parra, E. Casero, E. Lorenzo, F. Pariente, and L. Vázquez, "Nanomechanical properties of globular proteins: Lactate oxidase," *Langmuir* **23**, 2747–2754 (2007).
19. E. M. Puchner and H. E. Gaub, "Force and function: probing proteins with AFM-based force spectroscopy," *Curr Opin Struct Biol* **19**, 605–614 (2009).
20. D. Martinez-Martin, E. T. Herruzo, C. Dietz, J. Gomez-Herrero, and R. Garcia, "Noninvasive protein structural flexibility mapping by bimodal dynamic force microscopy," *Phys Rev Lett* **106**, 198101 (2011).
21. F. Rico, C. Su, and S. Scheuring, "Mechanical mapping of single membrane proteins at submolecular resolution," *Nano Lett* **11**, 3983–3986 (2011).
22. A. P. Perrino and R. Garcia, "How soft is a single protein? The stress–strain curve of antibody pentamers with 5 pN and 50 pm resolutions," *Nanoscale* **8**, 9151–9158 (2016).

23. A. F. Payam, R. Funari, G. Scamarcio, and N. Bhalla, "Sensing Dynamically Evolved Short-Range Nanomechanical Forces in Fast-Mutating Single Viral Spike Proteins," *Small Science* **3**, 2300029 (2023).
24. H. Wang, S. Lin, X. Wu, K. Jiang, H. Lu, and C. Zhan, "Interplay between Liposomes and IgM: Principles, Challenges, and Opportunities," *Advanced Science* **10**, 2301777 (2023).
25. N. Saito, K. Hayashi, H. Sugimura, O. Takai, and N. Nakagiri, "Surface potentials of patterned organosilane self-assembled monolayers acquired by Kelvin probe force microscopy and ab initio molecular calculation," *Chem Phys Lett* **349**, 172–177 (2001).
26. L. E. Cheran, M. Chacko, M. Zhang, and M. Thompson, "Protein microarray scanning in label-free format by Kelvin nanoprobe," *Analyst* **129**, 161–168 (2004).
27. A. K. Sinensky and A. M. Belcher, "Label-free and high-resolution protein/DNA nanoarray analysis using Kelvin probe force microscopy," *Nature Nanotechnology* **2**:10 **2**, 653–659 (2007).
28. T. Ichii, T. Fukuma, K. Kobayashi, H. Yamada, and K. Matsushige, "Surface potential measurements of phase-separated alkanethiol self-assembled monolayers by non-contact atomic force microscopy," *Nanotechnology* **15**, S30 (2004).
29. D. Zhou, K. Sinniah, C. Abell, T. R.-C. I. Edition, and undefined 2003, "Label-free detection of DNA hybridization at the nanoscale: a highly sensitive and selective approach using atomic-force microscopy," academia.edu D Zhou, K Sinniah, C Abell, T Rayment *Angewandte Chemie International Edition*, 2003 • academia.edu (n.d.).
30. H. D. Ou-Yang and M. T. Wei, "Complex fluids: Probing mechanical properties of biological systems with optical tweezers," *Annu Rev Phys Chem* **61**, 421–440 (2010).
31. C. H. Chiou, Y. Y. Huang, M. H. Chiang, H. H. Lee, and G. Bin Lee, "New magnetic tweezers for investigation of the mechanical properties of single DNA molecules," *Nanotechnology* **17**, 1217 (2006).
32. K. Guevorkian and J. L. Maître, "Micropipette aspiration: A unique tool for exploring cell and tissue mechanics in vivo," *Methods Cell Biol* **139**, 187–201 (2017).

33. J. Israelachvili, Y. Min, M. Akbulut, A. Alig, G. Carver, W. Greene, K. Kristiansen, E. Meyer, N. Pesika, K. Rosenberg, and H. Zeng, "Recent advances in the surface forces apparatus (SFA) technique," *Reports on Progress in Physics* **73**, 036601 (2010).
34. N. E. Kurland, Z. Drira, and V. K. Yadavalli, "Measurement of nanomechanical properties of biomolecules using atomic force microscopy," *Micron* **43**, 116–128 (2012).
35. J. Bonander, B. K.-A. P. Letters, and undefined 2008, "Cantilever based optical interfacial force microscope," *pubs.aip.org* (2008).
36. R. J. Mosley, M. V. Talarico, and M. E. Byrne, "Recent applications of QCM-D for the design, synthesis, and characterization of bioactive materials," *J Bioact Compat Polym* **36**, 261–275 (2021).
37. A. Viljoen, M. Mathelié-Guinlet, A. Ray, N. Strohmeyer, Y. J. Oh, P. Hinterdorfer, D. J. Müller, D. Alsteens, and Y. F. Dufrêne, "Force spectroscopy of single cells using atomic force microscopy," *Nature Reviews Methods Primers* 2021 1:1 **1**, 1–24 (2021).
38. D. J. Müller, A. C. Dumitru, C. Lo Giudice, H. E. Gaub, P. Hinterdorfer, G. Hummer, J. J. De Yoreo, Y. F. Dufrêne, and D. Alsteens, "Atomic Force Microscopy-Based Force Spectroscopy and Multiparametric Imaging of Biomolecular and Cellular Systems," *Chem Rev* **121**, 11701–11725 (2021).
39. M. Pfreundschuh, D. Alsteens, M. Hilbert, M. O. Steinmetz, and D. J. Müller, "Localizing chemical groups while imaging single native proteins by high-resolution atomic force microscopy," *Nano Lett* **14**, 2957–2964 (2014).
40. I. D. Medalsy and D. J. Müller, "Nanomechanical properties of proteins and membranes depend on loading rate and electrostatic interactions," *ACS Nano* **7**, 2642–2650 (2013).
41. T. R. Rodríguez and R. García, "Compositional mapping of surfaces in atomic force microscopy by excitation of the second normal mode of the microcantilever," *Appl Phys Lett* **84**, 449–451 (2004).
42. U. Rabe, S. Amelio, M. Kopycinska, S. Hirsekorn, M. Kempf, M. Göken, and W. Arnold, "Imaging and measurement of local mechanical material properties by atomic force acoustic microscopy," *Surface and Interface Analysis* **33**, 65–70 (2002).

43. N. Huda Shaik, R. G Reifenberger, and A. Raman, "Nanomechanical mapping in air or vacuum using multi-harmonic signals in tapping mode atomic force microscopy," *Nanotechnology* **31**, 455502 (2020).
44. O. Sahin, S. Magonov, C. Su, C. F. Quate, and O. Solgaard, "An atomic force microscope tip designed to measure time-varying nanomechanical forces," *Nature Nanotechnology* **2**, 507–514 (2007).
45. S. Gopalakrishnan, J. Xu, F. Zhong, V. M. Rotello, S. Gopalakrishnan, J. Xu, V. M. Rotello, and F. Zhong, "Strategies for Fabricating Protein Films for Biomaterial Applications," *Adv Sustain Syst* **5**, 2000167 (2021).
46. V. L. Popov, "Contact mechanics and friction: Physical principles and applications, second edition," *Contact Mechanics and Friction: Physical Principles and Applications, Second Edition* 1–391 (2017).
47. S. Kim, Y. Lee, M. Lee, S. An, and S. J. Cho, "Quantitative Visualization of the Nanomechanical Young's Modulus of Soft Materials by Atomic Force Microscopy," *Nanomaterials* **11**, 1593 (2021).
48. S. Kasas, G. Longo, and G. Dietler, "Mechanical properties of biological specimens explored by atomic force microscopy," *J Phys D Appl Phys* **46**, 133001 (2013).
49. R. Benítez, V. Bolós, J. T.-H.-R. J., and undefined 2017, "afmToolkit: an R Package for Automated AFM Force-Distance Curves Analysis.," *rjournal.github.io* R Benítez, VJ Bolós, JL Toca-Herrera R J., 2017•*rjournal.github.io* (n.d.).
50. R. M. A. Sullan, J. K. Li, and S. Zou, "Direct correlation of structures and nanomechanical properties of multicomponent lipid bilayers," *Langmuir* **25**, 7471–7477 (2009).
51. M. D. A. Norman, S. A. Ferreira, G. M. Jowett, L. Bozec, and E. Gentleman, "Measuring the elastic modulus of soft culture surfaces and three-dimensional hydrogels using atomic force microscopy," *Nature Protocols* **16**, 2418–2449 (2021).
52. S. V. Kontomaris, A. Stylianou, K. S. Nikita, A. Malamou, and T. Stylianopoulos, "A simplified approach for the determination of fitting constants in Oliver–Pharr method regarding biological samples," *Phys Biol* **16**, 056003 (2019).

53. B. Cappella and D. Silbernagl, "Nanomechanical properties of polymer thin films measured by force–distance curves," *Thin Solid Films* **516**, 1952–1960 (2008).
54. B. Bhushan and O. Marti, "Scanning probe microscopy- Principle of operation, instrumentation, and probes," *Nanotribology and Nanomechanics: An Introduction: Fourth Edition* 33–93 (2017).
55. W. Zhou, R. Apkarian, Z. L. Wang, and D. Joy, "Fundamentals of Scanning Electron Microscopy (SEM)," *Scanning Microscopy for Nanotechnology: Techniques and Applications* 1–40 (2006).
56. J. N. Munday, F. Capasso, and V. A. Parsegian, "Measured long-range repulsive Casimir–Lifshitz forces," *Nature* 2009 457:7226 **457**, 170–173 (2009).
57. J. Israelachvili, *Intermolecular and Surface Forces* (2011).
58. T. Stifter, O. Marti, and B. Bhushan, "Theoretical investigation of the distance dependence of capillary and van der Waals forces in scanning force microscopy," *Phys Rev B Condens Matter Mater Phys* **62**, 13667–13673 (2000).
59. Y. Sugimoto, P. Pou, M. Abe, P. Jelinek, R. Pérez, S. M.- Nature, and undefined 2007, "Chemical identification of individual surface atoms by atomic force microscopy," [nature.com](http://nature.com) Y Sugimoto, P Pou, M Abe, P Jelinek, R Pérez, S Morita, O Custance Nature, 2007 •nature.com (n.d.).
60. A. Payam, D. Martin-Jimenez, R. G.- Nanotechnology, and undefined 2015, "Force reconstruction from tapping mode force microscopy experiments," [iopscience.iop.org](http://iopscience.iop.org) AF Payam, D Martin-Jimenez, R Garcia Nanotechnology, 2015 •iopscience.iop.org **26**, 185706 (2015).
61. S. de Beer, D. van den Ende, D. Ebeling, and F. Mugele, "Small Amplitude Atomic Force Spectroscopy," *NanoScience and Technology* **116**, 39–58 (2011).
62. H. H.-A. P. Letters and undefined 2006, "Quantitative measurement of tip-sample interactions in amplitude modulation atomic force microscopy," [pubs.aip.org](http://pubs.aip.org) **89**, (1231).
63. K.-M. Microscopy, J.-Y. Yang, M.-F. Chung, A. Hsieh, O. E. Dagdeviren, J. Götzen, H. Hölscher, E. I. Altman, and U. D. Schwarz, "Robust high-resolution imaging and quantitative force measurement with tuned-oscillator atomic force microscopy,"

- iopscience.iop.orgOE Dagdeviren, J Götzen, H Hölscher, EI Altman, UD SchwarzNanotechnology, 2016•iopscience.iop.org (2016).
64. M. Lee, W. J.-P. review letters, and undefined 2006, "General theory of amplitude-modulation atomic force microscopy," APSM Lee, W JhePhysical review letters, 2006•APS **97**, (2006).
  65. B. Rajabifar, R. Wagner, A. Raman, and S. Hu, "Inverting amplitude and phase to reconstruct tip-sample interaction forces in tapping mode atomic force microscopy," iopscience.iop.orgS Hu, A RamanNanotechnology, 2008•iopscience.iop.org **19**, 11 (2008).
  66. J. Hwang, J. P. Carbotte -, A. Yadav, M. Danesh, L. Zhong, al -, B. Eslami, E. A. López-Guerra, A. J. Diaz, A. J. Katan, M. H. van Es, and T. H. Oosterkamp, "Quantitative force versus distance measurements in amplitude modulation AFM: a novel force inversion technique," iopscience.iop.orgAJ Katan, MH Van Es, TH OosterkampNanotechnology, 2009•iopscience.iop.org **20**, 9 (2009).
  67. A. Payam, D. Martin-Jimenez, R. G.- Nanotechnology, and undefined 2015, "Force reconstruction from tapping mode force microscopy experiments," iopscience.iop.orgAF Payam, D Martin-Jimenez, R GarciaNanotechnology, 2015•iopscience.iop.org **26**, 185706 (2015).
  68. R. Garcia, R. P.-S. science reports, and undefined 2002, "Dynamic atomic force microscopy methods," Elsevier (n.d.).
  69. H. H.-S. science and undefined 2002, "Q-controlled dynamic force spectroscopy," Elsevier (n.d.).
  70. A. Rita. Bizzarri and Salvatore. Cannistraro, "Dynamic force spectroscopy and biomolecular recognition," 256 (2012).
  71. J. Cleveland, B. Anczykowski, ... A. S.-A. P., and undefined 1998, "Energy dissipation in tapping-mode atomic force microscopy," pubs.aip.org (n.d.).
  72. M. Nonnenmacher, ... M. o'Boyle-A. physics, and undefined 1991, "Kelvin probe force microscopy," pubs.aip.org (n.d.).
  73. W. Melitz, J. Shen, A. Kummel, S. L.-S. science reports, and undefined 2011, "Kelvin probe force microscopy and its application," Elsevier (n.d.).

74. W. Z.-R. of S. Instruments and undefined 1932, "A new method of measuring contact potential differences in metals," [pubs.aip.org](https://pubs.aip.org) (n.d.).
75. B. Moores, F. Hane, L. Eng, and Z. Leonenko, "Kelvin probe force microscopy in application to biomolecular films: Frequency modulation, amplitude modulation, and lift mode," *Ultramicroscopy* **110**, 708–711 (2010).
76. M. Nonnenmacher, M. P. O'Boyle, and H. K. Wickramasinghe, "Kelvin probe force microscopy," *Appl Phys Lett* **58**, 2921–2923 (1991).
77. B. Cappella and D. Silbernagl, "Nanomechanical properties of polymer thin films measured by force–distance curves," *Thin Solid Films* **516**, 1952–1960 (2008).
78. L. Zhang, Y. Mazouzi, M. Salmain, B. Liedberg, and S. Boujday, "Antibody-Gold Nanoparticle Bioconjugates for Biosensors: Synthesis, Characterization and Selected Applications," *Biosens Bioelectron* **165**, 112370 (2020).
79. B. Lu, M. R. Smyth, and R. O'Kennedy, "Tutorial review. Oriented immobilization of antibodies and its applications in immunoassays and immunosensors," *Analyst* **121**, 29R-32R (1996).
80. L. Sarcina, C. Scandurra, C. Di Franco, M. Caputo, M. Catacchio, P. Bollella, G. Scamarcio, E. Macchia, and L. Torsi, "A stable physisorbed layer of packed capture antibodies for high-performance sensing applications," *J Mater Chem C Mater* **11**, 9093–9106 (2023).
81. J. J. Ramsden, "Puzzles and paradoxes in protein adsorption," *Chem Soc Rev* **24**, 73–78 (1995).
82. A. Schmitt, R. Varoqui, S. Uniyal, J. L. Brash, and C. Pusineri, "Interaction of fibrinogen with solid surfaces of varying charge and hydrophobic—hydrophilic balance: I. Adsorption isotherms," *J Colloid Interface Sci* **92**, 25–34 (1983).
83. K. Manoli, M. Magliulo, M. Y. Mulla, M. Singh, L. Sabbatini, G. Palazzo, and L. Torsi, "Printable Bioelectronics To Investigate Functional Biological Interfaces," *Angewandte Chemie International Edition* **54**, 12562–12576 (2015).
84. J. E. Sader, J. W. M. Chon, and P. Mulvaney, "Calibration of rectangular atomic force microscope cantilevers," *Review of Scientific Instruments* **70**, 3967–3969 (1999).

85. B. Anczykowski, D. Krüger, and H. Fuchs, "Cantilever dynamics in quasiconnact force microscopy: Spectroscopic aspects," *Phys Rev B* **53**, 15485 (1996).
86. H. Hölscher, J.-E. Schmutz, and U. D. Schwarz, "Dynamic Force Microscopy and Spectroscopy in Ambient Conditions: Theory and Applications," *Scanning Probe Microscopy of Functional Materials* 71–94 (2010).
87. E. Macchia, K. Manoli, B. Holzer, C. Di Franco, M. Ghittorelli, F. Torricelli, D. Alberga, G. F. Mangiatordi, G. Palazzo, G. Scamarcio, and L. Torsi, "Single-molecule detection with a millimetre-sized transistor," *Nat Commun* **9**, (2018).
88. A. Liscio, V. Palermo, K. Müllen, and P. Samorì, "Tip–Sample Interactions in Kelvin Probe Force Microscopy: Quantitative Measurement of the Local Surface Potential," *Journal of Physical Chemistry C* **112**, 17368–17377 (2008).
89. D. Blasi, F. Viola, F. Modena, A. Luukkonen, E. MacChia, R. A. Picca, Z. Gounani, A. Tewari, R. Österbacka, M. Caironi, Z. M. Kovacs Vajna, G. Scamarcio, F. Torricelli, and L. Torsi, "Printed, cost-effective and stable poly(3-hexylthiophene) electrolyte-gated field-effect transistors," *J Mater Chem C Mater* **8**, 15312–15321 (2020).
90. B. Anczykowski, B. Gotsmann, H. Fuchs, J. P. Cleveland, and V. B. Elings, "How to measure energy dissipation in dynamic mode atomic force microscopy," *Appl Surf Sci* **140**, 376–382 (1999).
91. D. Martinez-Martin, E. T. Herruzo, C. Dietz, J. Gomez-Herrero, and R. Garcia, "Noninvasive protein structural flexibility mapping by bimodal dynamic force microscopy," *APSD Martínez-Martín, ET Herruzo, C Dietz, J Gomez-Herrero, R GarciaPhysical review letters, 2011•APS* **106**, (2011).
92. G. Song, "Bridging between material properties of proteins and the underlying molecular interactions," *PLoS One* **16**, e0247147 (2021).
93. S. Zhang, O. Felthaus, L. Prantl, N. Ma, and R. MacHatschek, "Continuous protein-density gradients: A new approach to correlate physical cues with cell response," *PNAS Nexus* **3**, (2024).
94. Z. Lv, J. Wang, G. Chen, and L. Deng, "Probing specific interaction forces between human IgG and rat anti-human IgG by self-assembled monolayer and atomic force microscopy," *Nanoscale Res Lett* **5**, 1032–1038 (2010).

95. E. Macchia, D. Alberga, K. Manoli, G. F. Mangiatordi, M. Magliulo, G. Palazzo, F. Giordano, G. Lattanzi, and L. Torsi, "Organic bioelectronics probing conformational changes in surface confined proteins," *Sci Rep* **6**, 28085 (2016).
96. M. Nonnenmacher, M. P. O'Boyle, and H. K. Wickramasinghe, "Kelvin probe force microscopy," *Appl Phys Lett* **58**, 2921–2923 (1991).
97. N. H. Thomson, "The substructure of immunoglobulin G resolved to 25 kDa using amplitude modulation AFM in air," *Ultramicroscopy* **105**, 103–110 (2005).
98. S. Emaminejad, M. Javanmard, C. Gupta, S. Chang, R. W. Davis, and R. T. Howe, "Tunable control of antibody immobilization using electric field," *National Acad Sciences* S Emaminejad, M Javanmard, C Gupta, S Chang, RW Davis, RT Howe *Proceedings of the National Academy of Sciences*, 2015 • National Acad Sciences **112**, 1995–1999 (2015).
99. C. Loppacher, "Electronic properties of Metal/Organic interfaces," in *Springer Series in Surface Sciences* (2012), Vol. 48, pp. 221–241.
100. N. Turetta, F. Sedona, A. Liscio, M. Sambì, and P. Samorì, "Au(111) Surface Contamination in Ambient Conditions: Unravelling the Dynamics of the Work Function in Air," *Adv Mater Interfaces* **8**, (2021).
101. B. Holzer, K. Manoli, N. Ditaranto, E. Macchia, A. Tiwari, C. Di Franco, G. Scamarcio, G. Palazzo, and L. Torsi, "Characterization of Covalently Bound Anti-Human Immunoglobulins on Self-Assembled Monolayer Modified Gold Electrodes," *Adv Biosyst* **1**, 1700055 (2017).
102. S. Casalini, A. C. Dumitru, F. Leonardi, C. A. Bortolotti, E. T. Herruzo, A. Campana, R. F. De Oliveira, T. Cramer, R. Garcia, and F. Biscarini, "Multiscale sensing of antibody-antigen interactions by organic transistors and single-molecule force spectroscopy," *ACS Nano* **9**, 5051–5062 (2015).
103. E. Macchia, L. De Caro, F. Torricelli, C. Di Franco, G. F. Mangiatordi, G. Scamarcio, and L. Torsi, "Why a Diffusing Single-Molecule can be Detected in Few Minutes by a Large Capturing Bioelectronic Interface," *Wiley Online Library* E Macchia, L De Caro, F Torricelli, CD Franco, GF Mangiatordi, G Scamarcio, L Torsi *Advanced Science*, 2022 • Wiley Online Library **9**, (2022).

104. E. Macchia, K. Manoli, B. Holzer, C. Di Franco, M. Ghittorelli, F. Torricelli, D. Alberga, G. F. Mangiatordi, G. Palazzo, G. Scamarcio, and L. Torsi, "Single-molecule detection with a millimetre-sized transistor," *Nature Communications* 2018 9:1 **9**, 1–10 (2018).
105. E. Macchia, F. Torricelli, P. Bollella, L. Sarcina, A. Tricase, C. Di Franco, R. Österbacka, Z. M. Kovács-Vajna, G. Scamarcio, and L. Torsi, "Large-Area Interfaces for Single-Molecule Label-free Bioelectronic Detection," *Chem Rev* **122**, 4636–4699 (2022).
106. E. Macchia, R. A. Picca, K. Manoli, C. Di Franco, D. Blasi, L. Sarcina, N. Ditaranto, N. Cioffi, R. Österbacka, G. Scamarcio, F. Torricelli, and L. Torsi, "About the amplification factors in organic bioelectronic sensors," *Mater Horiz* **7**, 999–1013 (2020).
107. E. Macchia, K. Manoli, C. Di Franco, R. A. Picca, R. Österbacka, G. Palazzo, F. Torricelli, G. Scamarcio, and L. Torsi, "Organic Field-Effect Transistor Platform for Label-Free, Single-Molecule Detection of Genomic Biomarkers," *ACS Sens* **5**, 1822–1830 (2020).
108. E. Macchia, L. Sarcina, R. A. Picca, K. Manoli, C. Di Franco, G. Scamarcio, and L. Torsi, "Ultra-low HIV-1 p24 detection limits with a bioelectronic sensor," *Anal Bioanal Chem* **412**, 811–818 (2020).
109. F. Torricelli, D. Z. Adrahtas, Z. Bao, M. Berggren, F. Biscarini, A. Bonfiglio, C. A. Bortolotti, C. D. Frisbie, E. Macchia, G. G. Malliaras, I. McCulloch, M. Moser, T. Q. Nguyen, R. M. Owens, A. Salleo, A. Spanu, and L. Torsi, "Electrolyte-gated transistors for enhanced performance bioelectronics," *Nature Reviews Methods Primers* 2021 1:1 **1**, 1–24 (2021).
110. F. Torricelli, D. Z. Adrahtas, Z. Bao, M. Berggren, F. Biscarini, A. Bonfiglio, C. A. Bortolotti, C. D. Frisbie, E. Macchia, G. G. Malliaras, I. McCulloch, M. Moser, T. Q. Nguyen, R. M. Owens, A. Salleo, A. Spanu, and L. Torsi, "Electrolyte-gated transistors for enhanced performance bioelectronics," *Nature Reviews Methods Primers* 2021 1:1 **1**, 1–24 (2021).
111. E. Macchia, L. De Caro, F. Torricelli, C. Di Franco, G. F. Mangiatordi, G. Scamarcio, and L. Torsi, "Why a Diffusing Single-Molecule can be Detected in Few Minutes by a Large Capturing Bioelectronic Interface," *Advanced Science* **9**, 2104381 (2022).

112. S. Sadewasser, P. Jelinek, C. K. Fang, O. Custance, Y. Yamada, Y. Sugimoto, M. Abe, and S. Morita, "New insights on atomic-Resolution frequency-Modulation kelvin-Probe force-Microscopy imaging of semiconductors," *Phys Rev Lett* **103**, 266103 (2009).
113. K. Banerjee-Ghosh, S. Ghosh, H. Mazal, I. Riven, G. Haran, and R. Naaman, "Long-Range Charge Reorganization as an Allosteric Control Signal in Proteins," *J Am Chem Soc* **142**, 20456–20462 (2020).
114. V. K. Gupta, J. J. Skaife, T. B. Dubrovsky, and N. L. Abbott, "Optical amplification of ligand-receptor binding using liquid crystals," *Science* (1979) **279**, 2077–2080 (1998).

## Publications

Cinzia Di Franco, Eleonora Macchia, Lucia Sarcina, Nicoletta Ditaranto, **Aniqa Khaliq**, Luisa Torsi, and Gaetano Scamarcio. "Extended Work Function Shift of Large-Area Biofunctionalized Surfaces Triggered by a Few Single-Molecule Affinity Binding Events." *Advanced Materials Interfaces* 10, no. 6 (2023): 2201829.

## Conference participation

1. "Anatomy of the transducing interface: the core of large-area label-free ultrasensitive electronic biosensors" Gaetano Scamarcio, Cinzia Di Franco, Eleonora Macchia, Angelo Tricase, Paolo Bollella, Lucia Sarcina, **Aniqa Khaliq**, Riccardo Funari, Luisa Torsi, 78th International Workshop & 6th Orbitaly, Erice, July 3-9, 2022
2. "Single molecule sensing via Kelvin Probe Force Microscopy" Cinzia Di Franco, Gaetano Scamarcio, Eleonora Macchia, Lucia Sarcina, **Aniqa Khaliq**, Luisa Torsi, 78th International Workshop & 6th Orbitaly, Erice, July 3-9, 2022
3. "Single-molecule affinity binding events induce extended work function shift of large-area bio-functionalized surfaces" Cinzia Di Franco, Eleonora Macchia, Lucia Sarcina, Nicoletta Ditaranto, **Aniqa Khaliq**, Luisa Torsi, and Gaetano Scamarcio, eBio-2022
4. "Mechanical properties of biofunctionalized thin films extracted by tapping mode AFM" **Aniqa Khaliq**, Cinzia Di Franco, Hendrik Hölscher, Riccardo Funari, Eleonora Macchia, Luisa Torsi and Gaetano Scamarcio, 16th European Conference of Molecular Electronics (ECME), Bari, Italy, 2-6 October 2023
5. "Influence of ligand exposure on the mechanical properties of biofunctionalized interfaces" Riccardo Funari, Cinzia Di Franco, **Aniqa Khaliq**, Eleonora Macchia, Luisa Torsi, Gaetano Scamarcio, 16th European Conference of Molecular Electronics (ECME), Bari, Italy, 2-6 October 2023
6. "Nanotecnologie per la rivelazione di singoli bio marcatori" C. Di Franco, M. Piscitelli, R. Funari, **A. Khaliq**, and G. Scamarcio, E. Macchia, L. Sarcina, C. Scandurra, M. Catacchio, M. Caputo, P. Boella, A. Tricase, and L. Torsi, BARI-Code, Italy, 23-25 October 2023

7. “Mechanical properties of bio-functionalized thin films extracted by tapping mode AFM”  
**Aniqa Khaliq**, Cinzia Di Franco, Hendrik Hölscher, Eleonora Macchia, Luisa Torsi and Gaetano Scamarcio, Conventional and High-Energy Spectroscopies for Inorganic, Organic and Biomolecular Surfaces and Interfaces, Brescia – Italy, 12-16 February 2024
8. “Mechanical properties of biofunctionalized thin films extracted by tapping mode AFM”  
**A. Khaliq**, C.D. Franco, H. Hölscher, E. Macchia, L. Torsi and G. Scamarcio, Biointerfaces International Conference (BIC), Switzerland, Muttenz, 20-23 August, 2024
9. “Single molecule detection at large bio-functionalized interfaces via Kelvin Probe Force Microscopy”  
Cinzia Di Franco, Matteo Piscitelli, **Aniqa Khaliq** , Eleonora Macchia, Cecilia Scandurra, Michele Catacchio, Lucia Sarcina, Mariapia Caputo, Luisa Torsi , and Gaetano Scamarcio, 32nd International Materials Research Congress (IMRC), México, Cancún, 18-23 August, 2024.

# Curriculum Vitae

## Aniqa Khaliq

### Biographic details

Date of Birth and place: 29 November 1994 in Lahore, Pakistan  
Nationality: Pakistani  
Home address: Via Napoli 29, 70123 Bari BA, Italy  
Phone: +39 3482364005  
Email: [aniqa.khaliq@uniba.it](mailto:aniqa.khaliq@uniba.it) – [aniqakhaliq94@gmail.com](mailto:aniqakhaliq94@gmail.com)

### About me

I am a PhD Physics student in the faculty of the Department of Physics as well as a researcher member of CNR-IFN Institute, living in Bari, Italy.

### Current Research Activity

My research focuses on investigating the mechanical properties of proteins when physisorbed onto a rigid gold substrate, both in films and clusters. This study is pivotal for advancing the development of single-molecule organic field-effect transistor (SiMoT) biosensors, which have the potential to revolutionize molecular diagnostics. By characterizing these properties, I aim to contribute to the optimization of SiMoT's performance in detecting biomolecular interactions.

Additionally, I am developing a diagnostic platform based on Kelvin Probe Force Microscopy (KPFM) to examine the forces and dynamics between ligands and receptors during immuno-complex formation. This work is crucial for understanding the surface phenomena that drive the amplified response of the SiMoT biosensor, thus improving its sensitivity and functionality in various biomedical applications.

### Education and training

**PhD Physics (Fully Funded Scholarship) Department of Physics, University of Bari, Italy**

**Date** 18/01/2021 – 17/09/2024

**Address** Via Giovanni Amendola, 173, Bari BA, Italy

**Website** <https://dottorato.fisica.uniba.it/>

**Laboratory Skills** Atomic Force Microscopy | Amplitude Modulation – Atomic Force Microscopy | Kelvin Probe Force Microscopy

**Thesis Title** Nanomechanical and Surface Potential Characterization of Protein Films via Atomic Force and Kelvin Probe Force Microscopy.

### **Achievements of Thesis**

- Developed a highly sensitive AFM-based methodology to characterize nanomechanical properties of anti-IgM protein films and clusters.
- Demonstrated significant differences in Young's modulus, stiffness, and adhesion forces between protein clusters and films.
- Introduced innovative KPFM and SiMoT techniques for detecting protein-antibody interactions at nanoscale.
- Achieved unprecedented sensitivity in detecting protein interactions down to zeptomolar concentrations.
- Contributed valuable insights for biomedical sensor development and immune response studies.

### **Master of Philosophy in Applied Physics**

**Institute** Center for Advanced Studies in Physics, GC University, Lahore, Pakistan

**Date** 10/09/2016 – 30/10/2018 – Lahore, Pakistan

**Address** Nabha Rd, Anarkali Bazaar Lahore, Pakistan

**Website** <https://www.gcu.edu.pk/CASP.php>

**Final grade CGPA** 3.41/4.00

**Research Skills** Laser ablation | Sputtering yield measurements | Laser-induced surface structuring | Quartz Crystal Microbalance | Scanning Electron Microscope

**Main Subjects** Laser Physics | Laser Matter Interaction | Experimental Plasma Physics | Physics of Materials

**Thesis** Magnetic confinement of laser induced Titanium plasma explored by laser induced breakdown spectroscopy

**Supervisor** Prof. Shazia Bashir

### **Work Experience**

**Designation** Lecturer Physics

**Address** Superior College, Lahore 54000 Pakistan

**Date** 08/08/2019 – 30/10/2020

**Website** <https://www.superiorcolleges.edu.pk/>

### **Main Duties**

- ❖ Teaching Physics subjects and attending laboratory classes of High School students.
- ❖ Organize educational/social events in college.

### **Publications**

- ❖ S. M. A Sarfraz, S. Bashir, K. Mahmood, **A. Khaliq** and R. Rizvi, "Fluence dependent sputtering yield measurement, surface morphology, crater depth and hardness of laser irradiated Zr in N and Ne environments" *Journal of Optical Society of America B*. Volume 36, Pages 1945-1957 (2019).
- ❖ Cinzia Di Franco, Eleonora Macchia, Lucia Sarcina, Nicoletta Ditaranto, **Aniqa Khaliq**, Luisa Torsi, and Gaetano Scamarcio. "Extended Work Function Shift of Large-Area Biofunctionalized Surfaces Triggered by a Few Single-Molecule Affinity Binding Events." *Advanced Materials Interfaces* 10, no. 6 (2023): 2201829.

### **Digital Skills**

Microsoft Word	Microsoft PowerPoint	Microsoft Excel
C++ (Basic)	Python (Basic)	Microsoft Visio
Origin	NT-MDT image analysis	

### **Networks and memberships**

CNR - IFN, Institute of Photonics and Nanotechnologies (Member)

18/01/2021 – CURRENT

**Address** Via Giovanni Amendola 173, 70125 Bari, Italy

**Website** <https://www.ba.ifn.cnr.it/>

### **Honours and awards**

International Fully Funded PhD Studentship – University of Bari, Italy

Date 18/01/2021 – 17/09/2024

Laptop Merit Award – Punjab Government

(August 2018)

### **Research Interests**

Atomic Force Microscopy (AFM)

Amplitude Modulation – Atomic Force Microscopy (AM-AFM)

Kelvin Probe Force Microscopy (KPFM)

Bio-interfaces

Protein Films

Mechanical Properties

Surface Properties

### **Recommendations**

**Prof. Gaetano Scamarcio** – PhD Supervisor

Director of CNR NANO, **Piazza San Silvestro 12, I – 56127 Pisa, Italy**

**Full Professor** at the Department of Physics, University of Bari, Italy

**Email** [gaetano.scamarcio@uniba.it](mailto:gaetano.scamarcio@uniba.it)

**Dr. Cinzia Di Franco** – Researcher

Head/Responsible of CNR - Institute of Photonics and Nanotechnologies, Bari, Italy

**Email** [cinzia.difranco@uniba.it](mailto:cinzia.difranco@uniba.it)